ABSTRACT

Title of Dissertation:	HYBRID PLASMONIC TUBULAR NANOSTRUCTURES: SYNTHESIS, OPTICAL AND PHOTOELECTROCATALYTIC PROPERTY
	Qian Zhang, Doctor of Philosophy, 2022
Dissertation directed by:	Professor Zhihong Nie, Professor Sang Bok Lee, Department of Chemistry and Biochemistry

Utilizing sustainable and clean solar energy in the visible-NIR range to drive chemical transformation has been a key resolution to solve the energy crisis. Recently, rational design of photocatalysts that conjugate plasmonic nanostructures with catalytic metal nanostructures has attracted particular research interests. This dissertation describes the design principles of plasmonic-catalytic hybrid tubular nanostructures and investigates their application in photoelectrocatalytic reactions.

First, we introduced the mechanism of plasmon-mediated catalysis and current research of plasmonic photocatalysts. Specifically, managing the energy flow from the plasmonic entity to the catalytic entity is the crucial part for customizable design of photoelectrocatalysts. We also summarized the design principles of general electrocatalysts and synthesis of hollow nanostructures.

Second, we reported a facile but highly reproducible synthetic strategy to fabricate catalytic Pt hollow nanotubes (NTs). Scalable fabrication of ultrathin Pt NTs can be achieved through simple mediation of the concentration of the surfactant employed in the reaction.

Third, we reported a template-directed synthesis of PtAu NTs with tunable localized surface plasmon resonance (LSPR) bands in the visible-near infrared region (NIR). The geometric dependent LSPR band shift was systematically studied based off the spectra from both experiment and finite-difference time-domain (FDTD) simulations. It was found that the PtAu NTs exhibited the LSPR characters of both rodlike and hollow nanostructures.

Finally, we investigated the photoelectrocatalytic performance of the PtAu NTs under visible-NIR light irradiation. The optimized photocatalytic activity of the PtAu NTs towards the electrooxidation of methanol was achieved by maximizing their LSPR absorption cross sections at longer wavelengths in the visible-NIR region. Meanwhile, combining the superior intrinsic electrocatalytic performance of PtAu NTs towards methanol oxidation, we expected the bimetallic PtAu tubular nanostructure could effectively convert visible light energy to drive the electrochemical transformation.

HYBRID PLASMONIC TUBULAR NANOSTRUCTURES: SYNTHESIS, OPTICAL AND PHOTOELECTROCATALYTIC PROPERTY

by

Qian Zhang

Dissertation submitted to the Faculty of the Graduate School of the
University of Maryland, College Park, in partial fulfillment
of the requirements for the degree of
Doctor of Philosophy
2022

Advisory Committee:
Professor Sang Bok Lee, Chair
Professor Zhihong Nie
Professor YuHuang Wang
Professor Leah Dodson
Professor Dongxia Liu, Dean's Representative

© Copyright by
Qian Zhang
2022

Dedication

To my beloved parents, Chenglian Zhang and Liqin Zheng.

Acknowledgements

I would like to thank both my advisors, Dr. Zhihong Nie and Dr. Sang Bok Lee, who served as great examples to guide me during my graduate research. Dr. Nie led me to "think of the bigger picture" in this field. I have learned not only related knowledge but also rational experimental design and straightforward presentation skills from him. As my co-advisor, Dr. Lee encouraged me to explore my research area of interest and to learn deeper. Also, he generously supported me on the electrochemistry part of my research. It is impossible for me to write this dissertation without the full support from both of my advisors.

During my study at the University of Maryland, I learned a lot from my colleagues and my friends. I would like to thank all members in Dr. Nie's lab for their encouragement and kind help. I would like to thank Dr. Zhiqi Huang, Dr, Chenglin Yi, Dr. Xiaoying Lin, Kyle Webb and Chelsey Lamar for their help on my experimental part. I would like to thank Dr. Hongyu Guo for the help on writing.

I'm very grateful for the help from Dr. Lee's group member, Dr. Nam Kim, for assisting me on the photoelectrochemical test platform design. Meanwhile, I would also like to thank Dr. Zhiling Zhao from Dr. Payne's group, Dr. Yi Peng at Wayne State University and Tianyu Li from Dr. Rodriguez's group for their help on the electrochemical data discussion.

I would also like to thank Dr. Shangjie Yu at Stanford University for the FDTD simulation and results interpretation, Huanyu Liu from Dr. Min Ouyang's group, Dr.

Nikolas Liaros from Dr. Fourkas's group and Danielle Le Roux from Dr. Blough's group for the laser and Xe lamp calibration.

I would also like thank Dr. Earle Stone for the discussion on the micelle behavior and surfactant-metal ion interaction.

Last but not least, I am thankful for the support I received from my loving friends, Huaqing Li, Lin Wan, Zhuo Wang, Tianhui Zhang and Jessica Snyder when I faced difficulties.

I would like to thank my committee members, Prof. YuHuang Wang, Prof. Leah Dodson and Prof. Dongxia Liu for their valuable comments on my defense and dissertation.

Table of Contents

List of Abbreviations

1D: one dimensional

AAO: anodic aluminum oxide

AIBN: 2,2-azobis(2-methylpropionitrile)

AR: aspect ratio

BAC-Cn: benzyldimethyl ammonium surfactant

CMC: critical micelle concentration

c_{surf}^{+}: the concentration of the surfactant

CnTAB: trimethyl ammonium surfactant

CV: cyclic voltammetry

DLS: dynamic light scattering

DMFC: direct methanol fuel cell

e^{-}-h^{+} pairs: electron-hole pairs

ECSA: electrochemical surface area

EDX: energy dispersive X-ray analysis

E_F: Fermi level

EG: ethylene glycol

EM: electromagnetic field

EtOH: ethanol

FDTD: finite-difference time-domain

FFT: Fast Fourier Transform

FWHM: full width at half maximum

GCE: glassy carbon electrode

HAADF-STEM: high-angle annular dark-field scanning TEM

HER: hydrogen evolution reaction

HOMO: highest occupied molecular orbital

HRTEM: high-resolution TEM

ICP: inductively coupled plasma

ICP-AES: inductively coupled plasma atomic emission spectroscopy

I.D.: inner diameter

IECSA: integrated extinction cross section area

I_f/I_b: ratio between the peak current in the forward and backward scan

k_{PEEF}: the slope of PEEF over the light intensity

L: length

L-Au NRs: long Au nanorods

L-AuPd NRs: long AuPd coaxial nanorod templates

L-Ext: the longitudinal extinction mode

LSPR: localized surface plasmon resonance

LT-AR: length/total wall thickness of PtAu NTs

LT-Pt: long Pt nanotube

LT-PtAu: long PtAu nanotube

LUMO: lowest unoccupied molecular orbital

LW-AR: length/width aspect ratio

M-Au NRs: medium Au nanorods

M-AuPd NRs: medium AuPd coaxial nanorod templates

MOF: metal-organic framework

MOR: methanol oxidation reaction

MT-Pt: medium Pt nanotube

MT-PtAu: medium PtAu nanotube

NIR: near infrared region

NCs: nanocages

NPs: nanoparticles

NRs: nanorods

NSs: nanoshells

NTs: nanotubes

NW: nanowires

OCP: open-circuit potential

OER: oxygen evolution reaction

ORR: oxygen reduction reaction

PC: polycarbonate

PEC: photoelectrochemistry

PEEF: photoelectrochemical enhancement factor

PS: polystyrene

QACs: quaternary ammonium compounds

SAED: selective area electron diffraction

S-Au ARs: short Au nanorods

S-AuPd NRs: short AuPd coaxial nanorod templates

SPR: surface plasmon resonance

ST-Pt: short Pt nanotube

ST-PtAu: short PtAu nanotube

Surf-M: metal ion-cationic surfactant complex

T: thickness

TEM: transmission electron microscopy

T-Ext: the transverse extinction mode

TMPTA: trimethylolpropane triacrylate

UPD: underpotential deposition

UV: ultraviolet

W: width

WE: working electrode

WT-AR: width/total wall thickness of PtAu NTs

XPS: X-ray photoelectron spectra

Chapter 1: Introduction

Part of this chapter is adapted from the manuscript in preparation: Zhang, Q., Kim, N., Zhao, Z. L., Peng, Y., Lee, S. B., Nie, Z. H., Plasmonic Photoelectrocatalysis

Energy, in the forms of thermal, electrical, and chemical etc., is the fundamental essence for the sustainable development of human society. Solar energy is regarded as the most clean and renewable energy source. A total of 173,000 TWh of solar energy strikes the Earth. Therefore, efficiently converting the solar energy to chemical energy has long been the core scientific topic.

Photocatalysis harvests photon from light irradiation to drive exothermic/endothermic chemical reactions to release/store the energy. Fujishima and Honda employed TiO_2 semiconductor electrode to actuate electrochemical H_2O splitting under ultraviolet (UV) light irradiation in their pioneer work[1]. Following, semiconductor photocatalysts (e.g., TiO_2, ZnO, WO_3, CdS, GaP *etc.*) have been extensively studied for their photocatalytic applications, such as H_2O splitting, CO_2 reduction, organic pollutants decomposition *etc*. Yet, the commonly used semiconductor photocatalysts with band gaps around 2.25-3.5 eV can only absorb UV light and short-wavelength visible light[2]. Majority of the solar energy concentrates in the range of visible to near infrared region (NIR). Consequently, numerous photocatalysts have been designed to absorb broadband visible-NIR light to drive chemical transformation.

Plasmonic nanomaterials interact strongly with incident light radiation owing to the localized surface plasmon resonance (LSPR). This unique optical property, as a function of composition, size and shape of the metallic nanostructure, empowers plasmonic nanomaterials with tunable light absorption in visible-NIR region. Thus,

developing photocatalysts by incorporating plasmonic nanostructure, such as pure plasmonic metal, plasmonic-semiconductor and plasmonic-catalytic hybrid nanostructures, and investigating the underlying mechanism have attracted intensive research interest recently.

1.1 Introduction of LSPR

1.1.1 Mechanism of LSPR

When the metal surface is irradiated by incident light, the free conductive electrons are delocalized by interacting with the sinusoidal oscillating electric field (Figure 1.1a). If the frequency of the incident light matches with the natural frequency of the metal plasmon oscillation, the system will absorb maximum energy from the incident light and reach resonance, which is known as surface plasmon resonance (SPR)[3]. For nanostructures whose sizes are smaller than the wavelength of the incident light, the collective electron oscillation is confined to the nanostructures on its surface, which is termed as LSPR. Al, Mg and Ga exhibit strong LSPR in the UV region. For Au, Ag and Cu, the maximum LSPR extinction bands are in the visible region. By further tuning the size, shape and interparticle distance of the nanostructures, the extinction band can be further extended into the NIR region.

1.1.2 Geometry-dependent LSPR characteristics of nanostructures

1.1.2.1 Spherical nanoparticles (NPs)

For spherical NPs (d/λ <0.1, d is the diameter of the NP, λ is the wavelength of the incident light), the Maxwell's equation is solved using a quasi-static approximation where the electromagnetic phase is assumed as constant (Figure 1.1b). Based off Mie's

theory, the extinction cross-section of a spherical nanoparticle (NP) can be expressed as[4]:

$$E\ (\lambda) = \frac{24\pi^2 N a^3 \varepsilon_m^{3/2}}{\lambda \ln(10)} \cdot \frac{\varepsilon_2(\lambda)}{(\varepsilon_1(\lambda) + 2\varepsilon_m)^2 + \varepsilon_2(\lambda)^2} \quad (1)$$

where a is the radius of the particle, ε_1 and ε_2 are the real and imaginary parts of the metal dielectric function, respectively, ε_m is the dielectric constant of the surrounding medium. According to eqn (1), the LSPR wavelength and intensity (extinction coefficient) are a function of composition, size and shape of the metallic nanostructure. When ε_1=- 2ε_m, the resonance reaches maximum. The extinction energy is proportional to the radius of the NP. Thus, with the increasing of the NP radius, the extinction band would red-shift to longer wavelength. Experimental results showed that a single LSPR band corresponding to the dipolar resonance shifted from 518.5 nm to 556 nm as the size of Au NPs increased from 8.4 to 96.1 nm (Figure 1.1d and 1.1e). Further increasing the size of the Au NPs would not only cause LSPR band red-shift but also significant peak broadening. When the size of Au NPs was above 120 nm, an additional shoulder peak at lower wavelength, which corresponds to a quadrupolar resonance, appeared[5].

1.1.2.2 Nanorods (NRs)

Nanorod (NR) is a typical anisotropic system. Take Au NRs for example, the plasmon resonance of Au NRs is split between the transverse and longitudinal dipole resonances due to the anisotropic morphology. The longitudinal mode correponds to the electron cloud osillation along the length of the NR and the the transverse mode correponds to the osillation along the width of the NR(Figure 1.1c)[3,6]. The longitudinal plasmon resonance appears at longer wavelength while the transverse plasmon resonance

appears at shorter wavelength. The spliting and position of the two extinction bands depend on the aspect ratio (AR, defined as length/width) of Au NRs. According to Mie-Gans theory, for a fixed dielectric environment, as the AR increases, the maximum longitudinal absorption resonance increases[7]. Extensive experimental results were found in good agreement with the theorical calculation. For instance, Murray *et al.* adjusted the AR of Au NRs from 3.8 to 7.6 continuously, which red-shifted the longitudinal LSPR band from 790 nm to 1150 nm (Figure 1.1f and 1.1g)[8].

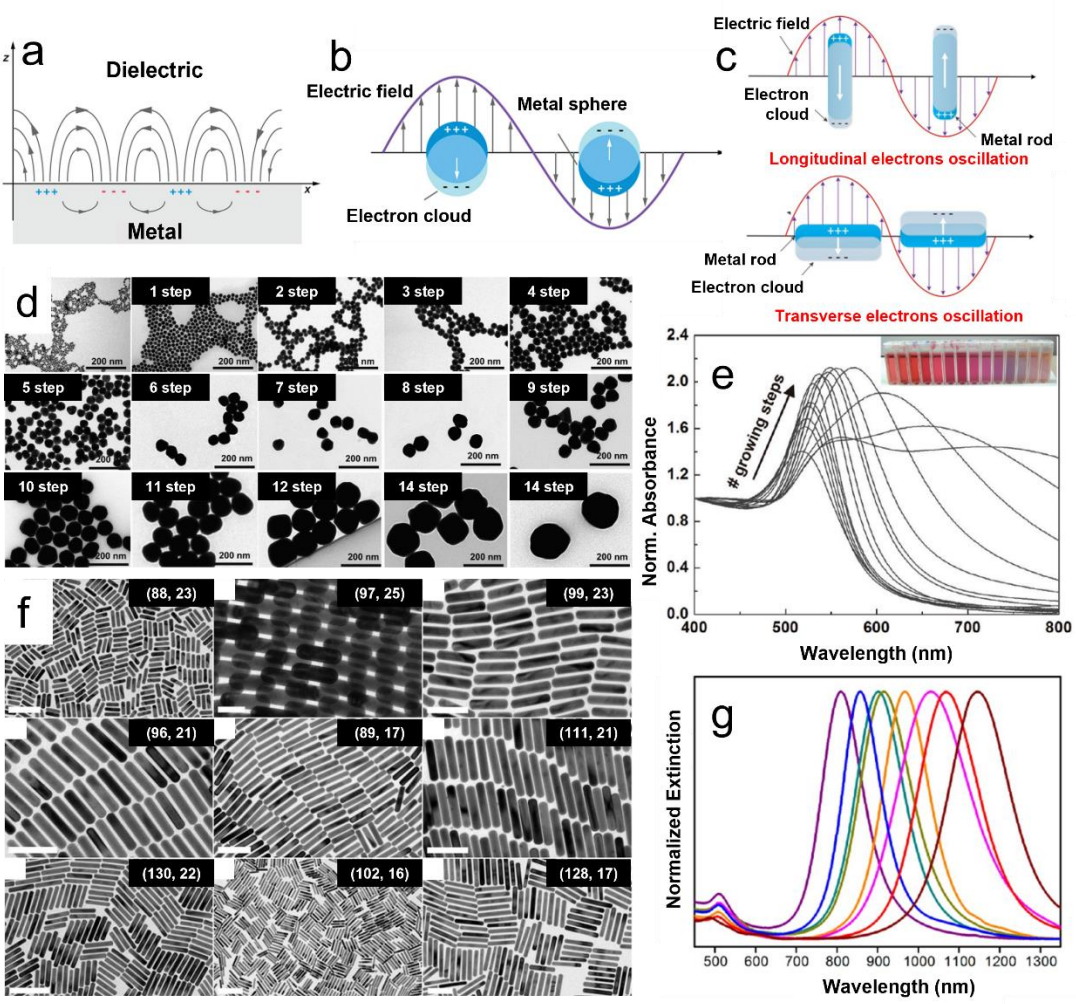

Figure 1.1 Schematic figure of (a) surface plasmon polariton, (b) LSPR excitation of metal NPs, (c) LSPR excitation of Au NRs along the longitudinal and transverse

direction, respectively[6]. (d) Transmission electron microscopy (TEM) images of Au NPs with sizes increase from 8.4 ±1.0 to 180.5±10.7 nm[5]. (e) UV-vis spectra of Au NPs presented in (d), the inset is the photo images of the corresponding Au NPs[5]. (f) TEM images of Au NRs with increased AR[8]. (g) Normalized extinction spectra of Au NRs in (f), the longitudinal LSPR peak shifts to longer wavelength with increasing the AR[8].

1.1.2.3 Hollow nanostructures

Typical hollow nanostructures include spherical nanoshells (NSs), nanocages (NCs), and nanotubes (NTs) *etc*. Halas and co-workers were the first to fabricate Au NSs with dielectric silica core[9]. The LSPR bands of the Au NSs were demonstrated to be tuned into the NIR region by varying ratio between the shell thickness and the core diameter (the ratio between outer diameter and shell thickness was defined as the AR for hollow nanostructure, Figure 1.2a-d)[10]. Xia *et al.* synthesized Au-Ag NCs by employing Ag nanocubes as templates. The LSPR band of the NC would red-shift when the ratio between the shell thickness and the outer diameter decrease(Figure 1.2e-g)[11,12]. To understand the AR dependent LSPR of hollow nanostructure, Prodan *et al.* developed *plasmon hybridization* model, in which the plasmon resonance of Au NSs was considered as an interaction between a solid nanosphere and a nanocavity[13]. The interaction splits the plasmon resonances into a “bonding” plasmon with symmetric coupled lower energy and an “antibonding” plasmon with antisymmetric coupled higher energy (Figure 1.2h). A decreased AR (by decreasing the shell thickness) would cause an increased interaction between the nanosphere and nanocavity, which increases

the splitting between “bonding” and “antibonding” mode and shifts the Au NSs LSPR band to lower energy[14,15].

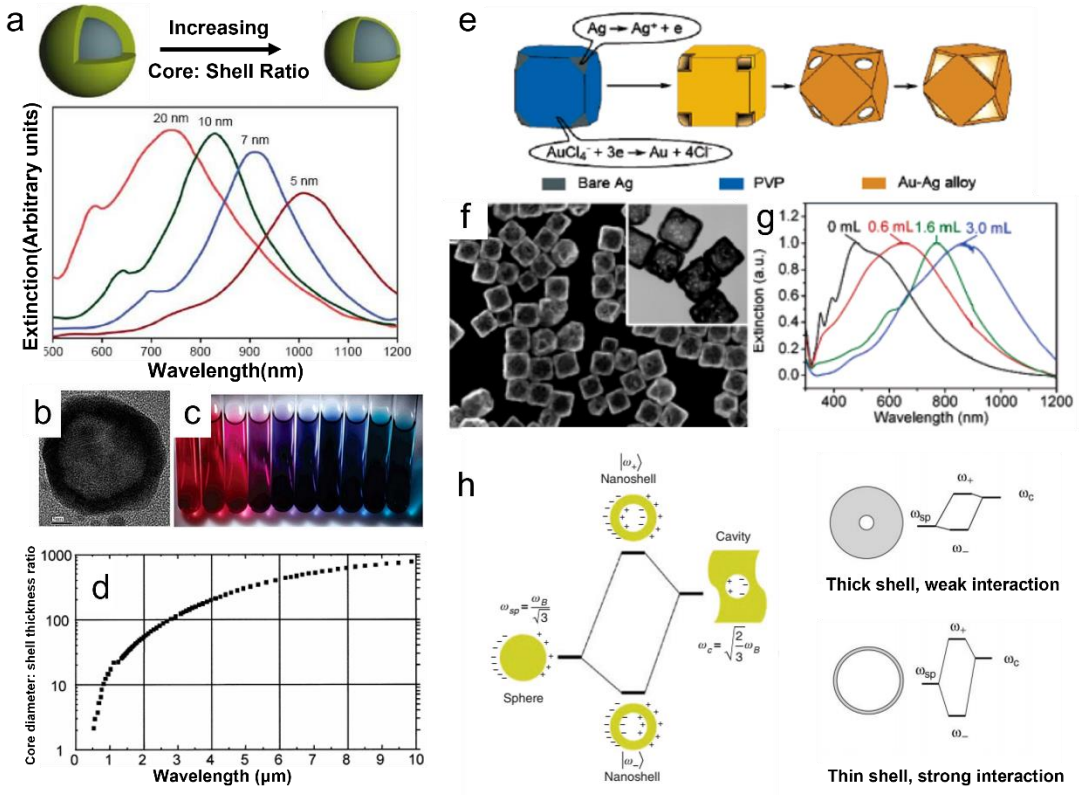

Figure 1.2 (a) The LSPR resonance of Au NSs, the extinction peak red-shifts with increasing the ratio between core diameter and shell thickness ratio[16]. (b) TEM image of a single Au NS[10]. (c) Photo image showing the color change of Au NS with increased AR[10]. (d) Calculated optical resonance wavelength as a function of core diameter/shell thickness ratio for Au NSs with silica core[9]. (e) Schematic figure of the synthesis steps of Au-Ag NCs[11]. (f) SEM image of the hollow Au-Ag NCs, inset is the TEM image of corresponding Au-Ag NCs[11]. (g) UV-vis-NIR spectra of Au-Ag NCs formation process from Ag nanocubes titrated with different volumes of 0.1 mM $HAuCl_4$[11]. (h) Plasmon hybridization and the nanosphere-nanocativity interaction model for NCs[13,15].

1.2 Mechanism of plasmon-mediated catalysis

As discussed above, the extinction cross-section of plasmonic metal nanostructure can be adjusted to the visible-NIR region by simply tuning their shapes, sizes and composition. Thus, plasmonic nanostructure based photocatalysts hold great promise to sunlight-driven photochemical reaction by efficiently utilizing solar energy in the visible-NIR region.

1.2.1 Light-matter interaction

The commonly accepted mechanisms for the plamonic enhanced photocatalysis are: (1) hot carrier (hot electron-hole (e^--h^+) pairs); (2) electromagnetic-field enhancement, and (3) photothermal effect (Figure 1.3a).

Upon light irradiaiton on clean plasmonic metal surface, the free conductive electrons coherently oscillate with the electromagnetic field and create LSPR (Step 1 in Figure 1.3b). From a quantum view, the polarized LSPR has been described as a coherent superposition of low-energy electrons and holes near the Fermi level (E_F)[17]. The plasmon decay (or called as 'relax') within a few femtoseconds (fs) through either radiative photon re-emission (scattering) or non-radiative excitation of energetic charge carriers (absorption) on the surface of the NPs, which is known as Laudau damping process, as presented in Step 2 in Figure 1.3b. The energy of the e^--h^+ pairs generated in the non-radiative decay within 1-100 fs equals to the photon energy. The hot e^- and h^+ are initially in a nonthermal distribution and rapidly thermalizes to a Fermi-Dirac distribution *via* electron-electron (Step 3 in Figure 1.3b) and electron-phonon scattering (100 fs-10 ps) that result in a higher lattice temperature. The heat then slowly dissipates to the environment (100 ps-10 ns, Step 4 in Figure 1.3b)[18].

The radiative photon re-emission (scattering) dominates plasmon decay mode for larger plasmonic nanostructures (d > 70 nm), while the non-radiative decay (absorption) with the hot e^--h^+ pair formation is the dominant mode for smaller plasmonic nanostructures[17,19]. Meanwhile, there is no HOMO-LUMO energy separation or analogous valence-conduction band and energy separation in plasmonic excitation.

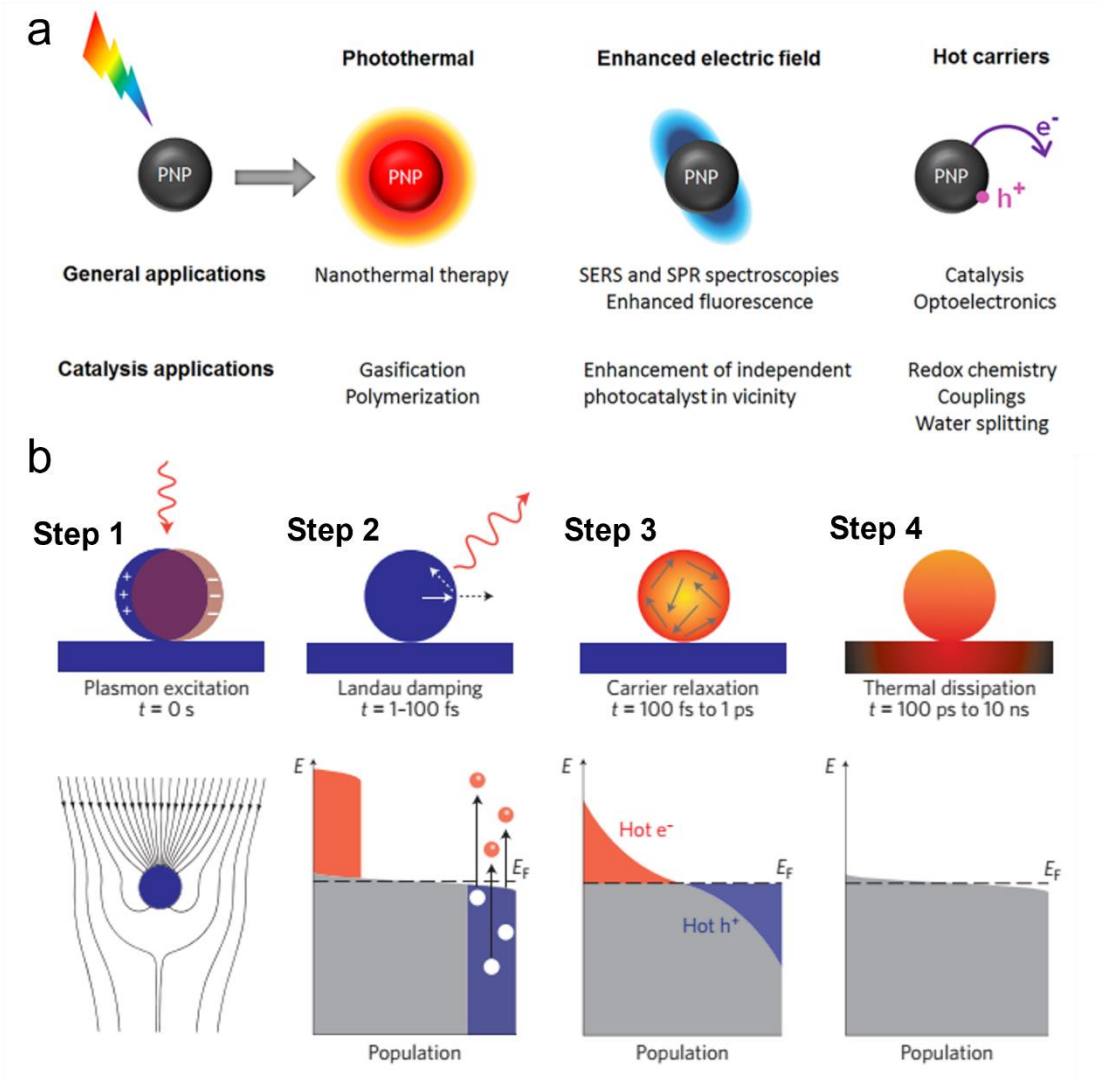

Figure 1.3 (a) Schematic of the three commonly accepted mechanisms for the plamonic enhanced photocatalysis arising from LSPR. Their relevance to catalysis may vary as a function of the plasmonic NP design[20]. (b) Photoexcitation and subsequent relaxation

process upon light illumination of a metal NP with a laser pulse and characteristic timescale[21]. Step 1: the exciation of a LSP redirects the flow of light towards and into the NP. Step 2: Landau damping in the first 1-100 fs and the athermal distribution of hot carrier. Step 3: hot carrier redistribution *via* electron-electron scatttering processes ranging from 100 fs to 1 ps. Step 4: Heat transfer to the surroundings on a timescale ranging from 100 ps to 10 ns *via* thermal conduction.

1.2.2 Photothermal effect (heat) induced chemical transformation

The photothermal process occurred when the hot carriers decay and convert the energy into heat through inelastic Coulombic electron-electron and electron-phonon scattering. The electrons couple with phonon modes *via* electron-lattice collisions and increase the temperature of the metal lattice. Later the heat transfers from the metal lattice to the soundings through phonon-phonon scattering (100 ps-10 ns). Thus, the plasmonic nanostrutures serves as 'nano heaters' to accelerate the reaction by increasing the local temperature in the reaction environment.

The local temperature increase caused by photothermal effect can be expressed as[22–24]:

$$\Delta T(r) = \frac{V_{NP} Q}{4\pi k_0 r} \tag{2}$$

where r is the distance from the center of the NP, V_{NP} is the volume of the NP, k_0 is the thermal conductivity of the sounding medium, and Q is the heat.

For a single spherical NP, the heat Q generated from photothermal effect is:

$$Q = \frac{\omega}{8\pi} E_0^2 \left| \frac{3\varepsilon_0}{2\varepsilon_0 + \varepsilon_{NP}} \right|^2 Im\varepsilon_{NP} \tag{3}$$

Derived from eqn (2) and eqn (3), the dependence of maximum temperature increase (ΔT_{max}) on the radius of the NP (R_{NP}) expresses as:

$$\Delta T_{max} \propto R_{NP}^2 \quad (4)$$

According to eqn (4), the thermal contribution increases as the increase of the size of the NP. Furthermore, Govorov *et al.* theorized that the photothermal effect can be strongly enhanced in the presence of massive NPs owing to the collective effect[23,25]. Several research groups have reported employing photothermal effect to enhance chemical transformation. Netto-Ferreira and Scaiano *et al.* demonstrated this effect by irradiating Au NPs with 532 nm pulsed laser to a high temperature (~500°C) and induced catalysis of the endothermic decomposition of dicumyl peroxide within less than 1 min, which originally required either hours of maintaining the reaction above 140 °C or UV irradiation[26]. Lear *et al.* reported prominent bulk-scale polyurethane film curing induced by the photothermal effect. Upon irradiation of 8 ns pulses of 532nm laser (50 mJ per pulse, peak irrdiance 12.5MW cm^{-2}), the rate of the bond formation between isocyanates and alcohols was unprecedentedly enhanced billion-fold[27]. Boyd *et al.* demonstrated that the plamsonic heating could lead heterogeneous catalysis of steam reforming of ethanol[28]. Upon a low-power laser irradiation, the mixture of ethanol-water passed through a flow-type microfluidic channel reactor embeded with 20 nm Au NPs and was converted to a mixture containg CO_2, CO and H_2. The fast response of photothermal effect upon external irradiation allowed the catalysis reaction to carry out in a controllable and miniaturized manner. To increase the reaction selectivity, plasmonic nanostructure often couple with other components to reach a synergistic effect. Jiang and co-workers reported the first case of plasmonic metal based

synergestic catalysts by encapsulating Pd nanocubes into metal-organic framework (MOF) ZIF-8[29]. While Pd nanocubes served as the plasmonic heating center, the ZIF-8 acted as a molecular sieve for olefins with different sizes. The composite presented efficient and seletive catalytic hydrogenation of olefins with a yield of 66% at room temperature under 1atm H_2 and 100 mW cm^{-2} Xe lamp irradiation. Meanwhile, the MOF can further stablize the Pd nanocube to increase the stability and recyclability of the catalysts. Similarly, complex nanocatalysts based off plasmonic photothermal effect, e.g., Cu_7S_4@ZIF-8[30], Pt/PCN-224 (Zn)[31], are reported exhibiting excellent catalytic performance with elevated yield, enhanced seletivity and mild reaction condition.

1.2.3 Enhanced electromagnetic field (EM) assisted chemical transformation

The oscillating electromagnetic field (EM) caused by LSPR close to the NP surface generates a much higher local field enhancement ($|E|$) compared to the incident field ($|E_0|$, the amplitude of the incident electric field). The areas of enhanced EM field are often referred to as "hot spots". The intensity and location of the hot spots depend on size, shape, composition and aggregation states of the NPs, such as sharp tips and small gaps between NPs[32]. Recently, the hot spots are found to contribute to the photocatalysis as the near-field enhanced electromagnetic field by directly activating nearby species or boost the exciton generation on the adjacent semiconductors[33]. Scaiano *et al.* demonstrated that the enhancement of the EM in vicinity of Ag NPs can initiate *in situ* polymerization on Ag NPs surface[34]. Upon irradiation (405 nm LED light source with a light flux of ~ 207W m^{-2}), the cross-link of trimethylolpropane triacrylate (TMPTA) formed a ~8 nm coating layer on Ag NPs surface in the presence

of 2,2-azobis(2-methylpropionitrile) (AIBN). The author spectulated that the EM excitation of AIBN initiated the polymerization thus only selectively cross-linking on Ag NPs surface was observed. Cronin *et al.* demonstrated that the Au coated TiO_2 nanocomplex showed enhancements of 5× and 66 × in photoelectrochemical water splitting upon 532 nm and 633 nm laser irradiation, respectively[35]. Based on the finite-difference time-domain (FDTD) result, the improved photocatalytic activity was ascribed to the local electric field enhancement near the TiO_2 surface, which increased the amount of the photogenerated charge, rather than by the direct charge transfer between Au and TiO_2. Ke *et al.* reported enhanced acetalization of aromatic aldehyde with methanol by the Au NPs decorated in NaY zeolite[36]. The author proposed that the LSPR induced EM intensified the polarized electrostatic field of Na^+, which facilitated the C=O bond breakage in the reactants and resulted in accelerating the reaction rate.

1.2.4 Hot carriers induced chemical transformation through charge transfer

The e^--h^+ pair formation has been demonstrated as a main energy loss mechanism of LSPR in metal[21,37,38]. The hot electrons have been widely employed to drive various reduction reactions. Meanwhile, the hot hole-driven photochemical oxidation reaction encounters challenges due to the short lifetime, large effective mass, and low kinetic energy of the hot holes compared with those of hot electrons[38,39].

The energetic e^--h^+ pairs formation can proceed *via* indirect electronic excitation (*s*-to-*s* intraband transition) or direct electronic excitation (*d*-to-*s* interband transition). For the intraband transition, the electrons are excited from filled *s* states below the E_F to empty *s* states above the E_F with the assistance of lattice phonons to change the

momentum. Interband transition involves the electron excitation from filled *d* states below the E_F to empty *s* states above the E_F (Figure 1.4a)[17]. The interband/ intraband excitation by certain wavlength is based off the relative position of *d* band to the E_F. Ag with a full *d* band position much lower than the E_F cannot excite the *d*-to-*s* interband transition by visible light (Figure 1.4b). For Au and Cu, whose full *d* band positions are higher than that of Ag but below the E_F, the *d*-to-*s* interband transition can be excited by visible light photons above a specific threshold energy. For transition metals such as Pt and Pd, with partially filled *d* bands intersect with the E_F, the metals can absorb photons to excite interband transition throughout the visible range(Figure 1.4c)[40].

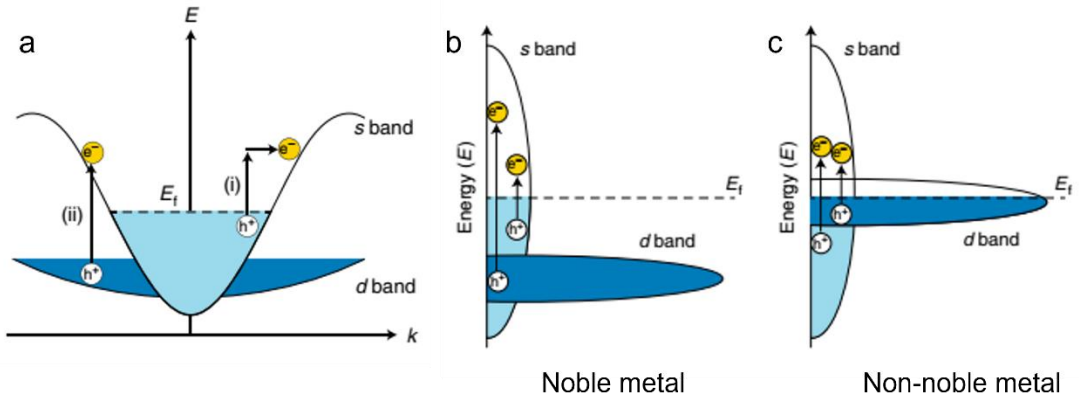

Figure 1.4 (a) band diagram depiction of intraband excitation and interband excitation. (b-c)The representative density of states of plasmonic noble metal and non-noble transition metal[40].

The extraction/separation of the plasmon-generated hot carriers before thermalization is crucial in efficiently driving the photocatalytic reaction[18,21]. Conjugating semiconductor with plasmonic metal is one of the most common strategies[19,41–43]. The interfacial Schottky barrier prevents the recombination of the energetic e^--h^+ pairs by spatially separating the hot electrons from hot holes, thus prolong the lifetime of the

hot carriers to match the kinetics of the target chemical reactions[44]. The photcatalytic performance of plasmonic metal-semiconductor conjugate systems has been investigated in various important chemical transformations, such as water splitting[45–48], CO_2 reduction[49,50] and organic transformation[51], *etc*.

Recently, multimetallic systems that incorporate plamonic metal and catalytic metal are of great research interest. Rational design of multimetallic materials to guide the photon absorption, engineer the plasmon decay pathway and maximize photocatalystic performance has been the key concern. Linic *et al.* investigated the energy flow in multimetallic plasmonic nanoparticles by modeling Ag-Pt and Au-Pt core-shell NPs of different sizes and shapes[52]. It is found that smaller NPs that support higher electric field intensities could direct more energy from the noble metal core to the Pt coating layer. More importantly, the energy transfer from a plamonic component (Au, Ag *et al.*) to the catalystic transition metal (Pt, Pd *et al.*) are dependent on the ratio of the imaginary part of the materials' dielectric function (ε_2). The wavelength dependent ε_2 of different metals are presented in Figure 1.5a. For the Ag-Pt system, the incident energy transfers from the Ag core to the Pt shell at all LSPR wavelengths (Figure 1.5c), indicating the photons are absorbed more significantly by Pt than Ag (Figure 1.5e1 and e2). Therefore, the selective formation of energetic e^--h^+ pairs moves to the Pt shell. Experimentally, the Ag-Pt core-shell nanocubes show excellent catalytic performance towards CO oxidation with accelerated reaction rate and selectivity upon broadband visible light irradiation at a 400 mW cm^{-2} intensity (Figure 1.5b1-3)[53]. On the other hand, for the Au-Pt system, the energy is preferentially directed from Au to Pt when the LSPR extinction band shifts to longer wavelengths (> 600 nm), where the ratio of

ε_2 between Pt and Au is high (Figure 1.5d). Meanwhile, less energy is tranferred from Au to Pt when the LSPR band is located at a shorter wavelength (<550 nm). Thus, Au-Pt NRs coated with ultrathin Pt shells (1nm), with their longitudinal LSPR bands located at longer wavelengths, were expected to direct more energy to the Pt shell when exciting the longitudinal LSPR band upon light irradiation (Figure 1.5f1 and f2). Furthermore, Cortés and Han also found that the hot spots among the gaps of the assembly of the Au@M (M=Pt, Pd) core-shell structures assist energy transfer from Au core to the nonplasmonic shell[54]. The plasmonic-catalytic bimetallic Au@Pd assembly structure displayed distinguishable catalytic performance towards 4-nitrobenzenethiol compared to the pure Au NPs assembly structure.

Other bimetallic systems, such as alloys, antenna-reactor complexes, core-shell NPs, heterodimers, have also been demonstrated to efficiently drive photocatalytic reactions[49,55–60].

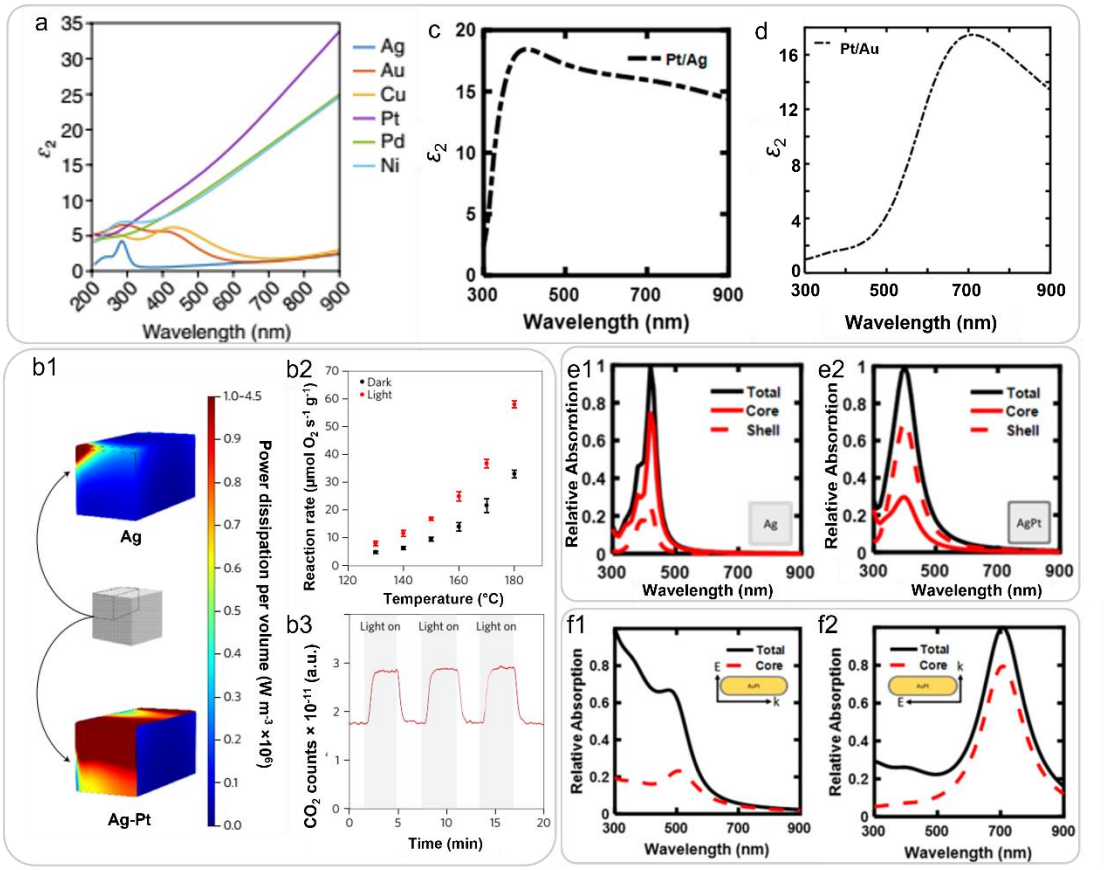

Figure 1.5 (a) The imaginary part of dielectric function of plasmonic metals and other transition metals[40]. (b1) Heat maps of the power dissipation per volume at the LSPR peak (455 nm) for the Ag nanocube and at the LSPR peak (460 nm) for the Ag-Pt nanocube; (b2) Reaction rate versus temperature for preferential CO oxidation in excess H_2 on Ag-Pt core-shell nanocubes under light-off and light-on conditions and (b3) Fast-response mass spectrometry analysis of CO_2 produced during the cycling of light-on and light-off conditions[53]. (c) Wavelength-dependent ratio of ε_2 of Pt with Ag. (d) Wavelength-dependent ratio of ε_2 of Pt with Au[52]. (e1-e2) Relative absorption fractions in the core vs the shell for a 40 nm Ag cube with (e1) a 1.4 nm thick Ag shell and (e2) a 1.4 nm thick Pt shell. (f1-f2) Relative absorption fractions of Au-Pt nanorod

with a length of 80 nm, width of 20 nm coated with a 1 nm Pt shell along (f1) transverse and (f2) longitudinal direction.

1.3 Plasmonic enhanced electrocatalysis

Photoelectrochemistry (PEC) utilizes external electric field to force the separation of hot electrons and holes, thus prolonging the lifetimes of the hot carriers. Similar to traditional electrochemistry (Figure 1.6a), the working electrodes (WEs) of PEC can also be classified as photoanodes and photocathodes. For PEC driven by visible-NIR light, plasmonic metals such as Au, Ag and Cu with characteristic LSPR band in visible-NIR region are often employed when designing the photocatalysts. Various photocatalysts have been demonstrated their applications in methanol oxidation reaction (MOR), oxygen reduction reaction (ORR), oxygen evolution reaction (OER), hydrogen evolution reaction (HER) *etc*. Pure LSPR metal NPs alone can serve as both light absorbers and catalytic active sites. The hot carriers excited by irradiation can modulate the nature of the electrochemical reactions occurring at the catalyst/electrolyte interface. Here we limit our discussion only to the multimetallic based photoanodes and photocathodes. The plasmonic metal-semiconductor conjugate catalysts are excluded but here are some reference review articles[18,61].

1.3.1 Photoanode

Metal photoanodes have been utilized in various photo-driven oxidation reactions. Unlike metal/semiconductor photoanode, at whose interface the Schottky barrier limits the collection efficiency of hot electron and leads to recombination of the hot electrons

and holes, metal photoanode is expected with a higher hot carrier collection efficiency. Upon light irradiation, the generated hot electrons may have three possible pathways: (1) recombine with hot holes; (2) participate in electrochemical reaction; (3) transferred into external circuit driven by an applied voltage bias while the hot holes are left on the electrode and get involved in the reaction (Figure 1.6b1).

It is demonstrated that the hot carriers accelerate the electrochemical reaction rate by generating new intermediates, electron transfer pathways *etc*. Xia *et al.* suggested the significant enhancement of photo electro-oxidation of glucose on Au NPs at a higher pH value was attributed to •OH radicals generated by the hot holes upon laser irradiation (Figure 1.6b2). The high oxidation capacity of hot holes oxidized OH^- into •OH, which could lead a faster glucose oxidation[62]. Jain and Kang *et al.* reported enhanced MOR on Pd_xAg alloy NTs driven by the hot holes and separated the hot carrier effect from the photothermal effect (Figure 1.6c1)[63]. By utilizing bulk temperature control and open-circuit potential (OCP) test (Figure 1.6c2 and c3), the authors proposed that the enhancement was attributed to an easier transition of the hot holes to the surface adsorbed methanol, which was induced by the downshift of the quasi-E_F along with the increase in light intensity.

In MOR catalytic reactions, preventing CO poisoning to prolong the catalysts' durability has been a key concern for effective catalyst design. Yang and co-workers constructed Au@AgPt trimetallic urchin-like nanostructure and studied their catalytic performance under light irradiation (Figure 1.6d1 and d2). Based on the simulation results, the adsorption of CO could be weakened by hot hole injection which was excited by LSPR. In the meantime, the introduction of Ag downshifted the *d*-band

center of Pt to further improve the MOR catalytic activity. The hot carrier energized the transfer from *CO-h site to the *CO-t sites, which weakened *CO adsorption, while the localized electric field downshifted the LUMO of CO, which facilitated the transformation of *CO to *COOH (Figure 1.6d3). Both effects contributed to the enhancement of the MOR catalytic performance[64].

1.3.2 Photocathode

Photocathodes consist of metallic nanostructures have also been reported to catalyze photo-driven reduction reactions (CO_2 reduction, ORR, HER, NO_3^- reduction reactions). However, unlike metal/*p*-type semiconductor heterostructures, on which hot holes are captured by the *p*-type semiconductor and hot electrons are trapped on metal NPs to drive reduction reactions[65], the quick hot e^--h^+ pair recombination on the metal NPs limits the catalytic efficiency even under intense light irradiation.

Similar to that of photoanode, metallic based photocathode electrocatalysts could also alter the reaction pathways. Edgeless Ag-Pt bimetallic NCs were reported to be able to suppress the formation of undesired peroxide intermediate in ORR, which could lead to a loss in overall electrocatalytic efficiency, *via* plasmonic-induced suppression (Figure 1.6e1 and e2). *In situ* Pt L_3-edge of X-ray absorption near-edge spectroscopy confirmed hot electron transfer from Ag to Pt (Figure 1.6e3). The plasmon-induced hot electron transfer may produce higher electron population in the antibonding orbital of O_2, thus weaken the O-O bond and produce the desired H_2O product (Figure 1.6e4)[66]. Smart design of the plasmonic electrocatalysts plays a vital role to direct the electron transfer. Zheng and coworkers designed Au-Pd-Pt NR by incorporating Pd between Au NRs and the surface Pt catalysts (Figure 1.6f1-f3)[67]. The optimized structure not only

maintained the strong SPR absorption from Au but also exhibited enhanced ORR catalytic activity from the formation of Pd-Pt bond. Upon visible-light irradiation, the trimetallic NRs performed specific activity 27.5 times higher than those of commercial Pt/C catalyst (Figure 1.6f4). Plasmonic metallic photocathode materials were also reported to enhance reaction selectivity. Kostecki *et al.* reported that the hot electrons excited by LSPR, whose energy was tuned by the applied potential, could be injected into molecular orbitals of nearby acceptors and result in selective reduction of target molecules (Figure 1.6g). The CO_2 reduction could be achieved when -1.1V_{RHE} and 360 nm laser irradiation were applied while for NO_3^- reduction, -1.0, -1.2 V_{RHE} and a longer wavelength were required[68].

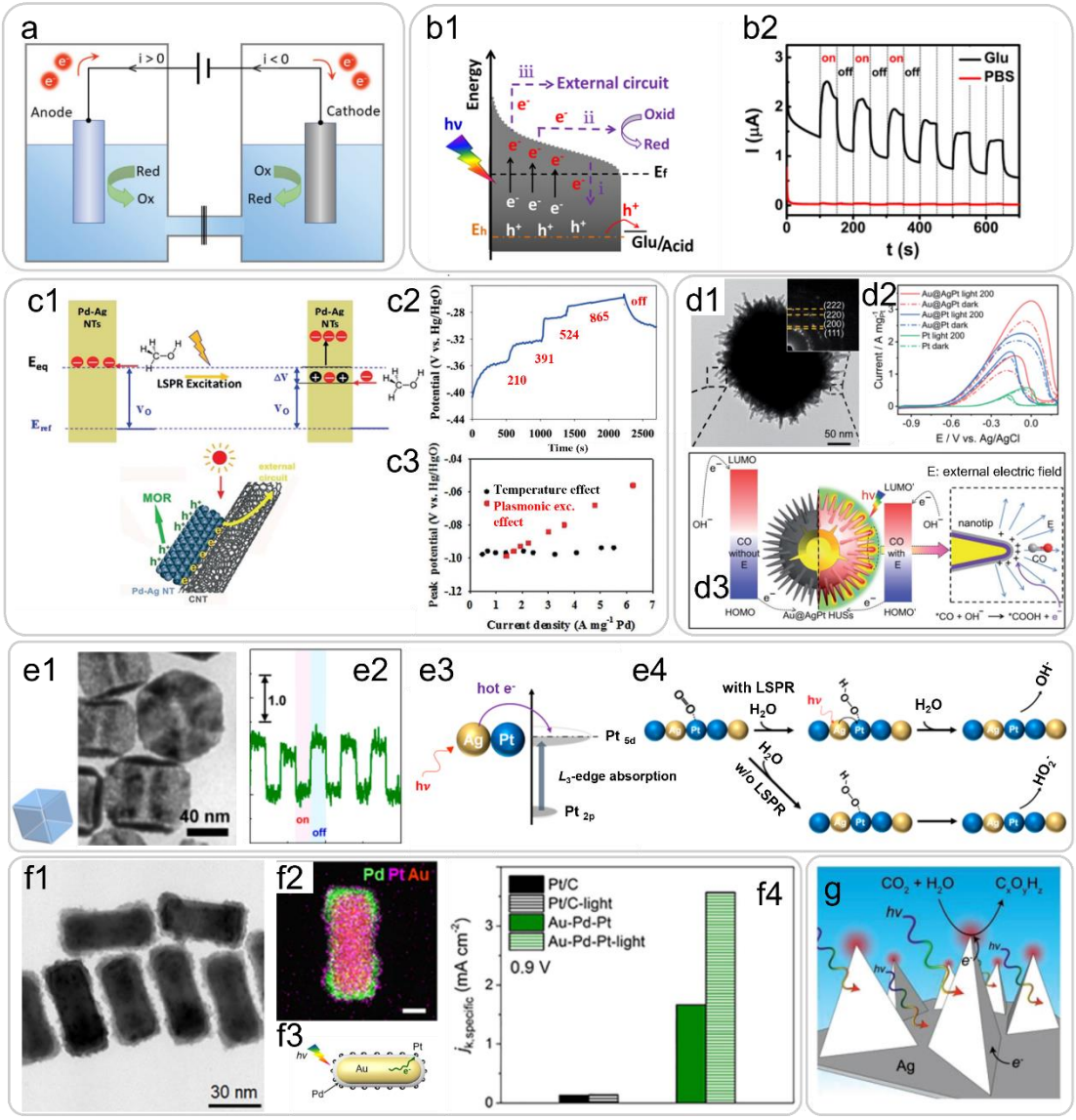

Figure 1.6 (a) A schematic of an anode and a cathode[65]. (b1) Possible transfer channels of LSPR-excited hot charge carriers with the yellow line indicating the energy level (E_h) of the hot h^+; (b2) *I-t* curves at 0.4V (*vs* Ag/AgCl) with LSPR excitation on and off in the presence and absence of 100 mM glucose[62]. (c1) Energy diagram of Pd_xAg/CNTs electrocatalysts in the dark (left) and under LSPR excitation (right); (c2) The OCP of $Pd_{0.52}Ag$/CNTs electrocatalyst in basic methanol solution as a function of time under 530 nm laser irradiation of various intensities; (c3) Peak potential derived

from the CV scans of $Pd_{0.52}Ag$/CNTs electrocatalyst at temperature control and under 530 nm laser illumination, respectively[63]. (d1) TEM image of Au@AgPt urchin-like nanostructure; (d2) MOR performance of Au@AgPt urchin-like nanostructure, Au@Pt urchin-like nanostrutures and commercial Pt/C; (d3) Mechanism diagram of the reaction when the LUMO energy level of CO molecule was downshifted by LSPR effect[64]. (e1) TEM image of edgeless Ag-Pt nanocages and the corresponding geometrical model; (e2) Fraction of peroxide change for AgPt-30 sample under chopped 532 laser irradiation; (e3) Schematic diagram of Pt L_3-edge XANES and hot electron transfer; (e4) Schematic diagram of mechanism in suppressing peroxide yield through hot electron transfer[66]. (f1) TEM image of Au-Pd-Pt NRs; (f2) element mapping of Au-Pd-Pt NRs; (f3) Schematic diagram of electron transfer from excited Au NR to Pt; (f4) Specific activities at 0.9V (*vs* RHE) of Au-Pd-Pt and Pt/C in dark and under light irradiation[67]. (g) Injection of hot carriers from plasmonic Ag to adsrobed surface species[68].

1.4 Design principle of electrocatalysts

The development of the theory and the advances in the methodology of nanomaterials synthesis *via* wet chemistry allow researchers to fabricate NPs with desired sizes, shapes and components of high uniformity to explore their improved catalytic activity at the nanoscale. Over the past decades, tremendous work has been done in developing novel electrocatalysts with optimized structure and component for various electrochemical reactions, including H_2 oxidation, alcohol oxidation, ORR, CO_2 reduction, N_2 reduction, *etc*. Pt and Pt group metals (Ru, Rh, Pd, Os, Ir) are well-known as the most excellent electrocatalysts due to their partially filled *d*-bands, which could

reduce the activation barrier of the reaction and/or facilitate the desorption of the product from the catalyst's surface. Yet, the commercialized catalysts still face severe drawbacks. For example, Pt/C, the most successful commercialized direct methanol fuel cell (DMFC) catalyst, despite its high activity towards methanol oxidation, the strong binding between Pt and the reaction intermediate (mainly CO) quickly blocks the active Pt sites (usually called as "poisoning"), which leads to a great failure of the catalyst performance[69]. Consequently, to overcome the intrinsic drawbacks and improve the catalytic performance, Pt-based bimetallic, and trimetallic catalysts, such as Pt-Ru, Pt-Ni, Pt-Pd, Pt-Au *etc*., have been developed in recent years[70,71].

In terms of designing the catalysts, three fundamental effects must be taken into consideration: ensemble effect, ligand (electronic) effect, and geometric (strain) effect [72,73].

1.4.1 Ensemble effect

The ensemble effect arises from the surface of the catalyst consisting of multiple metal components. The introduction of guest metal could adjust the ensemble size of catalytic active site, thus tune the adsorption binding configuration for the reactants or intermediates to enhance catalytic performance[74–77]. Recently, some researchers also ascribed the "oxyphilic effect" or "bifunctional effect" to the ensemble effect[78], which was first proposed by Watanabe and Motoo in 1975[79]. The removal of the poisonous CO intermediates that block the Pt sites is promoted by nearby Ru sites, which activate H_2O dissociation and promote the oxidation of CO to CO_2[80]. It is believed that the CO oxidation follows the Langmuir-Hinshelwood mechanism, where CO_{ads} on Pt site reacts with the adsorbed oxygenated species OH_{ads} on nearby Ru site. Other oxyphilic

elements, such as Au, Sn, Mo, have also been reported to effectively enhance catalytic performance by similar effect when alloying with Pt[81–83].

1.4.2 Ligand effect

The ligand effect, or the electronic effect, occurs when guest metals with dissimilar electronegativities are introduced. The charge transfer between different components modifies the electronic band structure (shifts in *d* band center), thus, varies the adsorption energies of the reactants, intermediates, and products on the catalyst surface. Nørskov and Hammer proposed the "*d*-band center" theory and calculated correlated adsorption of reactive intermediates on the catalyst surface, which have been recognized as the mainstream guide for multimetallic catalysts design[84–87].

1.4.3 Geometric effect

Geometric effect, or strain effect, originates from lattice mismatch between the coating layer and the substrate, commonly seen in core-shell nanostructures[72,88]. For example, the mismatch between the core material and Pt shell results in a strain on the catalytic Pt surface, either compressed or expanded, which tunes the adsorption/desorption of the reactants/intermediate *via* the *d*-band center position shift of Pt. In another word, the strain indirectly influences the electronic structure of Pt, thus tunes the catalytic activity.

For core-shell nanostructure, the lattice distortion is calculated by eqn (5), where a_{shell} is Pt lattice parameter when forming core-shell structure and a_{Pt} is the bulk Pt lattice parameter[72,78]:

$$S_{Pt} = \frac{a_{shell} - a_{Pt}}{a_{Pt}} \times 100\% \quad (5)$$

When tensile stress is identified, the expanded lattice makes the overlap between the *d* electrons on neighboring metal atoms smaller. To keep the *d* occupancy, the *d*-band center would upshift in energy and trigger a stronger interaction between the active sites and the adsorbates. In contrast, the compressive stain would decrease the lattice constant and result in *d*-band center downshift, which would weaken the interaction[78,89]. It is generally accepted that, for ORR, the compressive strain is beneficial for improving Pt-based catalyst performance.

1.5 Synthesis of Hollow nanostructure electrocatalysts

1.5.1 Hollow structure in electrochemistry

Despite tremendous efforts made to design novel electrocatalysts, its commercialization is limited by not only the expensive price of Pt but also loss of catalytic performance due to the poor stability of Pt NPs. The Pt NPs dissolution, redeposition, aggregation, carbon support corrosion and long-term CO poisoning *etc*. have been demonstrated as the main reasons[90]. Therefore, maximizing the activity and stability with minimum cost has become the key issue when designing Pt-based nanocatalysts.

Hollow nanostructures (e.g., nanoshells, nanoframes, nanocages and nanotubes *etc.*) with interior cavities possess advantages such as low density, high surface-to-volume ratio, large loading capability, and highly exposed active sites with significantly reduced amount of noble metal. Therefore, they attract increasing research interest in the field of energy storage and catalysis[91–93]. Given their superior advantages and vast applications, various strategies have been put forward to synthesize hollow

nanostructures, among which the wet-chemistry method is considered as one of the most versatile and convenient ways[94]. Aiming at improving catalytic performance, both thermodynamic and kinetic factors are taken into consideration during the synthesis to optimize the structure, such as tunable void size, wall porosity, surface composition and active sites *etc*.

The wet-chemistry based synthesis strategies can be categorized based on either the template species involved or the mechanism adopted in the reaction.

Template-directed methods, either hard templates (e.g., SiO_2, polystyrene (PS) spheres, polycarbonate (PC), metallic NPs, anodic aluminum oxide (AAO), *etc.*) or soft templates (e.g., polymer vesicles, micelles, emulsions, gas bubbles, *etc.*) are widely employed. By fine tuning the template geometry, hollow nanostructures with various shapes, such as tubular, cubic, polyhedral, bowl-like shapes *etc.* can be achieved[95–97]. Moreover, complex architectures, such as multi-shell or shell with multiple inner chambers, can also be achieved by controlling the reaction parameters, such as annealing process, solvent composition, types of precursors, pH *etc*[92,94].

From the mechanism view, general synthesis mechanisms include galvanic replacement reaction, Kirkendall effect, and selective etching *etc.* Here we briefly introduce recent progress on hollow nanostructure synthesis based on different mechanisms.

1.5.2 Synthesis strategies of hollow nanostructures

1.5.2.1 Galvanic replacement reaction

The driving force of galvanic replacement reaction is the redox potential difference between the templates and the metallic salt precursors[96]. Xia *et al.* first demonstrated

the synthesis of hollow Au nanostructures by a galvanic replacement reaction with Ag templates in 2002 (Figure 1.7a)[98]. The metallic precursor with higher redox potential will oxidize and dissolve the templates while the reduced metal atoms will deposit on the template surface and form the shell[97,99]. The standard electrochemical potentials serve as the theoretical basis to allow the researchers choose thermodynamically favored metal pairs. Other factors, such as pH, temperature, ligands, that can influence the standard redox potential are utilized to further adjust the reaction both thermodynamically and kinetically[100–103].

1.5.2.2 Kirkendall effect

Kirkendall effect at the nanoscale was first reported by Alivisatos *et al.* in 2004[104]. The small voids results from the unbalanced counterdiffusion of the reactive species through a reaction interface accumulate and generate central hollow space in the NP (Figure 1.7b1)[105]. Since then, Kirkendall effect has been extensively exploited in the synthesis of hollow nanostructures consist of metal oxide, metal sulfide, metal selenide, and metal phosphide, such as Fe_2O_3, CdS, $ZnAl_2O_4$, Ag_2Se, NiP, Pt_3Ni *etc.* (Figure 1.7b2 and b3)[106–112]. Factors such as crystalline defects, reaction temperature, sizes of the NPs influence the surface diffusion kinetics thus the void formation[113,114]. Coupling Kirkendall effect with galvanic replacement reaction could further expand the structural and compositional diversity of hollow nanostructures (Figure 1.7c)[115].

1.5.2.3 Selective etching and dealloying

Selective etching and dealloying has been employed as a common treatment to selectively remove part of components to generate hollow structures, either through chemical treatment or calcination (Figure 1.7d1-d3). It is applied to a variety of core materials, such as SiO_2, Au, Prussian Blue, *etc*[116–119].

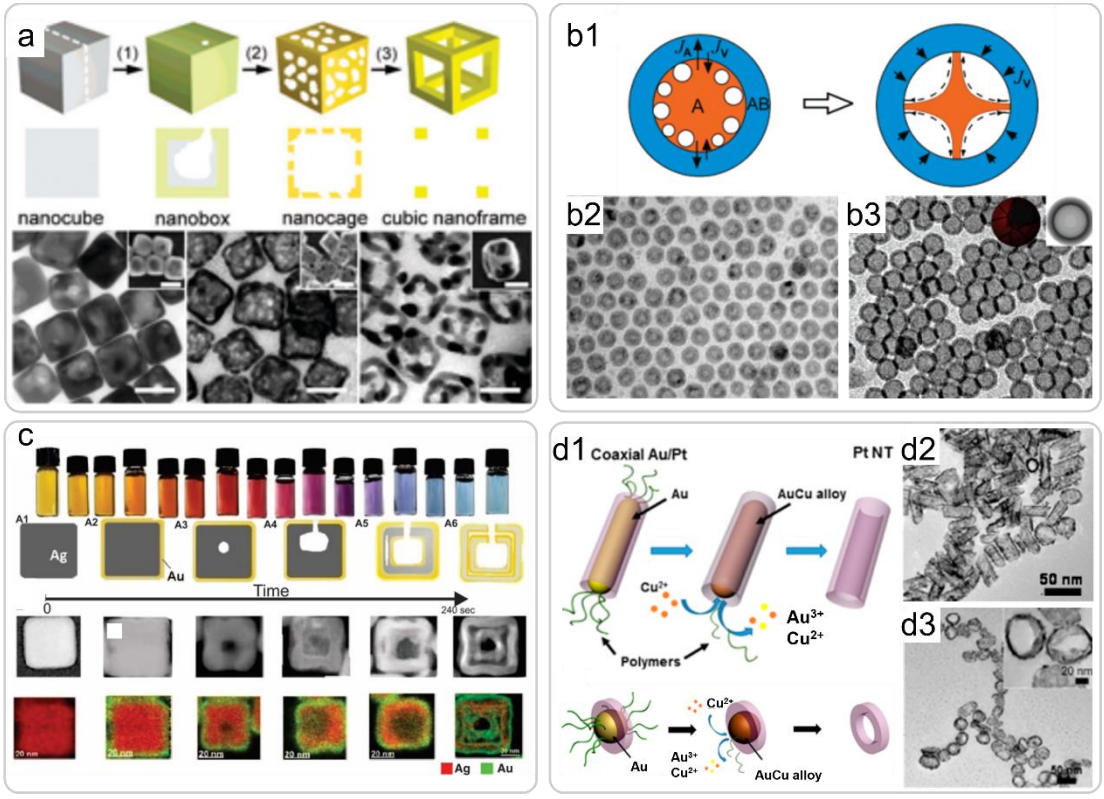

Figure 1.7 Synthesis strategies based on galvanic replacement reaction, Kirkendall effect, and selective etching. (a) Schematic of Au/Ag nanocage and Au nanoframes from Ag nanocubes and the corresponding TEM images[120]. (b1) Schematic for hollow structure formation based on Kirkendall effect; (b2-b3) TEM images of (b2) cobalt sulfide[104] and (b3) γ-Fe_2O_3[109] synthesized *via* Kirkendall effect. (c) Optical and morphological evolution of AuAg double-walled nanoboxes and the corresponding HAADF STEM and TEM images[115]. (d1-d2) Mechanism of Pt NT and Pt nanoring

formation through alloying-etching; (d3) the corresponding TEM images of (d2) Pt NTs and (d3) Pt nanorings[117].

1.5.3 One dimensional (1D) hollow nanostructure in electrocatalysis

Among various hollow nanostructures, 1D hollow nanostructures attract special research interest not only because they possess the advantages of traditional hollow nanostructures but also exhibit additional merits correlated with their anisotropic nature, structural rigidity and lower number of lattice boundaries and defects. Specifically, 1) 1D hollow NTs with open ends expose both interior and exterior surfaces to the reaction environment which provide sufficient active reaction sites and enlarge the electrolyte/catalysts contact area to increases Pt utilization; 2) the anisotropy offers easier electron and mass transportation, which could enhance its electrochemical catalytic performance; 3) the structural stability makes them serve as self-supporting catalysts in electrochemical reaction, which extends the lifetime of the catalysts by avoiding carbon support usage and consequent carbon corrosion, Pt dissolution, ripening and aggregation; 4) the confined interior void space may offer opportunities to control local reactant concentration, which improve the selectivity and activity of the catalytic reaction[90,91,121].

The morphology extension along the longitudinal direction is the key challenge in 1D hollow nanostructure synthesis. Thus, template-directed method by exploiting 1D nanomaterials as the templates is the most widely used strategy to synthesize high quality 1D NTs. Pure metal and multimetallic NTs, such as Pt, Pd, Au, PtNi, PdAu, PdAuCu, PtPdCu *etc.*, have been successfully fabricated by employing AAO as hard templates (Figure 1.8a-c)[122–126]. The components of the NTs can be changed by simply

varying the species of the precursors and the ratio among them during the electrodeposition process. ZnO nanorod array is another type of the most employed hard templates which can be dissolved after electrodeposition by a weak alkali solution. Multimetallic NTs, P-doped alloy NTs and multishell NTs, such as PtP, PtRu, PtPdAg, PdNiCoCuFe, Pd/PANI/Pd *etc.*, are successfully synthesized with ZnO template (Figure 1.8d and 1.8e)[127–133].

Template-directed galvanic replacement reaction is another commonly used method to achieve 1D NTs. Metallic nanowires (NWs) frequently involved includes Ag, Cu, Te *etc*[134–139]. Yu *et al.* employed active Te and Cu NWs as templates and successfully synthesized multimetallic NTs, such as PtCu, PtPdCu, PtPdRuTe *etc.* (Figure 1.8f)[140–142]. The low standard reduction potentials make the Te and Cu templates to be completely consumed after the reaction, avoiding additional template removal steps. Yan *et al.* employed Ag NWs as templates to synthesize Pt NTs and PtPd NTs[143]. The Pt NTs (50 nm diameter, 5-20 μm long and 4-7 nm wall thickness, Figure 1.8g1) maintained the tubular structure as confirmed by TEM and only lost 20% of its electrochemical surface area (ECSA) after 1000 cycles in 0.5 M H_2SO_4, compared to the 51% ECSA loss and 90% ECSA loss of commercial catalysts Pt/black and Pt/C who aggregated heavily after scanning, demonstrating their superior stability which benefited from the 1D NT morphology (Figure 1.8g2). Both Pt NTs and PtPd NTs exhibited enhanced specific activity towards ORR, which were 3.8 times and 5.8 times higher than that of Pt/C, respectively (Figure 1.8g3). Additionally, NTs with complex inner structures, such as segmented tubes or multishell NTs can be achieved by

combining Kirkendall effect with the galvanic replacement reaction or utilizing galvanic replacement repeatedly[105].

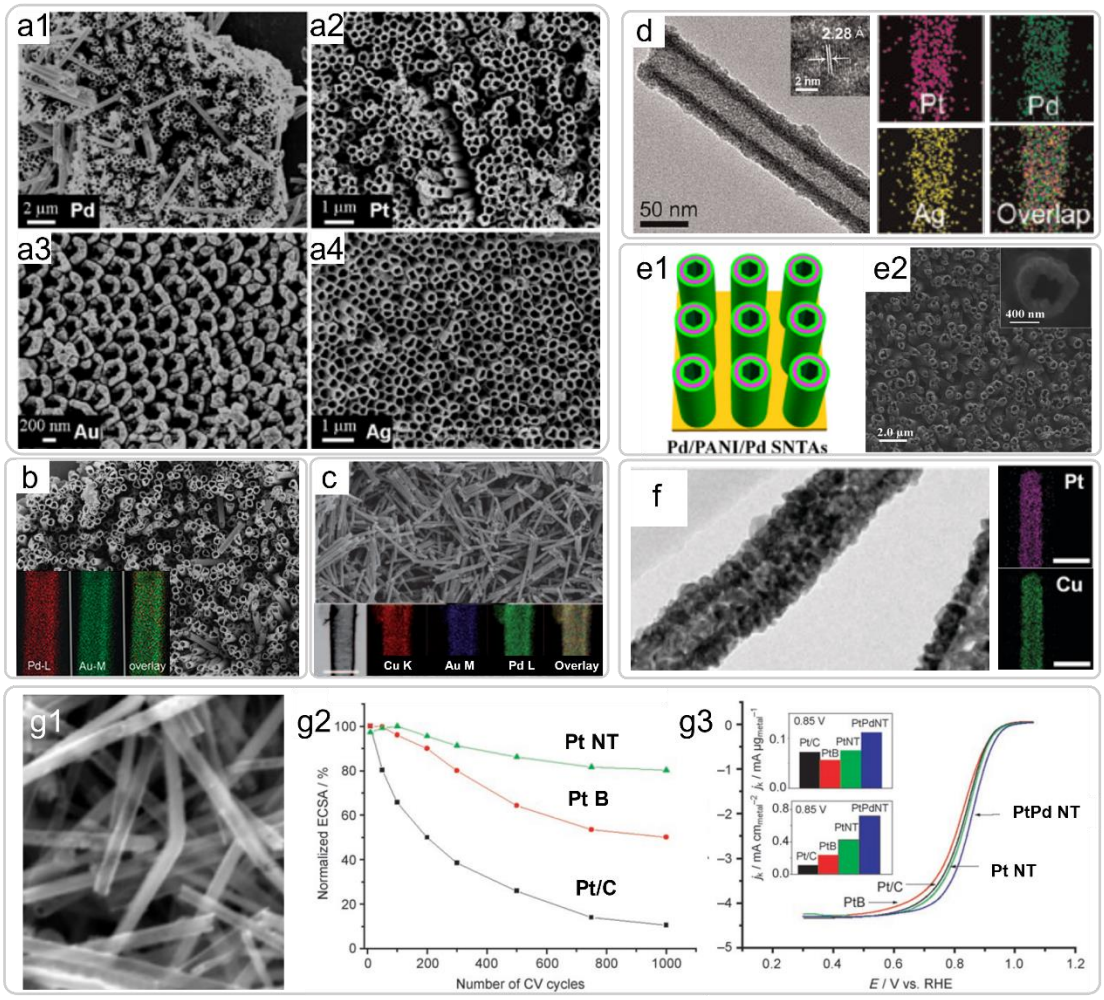

Figure 1.8 (a1-a4) TEM images of Pd, Pt, Au and Ag NTs, respectively[126]. (b) TEM image and corresponding EDX mappings of Pd-Au NTs fabricated from AAO template[123]. (c) TEM image and corresponding EDX mappings of PdAuCu NTs fabricated from AAO template[124]. (d) TEM image and corresponding EDX mappings of Pt-Pd-Ag NTs employing ZnO nanowires as sacrificial templates[130]. (e1) Schematic of fabrication of Pd/PANI/Pd NTs; (e2) SEM image of as-synthesized Pd/PANI/Pd NTs[133]. (f) TEM image and corresponding EDX mappings of PtCu NTs[140]. (g1) SEM

image of Pt NTs; (g2) ECSA loss of Pt NTs, Pt/black and Pt/C after 1000 CV cycles in Ar-purged 0.5 M H_2SO_4, respectively; (g3) ORR curves of Pt NTs, PdPt NTs, Pt/black and Pt/C in O_2-saturated 0.5 M H_2SO_4 solution. Insets are mass activity and specific activity for the four catalysts at 0.85 V[143].

1.5.4 Special topic on the Au-based NT research progress

Among various hollow tubular nanostructures, Au-based NTs, not only possess traditional advantages, such high surface-to-volume ratios, high loading capacity, lower density, but also exhibit additional unique advantages results from its anisotropic morphology. Extension in the longitudinal direction not only enhances electron conductivity and structural stability but also introduces additional parameters in tuning its LSPR band. Up to now, Au-based NTs have been reported to be utilized in bioimaging[144–146], sensor[147–152] and catalysis[153–158]. Here we briefly summarize recent progress of Au-based NTs synthesis and their applications.

The synthesis of Au-based NTs has been a great challenge due to the difficulties in 1) breaking symmetry during the synthesis and 2) keeping both ends open[145,159,160]. Up to date, most Au-based NTs are synthesized by adopting anisotropic hard templates, in which AAO and Ag NWs/NRs are most frequently employed.

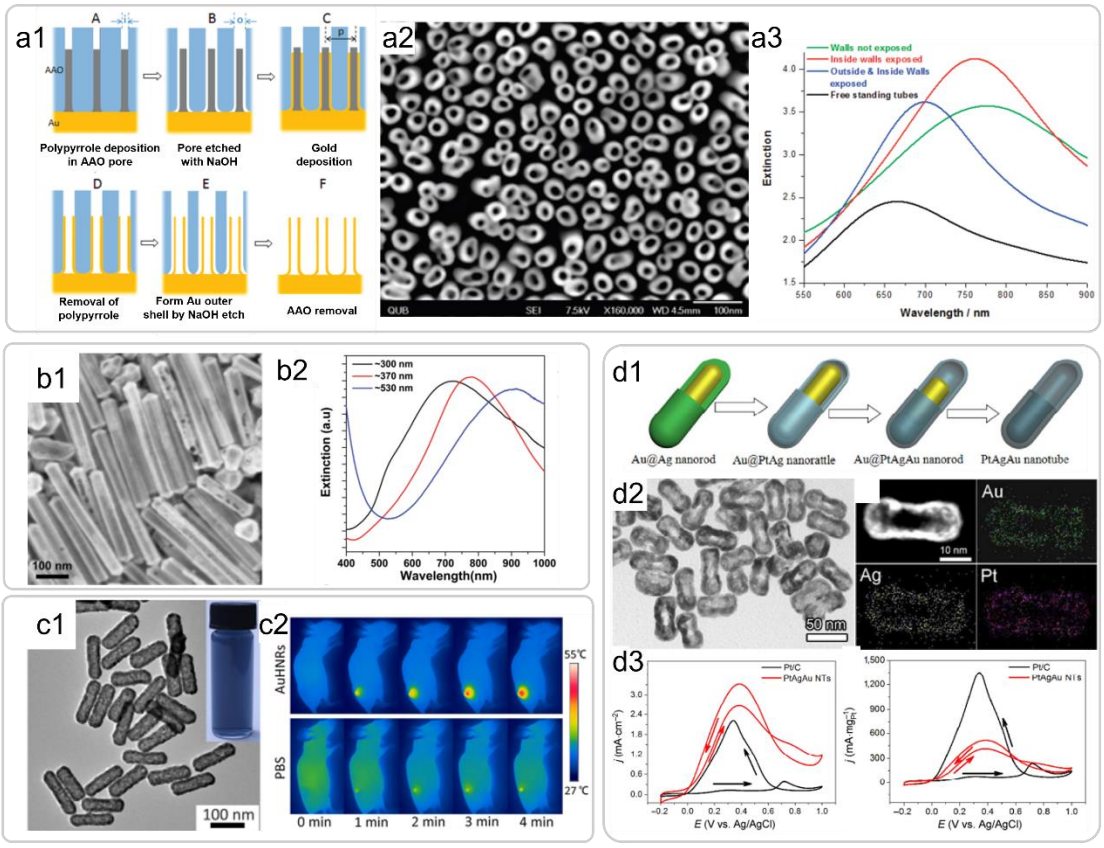

Figure 1.9 (a1) Schematic of the fabrication process of Au NTs using AAO template; (a2) SEM image of the Au NTs; (a3) Extinction spectra obtained for Au NTs at different fabrication stages[148]. (b1) SEM image of Au NTs and (b2) UV-vis spectra of Au NTs of different lengths[145]. (c1) TEM images of hollow Au NRs, inset is photograph of hollow AuNRs solution; (c2) Photothermal images of mice treated with hollow AuNRs[146]. (d1) Schematic of PtAgAu hollow NT synthesis; (d2) TEM, HAADF and EDX mapping of a single PtAgAu hollow NT; (d3) Specific and mass normalized CVs of PtAgAu hollow NTs towards formic acid oxidation in a mixed solution of 0.5 M H_2SO_4 and 0.5 M HCOOH[155].

McPhillips *et al.* fabricated aligned Au NT arrays *via* electrodeposition of Au around polypyrrole NRs in AAO template (Figure 1.9a1 and 1.9a2)[148]. A broad extinction peak in the range of 650-675 nm corresponding to the transverse plasmonic mode of Au NTs was observed after complete removal of both polypyrrole and AAO templates (Figure 1.9a3). The free standing Au NTs were recognized as potential label-free sensors owing to their competitive sensitivity of 225 nm per refractive index unit among other Au-based LSPR structures with resonances around 650 nm and an outstanding signal-to-noise ratio upon protein binding.

Au-based NTs can also be fabricated by combining galvanic replacement reaction with dealloying process. Xia *et al.* employed Ag NWs as sacrificial templates to achieve Au-Ag NTs with pinholes on the wall[12]. The galvanic replacement reaction between gold precursor ($AuCl_4^-$) and the Ag templates generated Au-Ag alloyed NTs with smooth walls while maintaining the morphology features of the templates. Further dealloying process resulted in pure Au NTs with pinholes in the walls. If coating the smooth Au-Ag alloy NTs with an additional Ag layer by electroless plating and repeating the aforementioned galvanic replacement reaction, Au-Ag alloyed NTs with multishells can be fabricated[161]. The resulting Au-Ag NTs were 1-2 μm in length and ~ 100 nm in width. The LSPR peak can be shifted up to 1000 nm by adjusting the amount of $AuCl_4^-$ added or by the number of the shells inside the tubular structure. However, the acquired NTs had poor length and width tunability with broad size distribution, which prohibited them from serving as a model system for systematic LSPR study of Au-based NTs.

It is well-known that the morphology of the hollow nanostructures depends highly on the templates. Evans and co-workers adopted shorter Ag NRs with narrower length

distribution as templates and successfully synthesized Au-Ag NTs with tunable lengths down to 300 nm *via* galvanic replacement reaction (Figure 1.9b1)[145]. The control over the lengths of the Au-Ag NTs allowed more precise manipulation over the LSPR band shift. By increasing the length of the Au-Ag NTs from 300 nm to 530 nm, an obvious LSPR band red-shift from 700 nm to 950 nm was observed, with the latter located in the biological transparent window (Figure 1.9b2). The poly (sodium 4-styrenesulfonate) coated Au-Ag NTs displayed low cytotoxicity, capability of photothermal ablation of tumor cells and excellent photoacoustic signal enhancement at the tumor site, offering its potential applications in photothermal therapy and photoacoustic imaging. Zhai *et al.* employed Se-doping of Te nanorods as templates and synthesized hollow Au NRs within 150 nm (Figure 1.9c1)[146]. Despite the decreased dimension, the LSPR band of the hollow Au NRs could be tuned into the second NIR window (1000-1350 nm) by varying the ARs (length/width). The hollow Au NRs were demonstrated to be nontoxic and capable of loading drugs. *In vivo* study further revealed that the hollow Au NRs could serve as contrast agents in multimodel imaging (Figure 1.9c2).

Au-based NTs have also been applied in the field of catalysis. Ding *et al.* synthesized Pt/Au porous NTs by the galvanic replacement reaction between $[PtCl_6]^{2-}$ and Ag residual in AuAg alloy NTs[153]. The elemental ratio between Pt and Au can be tuned by varying the feeding ratio between the Pt salt precursor and the AuAg alloy NTs. The porous Pt/Au NTs exhibited higher electrocatalytic activity towards formic acid oxidation compared to pure Pt NTs due to the aforementioned “bifunctional effect”. Yang *et al.* reported a one-step synthesis of trimetallic PtAuAg NTs by employing

Au@Ag core-shell NRs as templates, in which Ag layer played dual roles as reducing the Pt salt precursor and assisting the oxidation of Au core (Figure 1.9d1 and d2)[155]. Cyclic voltammetry (CV) revealed that the PtAuAg NTs oxidized formic acid *via* direct dehydrogenation of HCOOH to CO_2 and exhibited enhanced activity towards formic acid oxidation compared to that of commercial Pt/C (Figure 1.9d3).

1.6 Scope of the dissertation

As discussed in earlier sections, the rational design of plasmonic-catalytic conjugate photoelectrocatalyst systems plays a vital role in directing light energy to drive chemical transformation. The photoelectrocatalyst should meet the following requirements: (1) intrinsic high electrocatalytic activity; (2) a tunable LSPR band in the visible-NIR range, and (3) effective energy flow from the plasmonic entity to the catalytic entity. In this dissertation, I have chosen Au, which is chemically stable under corrosive electrocatalytic environments, as the plasmonic entity and Pt, which is considered as one of the most active electrocatalysts, as the catalytic entity. The aim of this dissertation is to develop the synthetic strategy of hybrid PtAu NTs, to investigate the tunability of their LSPR bands in the visible-NIR range and to improve photoelectrocatalytic performance under visible-NIR light irradiation.

Chapter 2: Synthesis of ultrathin Pt nanotubes *via* critical micelle concentration mediated heterogeneous deposition

Overview

In this chapter, we developed a novel approach to synthesize ultrathin Pt nanotubes (NTs). The ultrathin Pt NTs were synthesized by a templated deposition of an ultrathin layer Pt on the templates followed by a selective template removal. The ultrathin Pt layer deposition was controlled by the concentration of the surfactant (c_{surf}^{+}) in the reaction system. This method was demonstrated as a reproducible and scalable method to fabricate hollow Pt NTs compared to conventional methods.

This chapter is adapted from the manuscript in preparation: Zhang, Q., Yi, C. L., Shen, X. X., Huang, Z. Q., Guo, H. Y., Yu, S. J., Webb, K., Lamar, C., Lin, X.Y., Kong, C.C., Lee, S. B.*, Nie, Z. H.*, Synthesis of Ultrathin Pt Nanotubes *via* Critical Micelle Concentration Mediated Heterogeneous Deposition

2.1 Introduction

Pt and Pt based hollow nanostructures have attracted extensive attention in both research and industrial fields. Compared with their solid counterparts, they show a low density, high surface-to-volume ratio, and high-volume capacity, and thus exhibit enhanced performance in catalysis, biomedicine, and optics[162–164]. The use of ultrathin hollow nanostructures helps to increase the utilization efficiency of Pt as a scarce noble metal. Typical strategies for the synthesis of hollow nanostructures include galvanic replacement reaction[165], Kirkendall effect[115], and seed-mediated deposition followed by selective removal of templates[166], *etc*., with the later as one of the most popular ways. Both thermodynamic and kinetic factors are taken into consideration when designing the nucleation and growth of Pt on the templates. Thermodynamically, Pt

prefers an island growth mode (Volmer-Weber mode) on the surface of the template (e.g., Pd nanoparticles) due to the strong binding energy of the Pt-Pt bond[167–170]. A slow reduction of metal precursors at a relatively high temperature in the synthesis is an essential prerequisite for the diffusion of the newly formed Pt atom across the surface of Pd templates to form a complete ultrathin Pt overgrowth layer[171]. The slow reduction rate is often achieved by precisely controlling the addition rate of the Pt precursors *via* a syringe pump[170], using a Pt precursor with low solubility[172], or coordinating the Pt precursor with strong binding ligands[169]. However, these strategies are either time consuming, or require delicate synthesis skills, which restrict them from large-scale fabrication. Consequently, there is an urgent need to develop a synthesis method to produce ultrathin Pt hollow structure initiated by an ultrathin Pt layer deposition on the template, which is simple, scalable, and reproducible.

Adopting long alkyl chain surfactants to control the nucleation process exhibits great influence in ultrathin nanomaterial fabrication. The long alkyl chain surfactant not only serves as templates but also coordinate with the metal precursors to alter the nucleation kinetics. In aqueous solution, the cationic quaternary ammonium compounds (QACs) are widely used to control the synthesis of metal nanoparticles (NPs) through the following aspects: (i) forming metal ion-cationic surfactants complex (denoted as Surf-M, e.g., CTA^+-$AuCl_4^-$, $[CTA^+]_2$-$PtCl_4^{2-}$, $[CPC^+]_2$-$PdCl_4^{2-}$) to lower the redox potential[173–176]; (ii) solubilizing the Surf-M complexes in soft templates of micellar structures[177,178]; (iii) impacting the NP growth by binding halide counterions to a specific crystal facet; and (iv) stabilizing the NPs by forming an electrostatic double layer on NPs' surface. Benefiting from these advantages, much effort has been focused

on using QACs as soft templates at c_{surf}^{+} above its critical micelle concentration (CMC) at the growth stage to control shaped NP synthesis, e.g., Au nanorods (NRs), Pd nanocubes, *etc*[168,179–181]. Although various large-scale synthesis methods have been well-established using QACs to synthesize shaped NPs with easy control, few reports have focused on utilizing QACs to control the nucleation stage in ultrathin layer heterogeneous deposition.

Herein, we report a facile strategy to control the templated deposition of Pt to synthesize hollow Pt NTs with ultrathin walls by modulating the c_{surf}^{+} of QACs. When Au/Pd coaxial NRs were used as the templates, at c_{surf}^{+} < CMC, the complexes formed by QAC surfactants and the Pt precursors (Surf-Pt) in aqueous phase aggregated into tiny clusters to initiate the generation of stable Pt nuclei with sizes above its critical radius which allows Pt heterogeneous deposition on the surface of Pd to produce an ultrathin Pt layer. The subsequent removal of Au and Pd of the templates produced high-quality hollow Pt NTs with controlled wall thickness (2.0 ± 0.3nm). In contrast, at c_{surf}^{+} > CMC, the incorporation of Surf-Pt complexes in the micelles formed by QACs reduced the localized concentration of the Pt precursor, thus hindered the heterogeneous Pt deposition. This synthetic strategy shows at least the following three advantages over existing methods for ultrathin hollow Pt nanostructure synthesis: (i) it can be implemented for scalable synthesis in aqueous solution; (ii) it does not require a high reaction temperature (≥80˚C), and (iii) it is applicable to other types of commonly used QACs. The ultrathin hollow Pt NTs were examined as catalysts for methanol oxidation reaction (MOR). The specific activity is about 2 times higher than

that of commercial Pt/C, indicating it may find applications in catalysis and energy conversion field.

2.2 Experiments

2.2.1 Materials

Gold (III) chloride trihydrate ($HAuCl_4 \cdot 3H_2O$, 99.9+%), silver nitrate ($AgNO_3$, 99+%), potassium tetrachloroplatinate (II) (K_2PtCl_4, 98+%), palladium (II) chloride ($PdCl_2$, 99+%), hydrochloric acid (HCl, 36.5%-38%), hexadecyltrimethylammonium bromide (C_{16}TAB, 99%), benzyldimethyldodecylammonium chloride (BDAC or BAC-C_{12}, 99.0%), octylbenzyldimethylammonium chloride (BAC-C_8, 96.0+%), decylbenzyldimethylammonium chloride (BAC-C_{10}, 97.0+%), tetradecylbenzyldimethylammonium chloride dihydrate (BAC-$C_{14} \cdot 2H_2O$, 98%), hexadecylbenzyldimethylammonium chloride (BAC-C_{16}, cationic detergent), octyltrimethylammonium bromide (C_8TAB, 98+%), decyltrimethylammonium bromide (C_{10}TAB, 98+%), dodecyltrimethylammonium bromide (C_{12}TAB, 98+%), tetradecyltrimethylammonium bromide (C_{14}TAB, 99+%), sodium borohydride ($NaBH_4$, 99.99%), L-ascorbic acid (AA, 99+%), copper (II) chloride dihydrate ($CuCl_2 \cdot 2H_2O$, 99.0+%), ethanol (200 proof), ethylene glycol (anhydrous, 99.8%), tetrahydrofuran (THF), dimethylformamide (DMF) were all purchased from Sigma-Aldrich. Methanol (CH_3OH, Reagent Grade) was purchased from PHARMCO, sulfuric acid (H_2SO_4, 95-98%) were purchased from Alfa Aesar. Nafion solution (5 wt.%) was purchased from Sigma-Aldrich.

HPLC water was used in all the experiment and was purchased from Sigma-Aldrich. Hexadecyltrimethylammonium chloride (CTAC, >95%) was purchased from TCI. Thiol-terminated polystyrene (PS-SH, Mn=12,000, Mw/Mn =1.09) was purchased from Polymer Source Inc.

All the chemicals were used as received without further processing.

2.2.2 Preparation of PS-tethered Au NRs

Au NRs were prepared by following the previous work published by our group. A seed solution was first prepared as follows: 2.5 mL of 0.2 M CTAB aqueous solution, 0.125 mL of 10 mM $HAuCl_4$ and 2.375 mL of water were well-mixed in a 20 mL scintillation vial, followed by injection of 0.3 mL of ice-cold 10 mM $NaBH_4$ aqueous solution under vigorous stirring. After stirring for 2 minutes at room temperature, the solution was kept at a 30 ˚C water bath for 2 hours before use. In the growth solution, 0.5 mL of 10 mM $AgNO_3$ aqueous solution and 2.5 mL of 10 mM $HAuCl_4$ aqueous solution were added sequentially to 47.5 mL of 0.1 M CTAB aqueous solution, followed by injection of 0.3 mL of 0.1 M AA aqueous solution. Then 0.8 mL of as-prepared Au seed solution was quickly injected. After gently shaking, the growth solution was kept at 30 ˚C water bath overnight. The 50 mL of as synthesized Au NRs was separated and concentrated by centrifugation. The supernatant was carefully removed, and the Au NRs was concentrated to 0.2 mL. The solution was then added dropwise into a 10 mL of THF containing 4 mg of PS-SH. The solution was sonicated for another 30 minutes and incubated overnight at room temperature. Then the PS-modified Au NRs was washed with THF for 6 cycles and re-dispersed in 4 mL DMF. Following, 2 mL solution of DMF/H_2O (60/40 wt %) was added dropwise under gentle shaking. The solution was

kept still for 3 hours. Then 1mL of the mixture was added dropwise in 9 mL of H_2O containing 1 mL of 0.2 M CTAB and the aqueous solution was used for Pd growth.

2.2.3 Synthesis of PS-tethered Au/Pd coaxial NR templates

Au/Pd coaxial NR templates were synthesized as follows. 1.6 mL of 10 mM H_2PdCl_4 was mixed with 20 mL of the PS-tethered Au NRs solution, followed by adding 0.8 mL of 0.1 M AA aqueous solution. After gentle shaking, the reaction was kept at 30 ˚C water bath overnight. The as-prepared PS-tethered Au/Pd coaxial NRs were separated by centrifugation and washed twice with water at 14,000 rpm for 15 min. During the washing steps, BDAC was added to avoid aggregation of the Au/Pd coaxial NRs. The supernatants must be completely removed in order to decrease the CTAB residue in the solution. The Au/Pd coaxial NRs were redispersed in 2 mL of water before further use.

2.2.4 Fabrication of ultrathin Pt NTs by using Au/Pd coaxial NR templates

0.1 mL of the as-prepared Au/Pd coaxial NR templates was dispersed in 0.9 mL of water containing 37.5 μL of 0.2 M BDAC. 24 μL of 10 mM K_2PtCl_4 and 96 μL of 10 mM KBr aqueous solution were added sequentially, followed by the addition of 15 μL of 10 mM AA aqueous solution. After gentle mixing, the reaction was kept at 80 ˚C water bath for 3 hours. After cooling down, the sample was washed with DMF and dispersed in 4 mL of 4mM $CuCl_2$/DMF solution at 60 ˚C to etch away the Au/Pd coaxial NR templates. After 6 hours, the sample was separated by centrifuge and washed with DMF twice then redispersed and kept in 1 mL water for further use.

2.2.5 Deposition of Pt on Au/Pd coaxial NR templates in the presence of ethanol (EtOH) or ethylene glycol (EG)

To investigate the influence of organic additives on the Pt deposition process, 0.8, 0.7 and 0.4 mL of water containing 37.5 μL of 0.2 M BDAC were added to 4 mL vials, respectively. Next, 0.1, 0.2 and 0.4 mL of EtOH or EG were introduced to each vial, respectively. Then 0.1 mL of the as-prepared Au/Pd coaxial templates was dispersed in the mixed solution in each vial followed by the addition of 24 μL of 10 mM K_2PtCl_4 and 96 μL of 10 mM KBr aqueous solution. After gentle mixing, the reaction was kept at 80 ˚C water bath for 3 hours. The template etching followed the same procedure as described above.

2.2.6 Investigation of the influence of different QACs

All the QAC solutions used were of 0.2 M. The volume of the QAC solution added in each vial was adjusted according to its CMC.

To investigate the influence of the BAC-C_n, 340, 760, 900, 891 and 900 μL of water were added to 4 mL vials, respectively. Next, 560 μL of 0.2 M BAC-C_8, 140 μL of 0.2 M BAC-C_{10}, 37.5 μL of BAC-C_{12}, 8.3 μL of BAC-C_{14} and 0.83 μL of BAC-C_{16} were introduced into each vial, respectively. Then 0.1 mL of the as-prepared Au/Pd coaxial NR templates was dispersed in the mixed solution in each vial followed by the addition of 24 μL of 10 mM K_2PtCl_4 and 96 μL of 10 mM KBr aqueous solution. After gentle mixing, the reaction was kept at 80 ˚C water bath for 3 hours. The template etching followed the same procedure as described before.

For the C_nTAB group of surfactants, 340, 620, 816, 886 and 896 μL of water were added to 4 mL vials, respectively. Next, 560 μL of 0.2 M C_8TAB, 280 μL of 0.2 M

C_{10}TAB, 84 μL of C_{12}TAB, 14 μL of C_{14}TAB and 3.3 μL of C_{16}TAB were introduced into each vial, respectively. Then 0.1 mL of the as-prepared Au/Pd coaxial NR templates was dispersed in the mixed solution in each vial followed by the addition of 24 μL of 10 mM K_2PtCl_4 and 96 μL of 10 mM KBr aqueous solution. After gentle mixing, the reaction was kept at 80 ˚C water bath for 3 hours. The template etching followed the same procedure as described before.

2.2.7 Morphological, structural, and elemental characterizations

Transmission electron microscopy (TEM) images were taken using a JEOL LaB6 microscope operated at 200 kV. High-resolution TEM (HRTEM), high-angle annular dark-field scanning TEM (HAADF-STEM) and energy dispersive X-ray (EDX) analyses were performed using a JEOL 2100F microscope (JEOL, Tokyo, Japan) operated at 200 kV. Visible-NIR extinction measurements were performed using Shimadzu UV-2501PC UV-Vis recording spectrophotometer. The dynamic light scattering (DLS) study was carried out using Zetasizer Nano ZS 90 Malvern Instruments.

2.2.8 Preparation of the DLS test

0.2 M BDAC, 10mM K_2PtCl_4 and 10 mM of KBr aqueous solution were employed as the stock solutions, respectively. The K_2PtCl_4 and KBr were mixed by a volume ratio of 1:4 before the DLS test. Different volumes of the surfactant solution were mixed with water and the solution concentrations were presented in Table 2.1. Then 240 μL of K_2PtCl_4 and KBr mixed aqueous solution was added in the diluted surfactant solution 5 minutes before the DLS test.

2.2.9 Electrochemical tests

The electrocatalytic tests were performed on a CHI 660A electrochemical workstation. A three-electrode system was adopted. A glassy carbon electrode (GCE) (diameter 3mm) was used as working electrode (WE), Ag/AgCl (3M KCl) was used as the reference electrode and a graphite rod was used as the counter electrode. The catalyst ink was prepared by adding as-prepared ultrathin Pt NTs into a mixture of water (180 µL), ethanol (50 µL) and Nafion (20 µL). A total volume of 2 µL of the catalyst ink was then dropcast onto the surface of a cleaned GCE and dried at room temperature. The ink preparation for the commercial Pt/C (purchased from Fuel Cell Store, 20% Pt on Vulcan XC-72R) was the same as that of Pt NTs. The electrochemically active surface area (ECSA) was calculated based on integration the hydrogen adsorption charge obtained by cyclic voltammetry (CV) with a scanning rate of 50 mV s^{-1} in 0.5 M H_2SO_4 solution. The MOR was performed in a freshly prepared N_2-saturated mixture solution containing 0.5 M H_2SO_4 and 1.0 M methanol solution at a scanning rate of 50 mV s^{-1}.

Table 2.1 Different concentrations of the surfactant solution used in the DLS

# of the vial	Volume of BDAC stock solution (μL)	Volume of HPLC water (μL)	Volume of K_2PtBr_4 and KBr (μL)	Conc. of BDAC in diluted solution (mM)
1	5	1995	240	0.45
2	9.9	1990.1	240	0.88
3	24.7	1975.3	240	2.20
4	48.8	1951.2	240	4.35
5	72.5	1927.5	240	6.47
6	95.7	1904.3	240	8.54
7	140	1860	240	12.5
8	180	1820	240	16.0
9	263	1737	240	23.4
10	335	1665	240	29.9
11	400	1600	240	35.7
12	560	1440	240	50
13	600	1400	240	53.5
14	800	1200	240	71.4
15	1120	880	240	100
16	1344	656	240	120
17	1680	320	240	150
18	2000	0	240	178.5

2.3 Results and discussion

2.3.1 Synthesis and characterization of Au/Pd coaxial NR templates and ultrathin Pt NTs at c_{BDA}^{+}< CMC

The scheme in Figure 2.1 illustrates the concept of surfactant concentration-mediated deposition of ultrathin Pt on the surface of the template. In a typical synthesis, Au/Pd coaxial NRs with collapsed polystyrene (PS) domains at both ends were used as a model system of the templates[182]. BDAC was selected to provide BDA^+ cations during the synthesis and KBr was added to facilitate the nucleation process. In the reaction, $PtCl_4^{2-}$ ions first reacted with Br^- ions to form $[PtCl_xBr_{4-x}]^{2-}$ (denoted as Pt (II) for simplicity) and then with BDA^+ to produce BDA-Pt (II) ion-pair complexes[100]. The Pt (II) concentration was kept low to ensure a slow deposition rate. At c_{BDA}^{+}< CMC, the BDA-Pt (II) complexes aggregated into tiny clusters with an increased local concentration of Pt (II), due to the charge neutralization of the oppositely charged BDA^+ and Pt (II). The reduction of Pt (II) in the BDA-Pt (II) cluster form followed the classic LaMer nucleation mode and triggered a burst of nucleation to form stable Pt nuclei (LaMer classical model), enabling the heterogeneous deposition of Pt on the surface of Pd to form a thin yet smooth metallic layer. The subsequent removal of the Au/Pd NR templates produced Pt NTs with ultrathin wall. In contrast, at c_{BDA}^{+} >CMC, only few BDA-Pt (II) complexes were incorporated in each BDA micelle (relative to a much larger aggregation number of BDA molecules in the micelles). The low local concentration of the Pt (II) distributed in the micellar structure prohibited the formation of stable nuclei above its critical radius, and hence prevented the deposition of Pt on the surface of Pd heterogeneously.

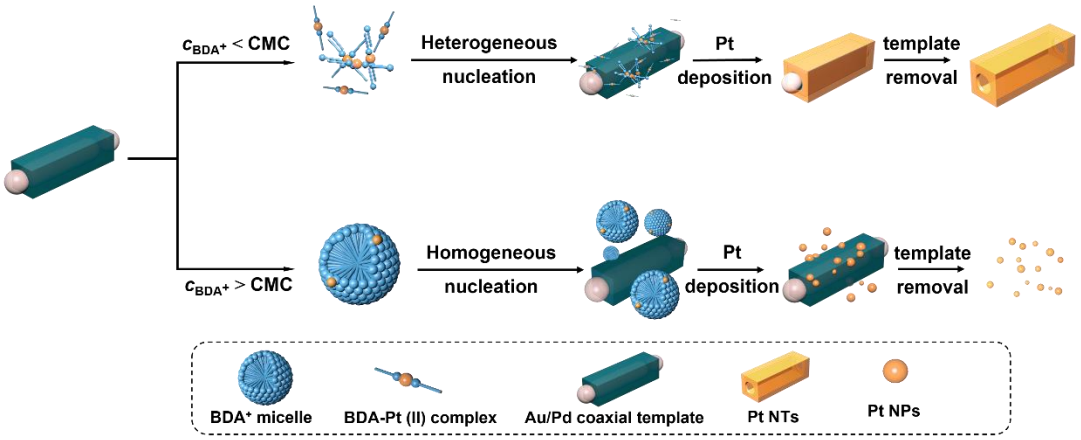

Figure 2.1 Schematic illustration of the experimental procedures for the fabrication of ultrathin hollow Pt NTs by CMC guided heterogeneous nucleation process.

Transmission electron microscopy (TEM) image in Figure 2.2a presents the Au/Pd template ((47.6 ±5.3) × (24.5±2.2) nm, length× width) containing a central Au NR ((30.4 ± 3.4) × (12.5 ± 2.2) nm, length× width) and a 6 nm thick layer of Pd. The Au/Pd templates are enclosed by Pd {100} facets, as indicated by a 0.2 nm interplanar distance of the Pd layer in the high-resolution TEM (HRTEM) image (Figure 2.3a). At c_{BDA^+}< CMC (8.8 mM for BDAC[183]), after the deposition of Pt to form Au/Pd/Pt nanostructure, the original flat and smooth surface of Au/Pd templates became rougher (Figure 2.2b). The continuous lattice fringes from the Pd layer to the Pt shell in the HRTEM image suggests the epitaxial growth of Pt on Au/Pd templates *via* the heterogeneous nucleation (Figure 2.2c). The Fast Fourier Transform (FFT) pattern shows that the (002) plane of Pt is growing on (002) plane of Pd along the [001] direction of the Pd crystal unit cell (inset of Figure 2.2c). The coating of a continuous Pt layer is further confirmed by the bright thin line on the outer surface of the Au/Pd template in the high-angle annular dark-field scanning TEM (HAADF-STEM), the corresponding energy-

disperse X-ray (EDX) elemental mapping, and EDX line scanning profile (Figure 2.2d and Figure 2.3c). The selective etching and removal of the Au/Pd templates by Cu^{2+}/DMF[117] produced ultrathin hollow Pt NTs with relatively uniform intact Pt wall (Figure 2.2e). The average thickness of the Pt wall was measured to be 2.0 ± 0.3nm (Figure 2.2f). The cross-section of the Pt NTs exhibits a square-shaped solid frame structure (inset in Figure 2.2f), which is inherited from the geometric configuration of the Au/Pd templates (Figure 2.3b). The 0.22 nm interplanar distance of the Pt frame and the selective area electron diffraction (SAED) image further reveals the formation of pristine polycrystalline Pt layer (Figure 2.2g-h). The reaction can be easily scaled up to fabricate Pt NTs with high uniformity and dispersity up to ~0.1 gram (Figure 2.3d).

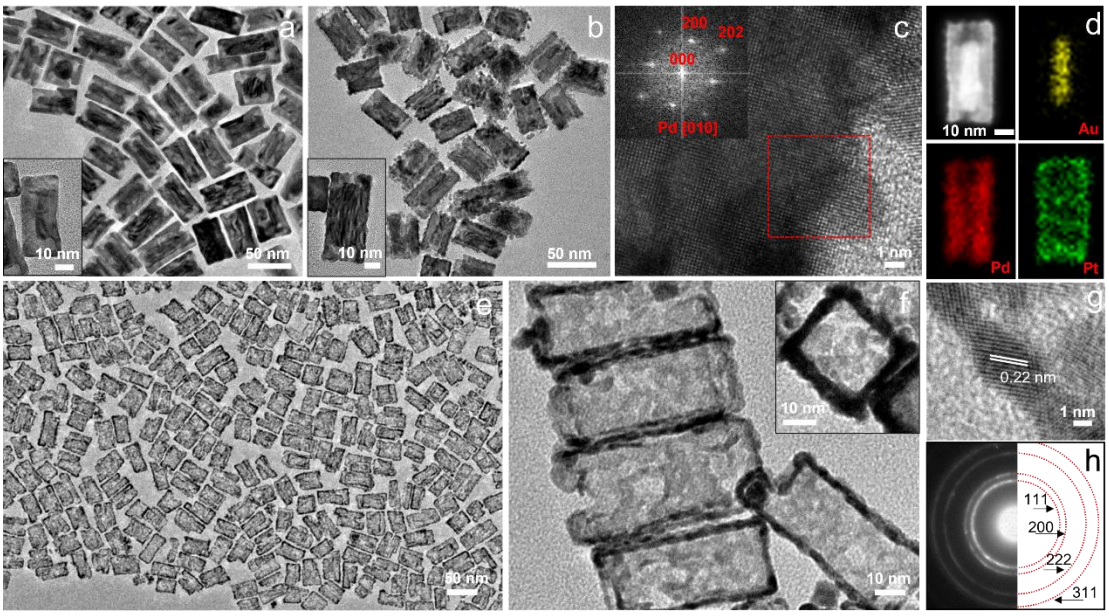

Figure 2.2 (a-b) TEM images of the Au/Pd templates before Pt deposition and Au/Pd/Pt nanostructure after Pt deposition, respectively. The insets present a single nanostructure correspondingly. (c) HRTEM image of the Au/Pd/Pt nanostructure and the inset is the SAED of the squared area. (d) HAADF-STEM image and the EDX

mapping of an individual Au/Pd/Pt nanostructure. (e) TEM image of ultrathin Pt NTs after template removal. (f) TEM image of single Pt NTs and the inset shows the intersection view of a single Pt NT. (g) HRTEM image taken from the Pt NT frame and (h) the SAED pattern of the Pt NTs.

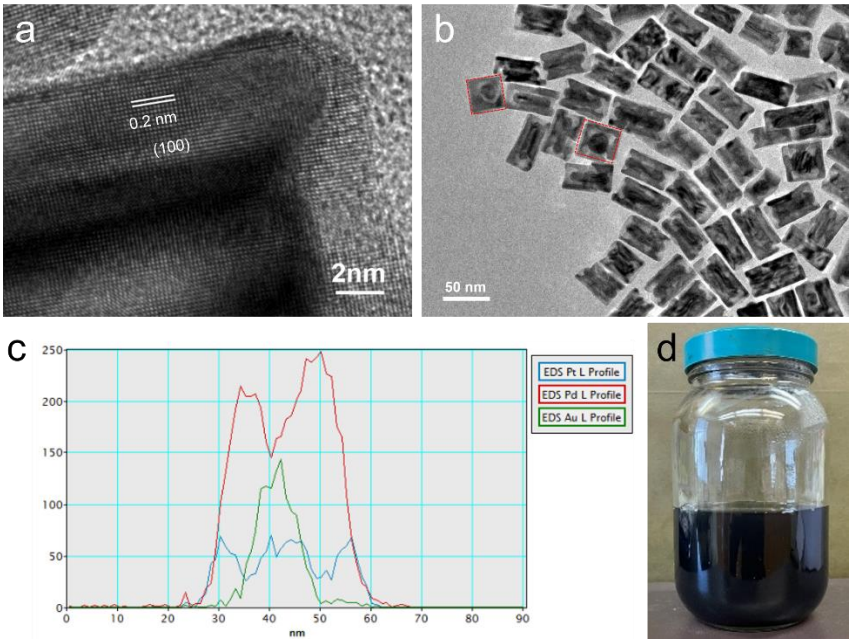

Figure 2.3 (a) HRTEM image of Au/Pd coaxial NR template enclosed by Pd {100} facets. (b) TEM image of intersection views of Au/Pd templates which are squared by the red frames. (c) EDX line scanning of Au/Pd/Pt nanostructure after depositing an ultrathin layer of Pt when c_{BDA}^{+} < CMC. (d) Photo image of large-scale fabrication of ultrathin hollow Pt NTs. The solution (180 mL) contains ~ 0.1 gram of Pt NTs.

2.3.2 Deposition of Pt on Au/Pd coaxial NR templates at c_{BDA}^{+} > CMC

At c_{BDA}^{+}> CMC, after Pt deposition, no obvious roughness on the surface of the resulting Au/Pd/Pt nanostructure was observed as compared with the original Au/Pd

template (Figure 2.2a and Figure 2.4a). Additionally, no continuous bright Pt layer was detected outside the Au/Pd template by HAADF-STEM (Figure 2.4b) in contrast to that of Au/Pd/Pt nanostructure synthesized when c_{BDA}^{+}< CMC (Figure 2.2d). The EDX mapping together with the line scanning (Figure 2.4b and 2.4d) further confirm very low content of Pt sparsely dispersed around the Au/Pd templates. After the removal of the templates, only collapsed Pt fragments rather than intact Pt NTs were obtained (Figure 2.4c).

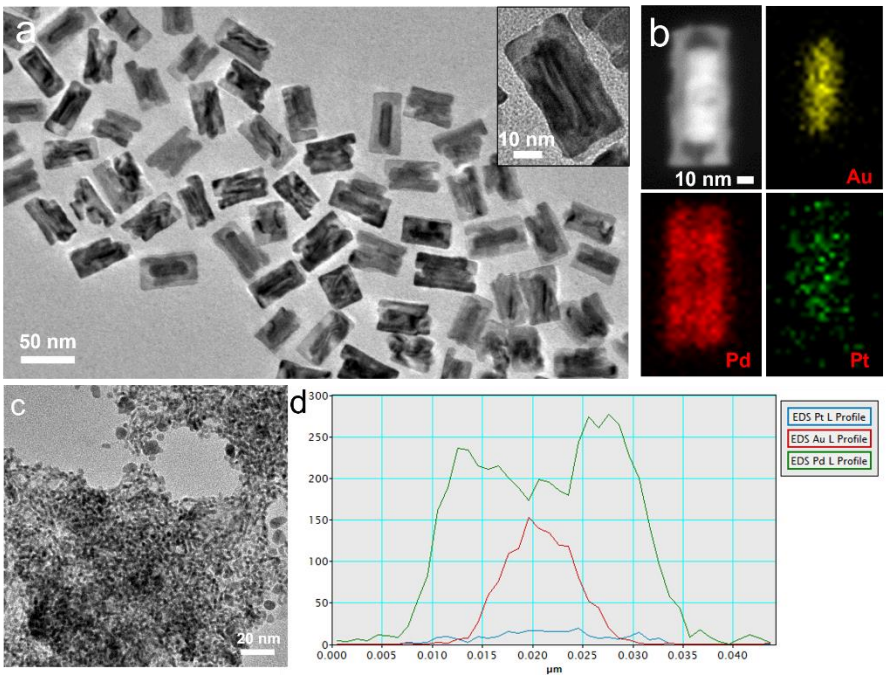

Figure 2.4 (a) TEM image of the Au/Pd/Pt nanostructures after Pt deposition when c_{BDA}^{+} > CMC, the inset presents a single Au/Pd/Pt nanostructure. (b) HAADF-STEM image and the EDX mapping of individual Au/Pd/Pt nanostructure and (c) TEM image of the resulted collapsed Pt fragments after removing Au/Pd templates. (d) EDX line scanning of Au/Pd coaxial template after Pt deposition when c_{BDA}^{+} > CMC.

2.3.3 Investigation of the role of c_{BDA^+} in the Pt deposition process

The deposition of Pt is strongly dependent on the c_{BDA^+} relative to its CMC. We systematically investigated the effect of c_{BDA^+} on the deposition of Pt on the Au/Pd template surface. At all the c_{BDA^+} below the CMC we studied, the reaction yielded Pt NTs with hollow interior and open ends after the removal of Au/Pd template (Figure 2.5a-e and Table 2.1). However, when c_{BDA^+} << CMC (0.45 and 0.88 mM), the weak electrostatic repulsion provided by BDA^+ resulted in heavy aggregation of the Au/Pd templates (Figure 2.6a). Thus, heavily aggregated Pt NTs with rough surfaces were produced (Figure 2.5a-b and Figure 2.6b). Pt NTs with increased dispersity and wall thickness uniformity were obtained as c_{BDA^+} approached to CMC (2.2 mM ~ 6.47 mM, Figure 2.5c-e). At $c_{BDA^+} \approx$ CMC (8.5 mM), the synthetic process yielded porous hollow tubular structures that are partially collapsed (Figure 2.5f). We attribute this to the reduced amount of BDA-Pt (II) clusters and hence Pt nuclei formed in the reaction, due to the incorporation of BDA-Pt (II) complexes in the BDA^+ micelles. With the further increase in c_{BDA^+} above CMC, all the BDA-Pt (II) complexes were solubilized in the BDA^+ micelles, rather than associated into tiny clusters. The heterogeneous deposition of Pt on the surface of Au/Pd templates was largely suppressed, leading to the formation of collapsed and aggregated Pt fragments (Figure 2.5g-i).

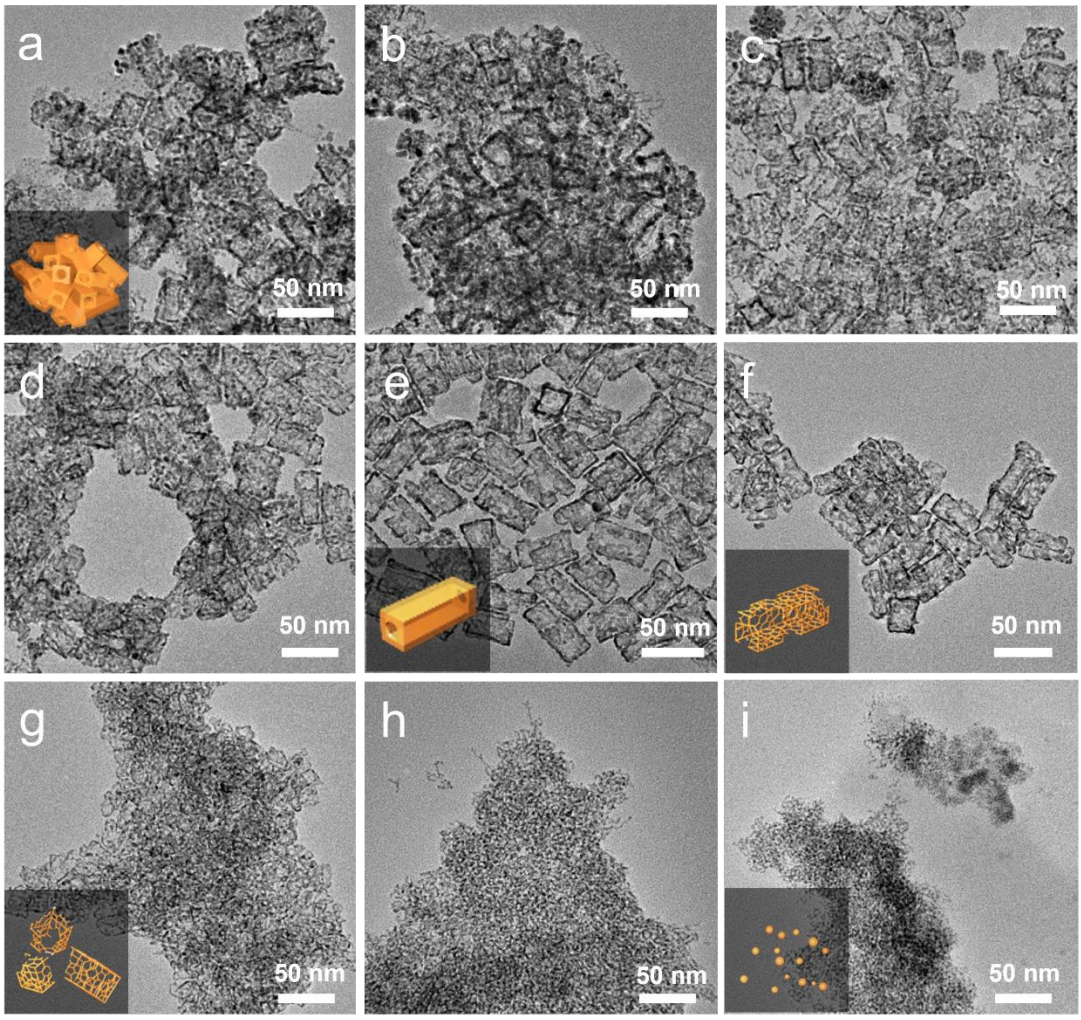

Figure 2.5 (a-e) TEM images of the acquired Pt NTs after the template removal when c_{BDA^+} < CMC: (a) 0.45 mM, (b) 0.88 mM, (c) 2.20 mM, (d) 4.35 mM and (e) 6.47 mM; when $c_{BDA^+} \approx$ CMC (f):8.54 mM and when c_{BDA^+} > CMC (g-i): (g) 12.5 mM, (h) 16.07 mM and (i) 23.48 mM. The insets show the corresponding schematic structural models of the Pt products after template removal.

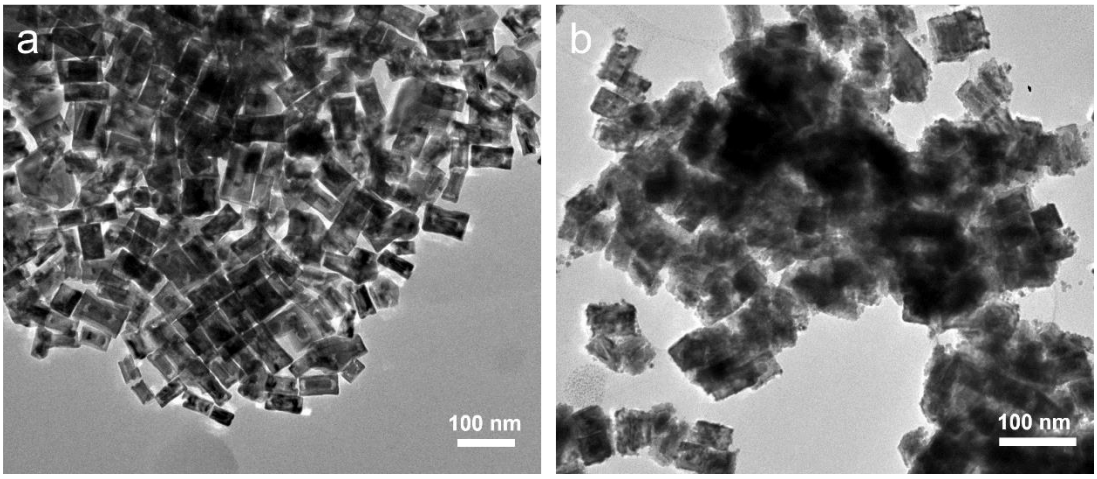

Figure 2.6 TEM images of (a) heavily aggregated Au/Pd templates after the excess removal of BDAC from the reaction and (b) heavily aggregated Au/Pd/Pt nanostructure after Pt deposition.

2.3.4 Investigation of BDA-Pt (II) association by DLS

DLS was used to investigate the association behavior of BDA-Pt (II) complexes and their incorporation in micelles. At c_{BDA^+}<CMC, the hydrodynamic radius of the BDA-Pt (II) clusters gradually decreases, and the peak becomes narrower with the increase of c_{BDA^+}, due to more insertion of BDA^+ to the BDA-Pt (II) clusters, which helps to solubilize the clusters[184] (Table 2.1 and Figure 2.7a). As c_{BDA^+} increased beyond its CMC, the DLS data presented two distinct peaks with one at ~2 nm and the other beyond 100 nm (Figure 2.7b and 2.7c). The former corresponds to individual BDA^+ micelles incorporated with BDA-Pt (II) complexes, whereas the latter corresponds to a secondary assembly structure of the BDA^+ micelles[185,186]. The DLS data is consistent with our visual observation (Figure 2.7d). Upon the mixing of BDA^+ with Pt (II) precursors, the solution became turbid, indicating the formation of insoluble clusters of BDA-Pt (II) complexes. In the region of 1st CMC < c_{BDA^+}< 2nd CMC[183], the BDA-Pt

(II) complexes continuously solubilized into the BDA^+ micelles and the solution gradually turned into clear. At $c_{BDA}{}^+ > 2^{nd}$ CMC, the BDA-Pt (II) complexes completely incorporated into the micellar structures and the solution became completely clear.

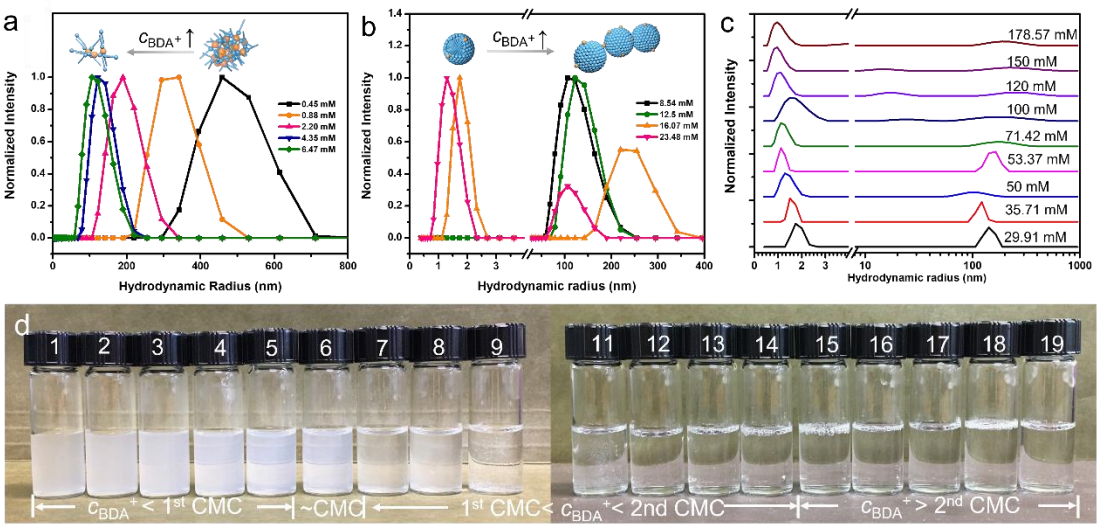

Figure 2.7 DLS data of (a) BDA-Pt (II) clusters when $c_{BDA}{}^+ <$ CMC and (b-c) its solubilization in micelle when $c_{BDA}{}^+ > \approx$ CMC, respectively. The insets present the schematic illustrations of the solubilization process. (d) The visual observation of BDA-Pt (II) complex with different $c_{BDA}{}^+$. The number on each vial corresponds to $c_{BDA}{}^+$ values listed in Table 2.1.

2.3.5 Morphological evolution during the heterogeneous Pt deposition

We monitored the time-dependent deposition of Pt on the surface of Au/Pd templates by withdrawing samples at different reaction stages. At $c_{BDA}{}^+ <$ CMC, when t = 5 min, we observed ultrafine Pt NPs attached to the template surface and be around the templates, indicating both homogeneous and heterogeneous nucleation of Pt happened immediately after the reaction started (Figure 2.8a1). As the reaction proceeded, the surface of the template became obviously rougher (t = 30 min, and 1-3h, Figure 2.8a2-

5). The corresponding Pt NTs after the template removal at different reaction stages reveal the gradual formation of Pt NTs (Figure 2.9). The HRTEM images (Figure 2.10) disclose the attachment of the Pt nuclei and confirm that through the overlap and fusion of the nuclei, a continuous Pt shell was formed. In contrast, at c_{BDA}^{+} > CMC, no obvious Pt deposition on the template was observed throughout the reaction (Figure 2.8b1-5), indicating the heterogenous deposition was largely prohibited. After template removal, the incomplete Pt coverage was not sufficient to maintain the integrity of Pt NTs, thus producing collapsed Pt fragments.

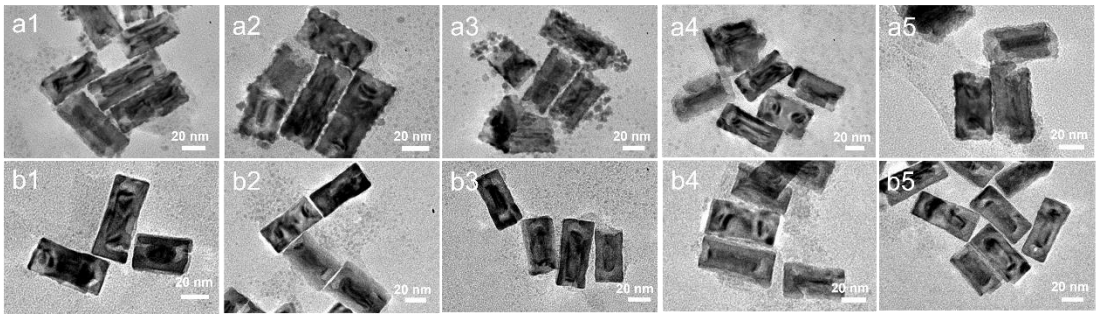

Figure 2.8 TEM images of the morphology evolution of the Au/Pd/Pt nanostructure in the time-dependent Pt deposition when c_{BDA}^{+} < CMC (a1-a5) at 5 min, 30min, 1h, 2h and 3h, respectively; and when c_{BDA}^{+} > CMC (b1-b5) at 5 min, 30min and 1h, 2h and 3h, respectively.

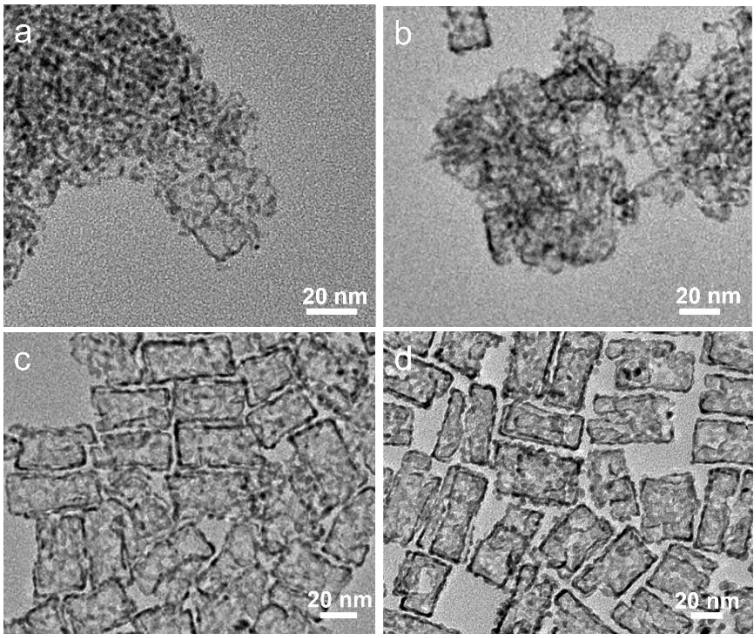

Figure 2.9 TEM images of Pt nanostructures obtained at different reaction stages after removing Au/Pt templates: (a) 0.5 h, (b) 1h, (c) 2 h and (d) 3h.

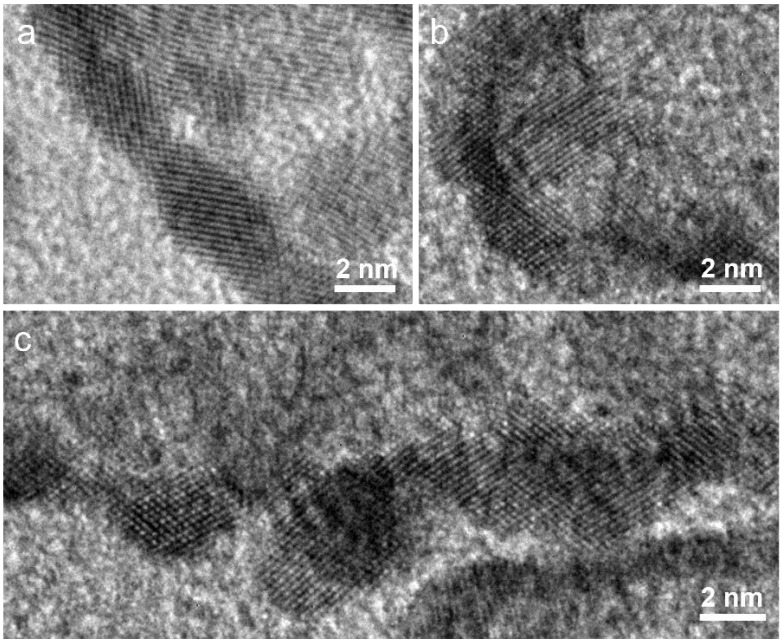

Figure 2.10 HRTEM images taken from a single ultrathin Pt NT showing the attachment of the Pt nuclei.

2.3.6 Effect of organic additives on Pt deposition process

The heterogeneous deposition of Pt can be regulated by modulating the CMC of BDAC through the addition of small organic molecules. In a reaction system with c_{BDA^+} > CMC, which was originally unfavored the formation of intact Pt NTs (corresponding to the condition in Figure 2.5g), the addition of ethanol (EtOH) and ethylene glycol (EG) resulted in the formation of intact Pt NTs, due to the increase in the CMC of BDAC in the mixed solvents[187–189]. With increasing the content of the added EtOH, the morphology of the products transited from collapsed Pt fragments (Figure 2.5g) to porous Pt nanoframes (Figure 2.11a) and eventually to intact Pt NTs (Figure 2.11b). A similar trend was observed when EG was used (Figure 2.11d and 2.11e). However, as the concentration of EtOH and EG increased to ~40 vol%, aggregated Pt NTs with rough surfaces were obtained (Figure 2.11c and 2.11f), owing to the Au/Pd template aggregation caused by reduced electrostatic repulsion among the templates with increased amount of EtOH and EG. Meanwhile, both EtOH and EG could serve as weak reducing agents to accelerate the reduction of BDA-Pt (II) complexes.

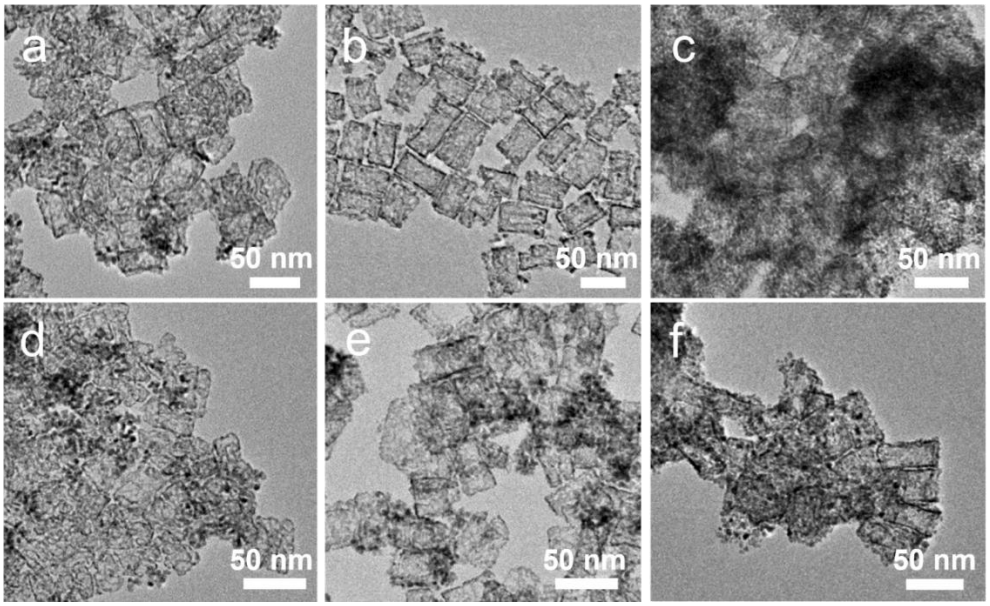

Figure 2.11 TEM images of the Pt products after template removal when introducing organic additives with different concentrations in the system: (a-c) EtOH added with different vol%: (a) 10%, (b) 20%, (c) 40%; (d-f) EG added with different vol%: (d) 10%, (e) 20% and (f) 40%.

2.3.7 The strategy generality in other QAC systems

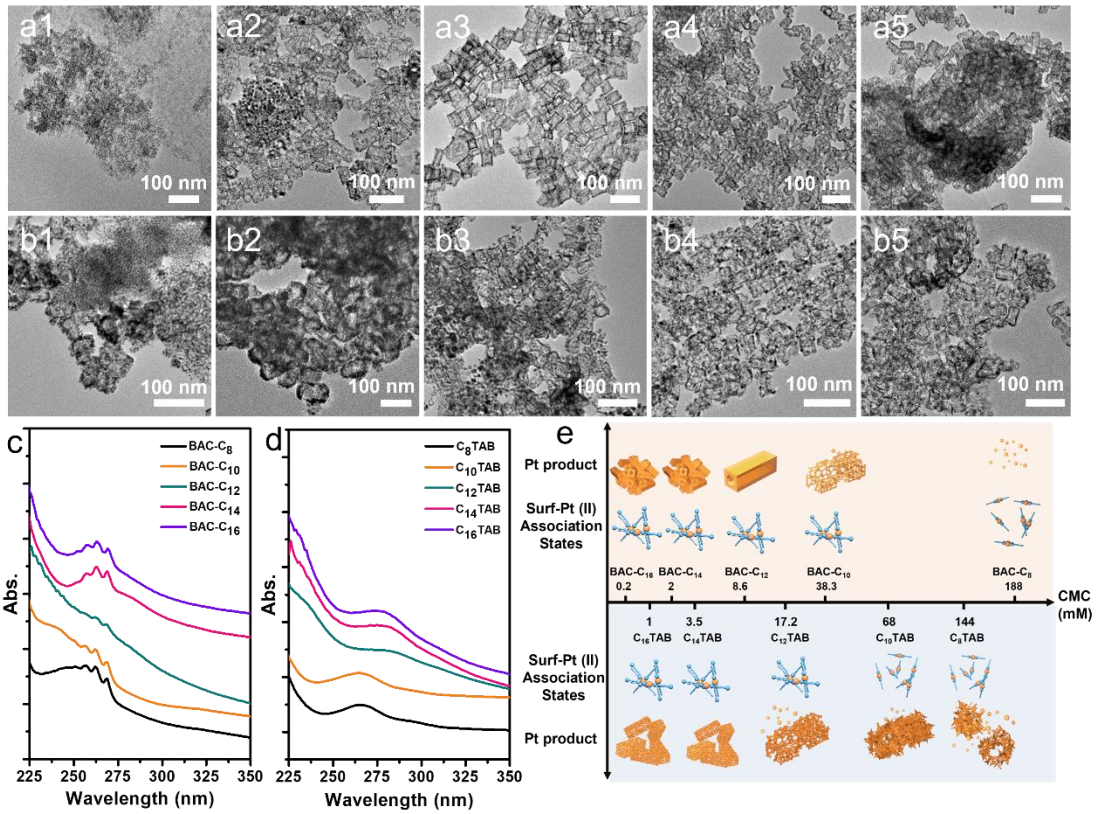

Figure 2.12 (a1-a5) TEM images of Pt products by using BAC-C_n as surfactants, n= 8, 10, 12, 14 and 16, respectively. (b1-b5) TEM images of Pt products by using C_nTAB as surfactants, n= 8, 10, 12, 14 and 16, respectively. (c) UV-vis spectra of the mixture of BAC-C_n and Pt (II). (d) UV-vis spectra of the mixture of C_nTAB and Pt (II). (e) Schematic diagram of Pt products when employing QACs as surfactants.

We further validated the generality of the strategy of ultrathin Pt layer deposition at c_{surf}^{+} < CMC using other QACs with different alkyl chain lengths and CMC values, which include benzyldimethyl ammonium surfactants (BAC-C_n, n= 8, 10, 12, 14 and 16) and trimethyl ammonium surfactants (C_nTAB, n=8, 10, 12, 14 and 16) (Table 2.2). For BAC-C_n group, intact ultrathin Pt NTs were obtained at n≥12, whereas Pt NPs and

collapsed Pt NTs were produced at n=8 and 10, respectively (Figure 2.12a1-5). The C_nTAB group showed a similar trend: surfactants with long alkyl chain preferred to assist intact Pt NTs formation, rather than Pt frame fragments and free Pt NPs (Figure 2.12b1-5). This result can be explained by the different association states of the Surf-Pt (II) complexes when QACs of different alkyl chain lengths were used, as confirmed by UV-visible measurements. When mixing BAC-C_8 with Pt (II), no obvious change was observed in the spectra as compared with those of individual BAC-C_8 and Pt (II), indicating no obvious formation of BAC-C_8-Pt (II) clusters (Figure 2.12c, Figure 2.13a and 2.13b). As the alkyl chain length increased (n=10,12, 14, and 16), a broad band around 275-300 nm became obvious (Figure 2.12c), because of a more complete cluster formation of BAC-C_n-Pt (II) complexes from the enhanced hydrophobic interaction. The influence of the association states of Surf-Pt (II) on the Pt nucleation was further validated by the direct reduction of BAC-C_n-Pt (II) without Au/Pd templates. Rare Pt NPs was observed when n=8 (Figure 2.14a1). As n increased, the enhanced hydrophobic interaction of the alkyl chains facilitated BAC-C_n-Pt (II) complex cluster formation, thus, Pt NPs were obtained (Figure 2.14a2-5). For C_nTAB, the UV band shifted from 260 nm to 280 nm (Figure 2.12d, Figure 2.13a and 2.13c), which also indicates a gradually complete association of C_nTA-Pt (II) as the n value increases from 8 to 16[190]. The direct reduction of C_nTA-Pt (II) complexes showed a similar trend as those of BAC-C_n-Pt (II) when $n \geq 12$ (Figure 2.14b3-5). However, C_8TAB and C_{10}TAB, we speculate that the coexistence of free C_nTA-Pt (II) complexes and C_nTA-Pt (II) clusters induced temporally unseparated nucleation and growth of Pt and led to

giant Pt dendritic nanostructures (Figure 2.14b1 and 2.14b2). The results are summarized as a schematic diagram in Figure 2.12e.

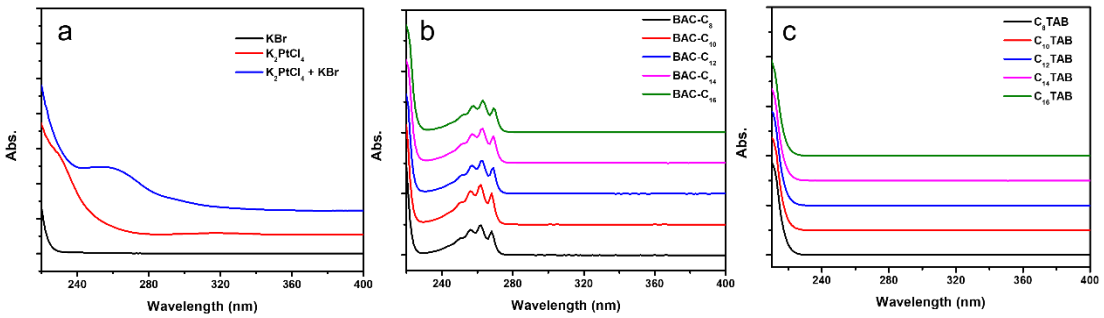

Figure 2.13 UV-Vis spectra of (a) KBr, K_2PtCl_4 and the mixture of K_2PtCl_4 and KBr; (b) BAC-C_n and (c) C_nTAB.

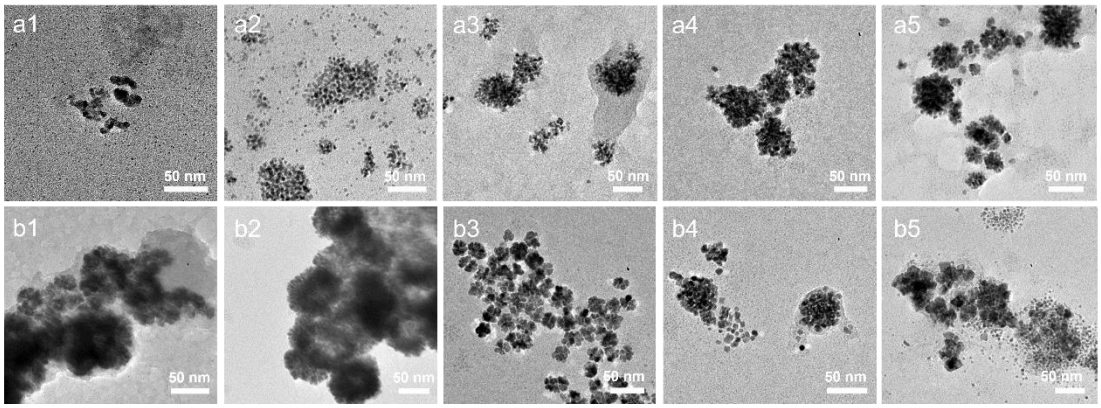

Figure 2.14 TEM images of Pt products synthesized by the direct reduction of different Surf-Pt (II) in the absence of the Au/Pd templates: (a1-5) BAC-C_8, BAC-C_{10}, BAC-C_{12}, BAC-C_{14} and BAC-C_{16}; and (b1-5) C_8TAB, C_{10}TAB, C_{12}TAB, C_{14}TAB and C_{16}TAB.

It is noteworthy that the smaller CMC values of BAC-C_n caused by the benzene ring on the side chain indicate a stronger hydrophobic interaction when forming the BDA-Pt (II) complex clusters, thus Pt NTs synthesized by BAC-C_n were of better wall thickness uniformity compared to those of Pt NTs synthesized by employing C_nTAB (Table 2.2). Meanwhile, for QACs with smaller CMC values, maintaining $c_{surf}^{+} <$ CMC

during the reaction would cause heavy aggregation of the templates, thus, led to heavily aggregated Pt NTs as final products.

Table 2.2 Commonly used QACs with their CMC values[191] and the morphologies of Pt products synthesized by adopting the corresponding QACs

Molecular formula	Abbreviation	CMC (mM)	Pt Product after template removal
BAC-C_n 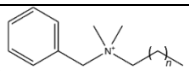			
$CH_3(CH_2)_7N(Cl)(CH_3)_2CH_2C_6H_5$	BAC-C_8	188	Pt NPs
$CH_3(CH_2)_9N(Cl)(CH_3)_2CH_2C_6H_5$	BAC-C_{10}	38.3–38.7	Pt NTs + NPs
$CH_3(CH_2)_{11}N(Cl)(CH_3)_2CH_2C_6H_5$	BAC-C_{12} (BDAC)	8.6	Ultrathin Pt NTs
$CH_3(CH_2)_{13}N(Cl)(CH_3)_2CH_2C_6H_5$	BAC-C_{14}	1.99-2.16	Ultrathin Pt NTs heavily aggregated
$CH_3(CH_2)_{15}N(Cl)(CH_3)_2CH_2C_6H_5$	BAC-C_{16}	0.2	Ultrathin Pt NTs heavily aggregated
C_nTAB 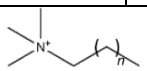			
$CH_3(CH_2)_7N(CH_3)_3(Br)$	C_8TAB	144	Pt NTs (collapsed) + NPs
$CH_3(CH_2)_9N(CH_3)_3(Br)$	C_{10}TAB	68	Pt NTs + NPs
$CH_3(CH_2)_{11}N(CH_3)_3(Br)$	C_{12}TAB	17.2	Pt NTs + NPs
$CH_3(CH_2)_{13}N(CH_3)_3(Br)$	C_{14}TAB	3.5	Pt NTs heavily aggregated
$CH_3(CH_2)_{15}N(CH_3)_3(Br)$	C_{16}TAB	0.99-1.2	Pt NTs heavily aggregated

In a word, in order to prepare ultrathin Pt NTs of high quality (increased dispersity and wall thickness uniformity), the QAC should meet the conditions of (1) the alkyl chains should be long enough to form Surf-Pt (II) clusters and (2) a moderate CMC value which can maintain electrostatic repulsion to avoid template aggregation.

2.3.8 Electrochemical performance of ultrathin Pt NTs

MOR was used as a model electrocatalytic reaction to examine the potential catalytic performance of the ultrathin Pt NTs. The corresponding CV scans are shown in Figure 2.15a. Figure 2.15b further exhibits the histograms of the peak current densities of the ultrathin Pt NTs and commercial Pt/C. The specific activity of the ultrathin Pt NTs is about 0.49 mA/cm^2, which is ~2 times higher than that of the commercial Pt/C (0.25 mA/cm^2). The ultrathin Pt NTs exhibit enhanced MOR activity and could potentially extend its application in energy field.

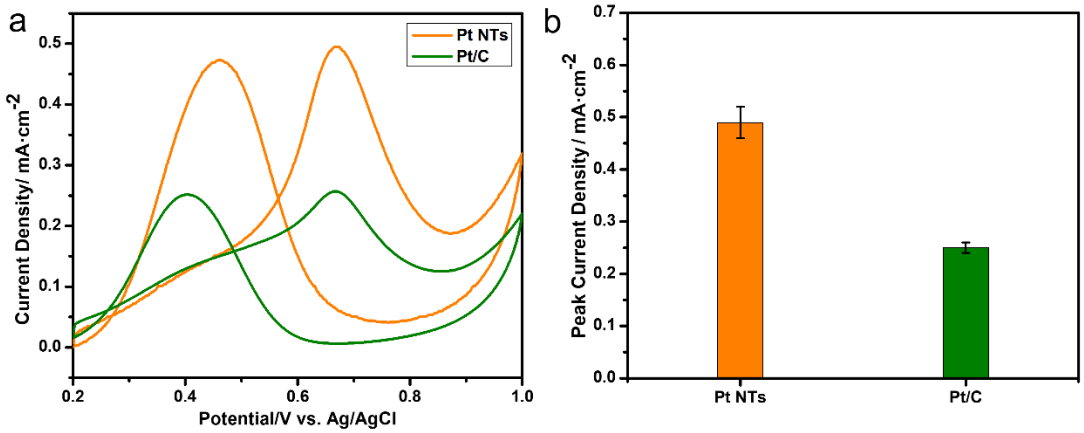

Figure 2.15 (a) CV scans of ultrathin Pt NTs and Pt/C in an aqueous solution of 0.5 M H_2SO_4 and 1.0 M methanol using a scanning rate of 50 mV/s, respectively; and (b) Specific activity comparison between Pt NTs and Pt/C, the error bars are from three independent measurements.

2.4 Conclusions

To conclude, we have developed a novel and facile strategy to synthesize ultrathin Pt NTs in aqueous solution. The heterogeneous Pt nucleation on the templates was

realized when c_{BDA^+} < CMC. It is demonstrated the BDA-Pt (II) complex clusters served as the effective precursors, which created a localized high concentration of Pt (II) that can induce a fast heterogeneous nucleation. This strategy demonstrated its generality when the reaction systems adopted other commonly used QACs.

This approach can be potentially extended to the synthesis of ultrathin hollow Pt nanostructures with different geometries by employing other Pd templates with different shapes (e.g., cubic, octahedral, truncated structures, concaved structures). Moreover, it enables the large-scale synthesis of ultrathin Pt hollow structures with high quality control, which lays the foundation for their practical industrial fabrication and potential application in catalysis and energy conversion field.

Chapter 3: Synthesis of ultrathin PtAu nanotubes with tunable LSPR bands in the visible-NIR range

Overview

In this chapter, a multi-stepwise synthesis was designed to fabricate PtAu NTs. We demonstrated the LSPR band tunability, ranging from 600 nm-820 nm, in the visible-NIR region through control of the length, width, and wall thickness of the PtAu NTs. Furthermore, the LSPR experimental extinction spectra and finite-difference time-domain (FDTD) simulated spectra were analyzed to study the geometric dependent LSPR band shift. It was demonstrated that PtAu NTs exhibited characteristic LSPR features of both rodlike and hollow nanostructures.

A manuscript based on this chapter is in preparation.

3.1 Introduction

Hollow Au-based NTs have been widely employed in bioimaging[145,146,192], sensors[148,193,194] and catalysis[153,155]. However, current synthetic methods are limited. To date, one of the most common strategies for Au-based NT fabrication is the hard template directed synthesis. AAO arrays[195,196] and Ag NWs/NRs[145,161,197] were commonly employed as templates for the synthesis of Au-based NTs that are tens of nanometers in width and hundreds of nanometers in length. Despite the mature fabrication strategies, the dimensions of Au-based NTs, comparable to or beyond the wavelength of the incident light, may weaken its LSPR response.

There are a few reports on the synthesis and optical properties of Au-based NTs smaller than 100 nm; however, the lack of flexible tunability over the NT size confines the

systematical discussion over its LSPR behavior. The LSPR band tunability is only limited to the dependence on the overall length and width of the tubular structures, an analogue analysis to its solid counterpart Au NRs. Nevertheless, the advantages of a hollow structure on the tunability of its LSPR band over the visible-NIR range are not highlighted. Although several simulation studies revealed the LSPR transverse mode of Au NTs[198–201], the LSPR longitudinal mode and its relation to the transverse mode has been rarely reported in tubular systems with a finite length.

In this chapter, we reported the synthesis of PtAu NTs with tunable dimensions, such as length, width, and thickness of the Pt and Au layer, *via* a multi-step, controllable synthesis strategy including: 1) template-directed deposition, 2) selective etching, and 3) underpotential deposition. The extinction LSPR band of obtained PtAu NTs matched with the LSPR extinction simulated by the FDTD method. The longitudinal and transverse LSPR band position dependence on the aspect ratios, including the ratio between the length/thickness, the ratio between width/thickness, the ratio between length/width, and the thickness of the Pt layer and the Au layer, were analyzed systematically. Through delicate control over the dimensions, the LSPR band can be tuned from 600-820 nm in the visible-NIR range. These findings allow for potential applications of PtAu NTs in visible-light driven catalysis.

3.2 Experiments

3.2.1 Materials

Gold (III) chloride trihydrate ($HAuCl_4.3H_2O$, 99.9 +%), silver nitrate ($AgNO_3$, 99+%), potassium tetrachloroplatinate (II) (K_2PtCl_4, 98+%), palladium (II) chloride ($PdCl_2$, 99+%), hydrochloric acid (HCl, 36.5%-38%), hexadecyltrimethylammonium bromide (CTAB, 99%), benzyldimethyldodecylammonium chlorride (BDAC, 99.0%), sodium borohydride ($NaBH_4$, 99.99%), L-ascorbic acid (AA, 99%+), tetrahydrofuran (THF), dimethylformamide (DMF), Nafion solution (5 wt.%), and sodium hydroxide (NaOH) were purchased from Sigma-Aldrich. Methanol (CH_3OH, Reagent Grade) was purchased from PHARMCO, and sulfuric acid (H_2SO_4, 95-98%) was purchased from Alfa Aesar.

HPLC water was used in all the experiments and was purchased from Sigma-Aldrich.

Hexadecyltrimethylammonium chloride (CTAC, >95%) was purchased from TCI.

Thiol-terminated polystyrene (PS-SH, Mn=12,000, Mw/Mn =1.09) was purchased from Polymer Source Inc.

All the chemicals were used as received without further processing.

3.2.2 Seeds solution for Au NR preparation

Seed mediated growth was employed for the synthesis of Au NRs with tunable dimensions. The seed solution was prepared as follows: 2.5 mL of 0.2 M CTAB aqueous solution, 0.125 mL of 10 mM $HAuCl_4$ and 2.375 mL of water were well-mixed in a 20 mL scintillation vial, followed by the injection of 0.3 mL of ice-cold 10 mM $NaBH_4$ aqueous solution under vigorous stirring. After stirring for 2 minutes at room

temperature, the solution was incubated in a 30 ˚C water bath for 2 hours before use. To prepare Au NRs with the longitudinal extinction band at 634 nm, 805 nm and 1032 nm respectively, the growth solutions were prepared separately as follows.

3.2.3 Au NRs with the longitudinal extinction band at 634 nm

In the growth solution, 0.25 mL of 2 mM $AgNO_3$ aqueous solution and 2.5 mL of 10 mM $HAuCl_4$ aqueous solution were added sequentially to 50 mL of 0.025 M CTAB aqueous solution, followed by the injection of 0.3 mL of 0.1 M AA aqueous solution. Then, 0.8 mL of the as-prepared Au seed solution were quickly injected. After gently shaking, the growth solution was kept in a 30 ˚C water bath overnight. The as-synthesized Au NRs were separated and concentrated *via* centrifugation. The supernatant was carefully removed, and the Au NRs were concentrated to 0.2 mL for further use.

3.2.4 Au NRs with the longitudinal extinction band at 805 nm

In the growth solution, 0.5 mL of 10 mM $AgNO_3$ aqueous solution and 2.5 mL of 10 mM $HAuCl_4$ aqueous solution were added sequentially to 50 mL of 0.1 M CTAB aqueous solution, followed by the injection of 0.3 mL of 0.1 M AA aqueous solution. Then, 0.8 mL of the as-prepared Au seed solution were quickly injected. After gently shaking, the growth solution was kept in a 30 ˚C water bath overnight. The as-synthesized Au NRs were separated and concentrated *via* centrifugation. The supernatant was carefully removed, and the Au NRs were concentrated to 0.2 mL for further use.

3.2.5 Au NRs with the longitudinal extinction band at 1032 nm

In the growth solution, 0.6 mL of 12 mM $AgNO_3$ aqueous solution and 2 mL of 10 mM $HAuCl_4$ aqueous solution were added sequentially to 40 mL of 0.1 M CTAB aqueous solution. 3.2 mL of 1 M HCl solution were added to adjust the pH of the growth solution. Then, 0.32 mL of 0.1 M AA aqueous solution were added. Following, 0.8 mL of the as-prepared Au seed solution were quickly injected. After gently shaking, the growth solution was kept in a 30 ˚C water bath overnight. The as-synthesized Au NRs were separated and concentrated *via* centrifugation. The supernatant was carefully removed, and the Au NRs were concentrated to 0.2 mL for further use.

3.2.6 Polymer modification

The concentrated Au NRs were added dropwise into 10 mL of THF containing 4 mg of PS-SH. The solution was sonicated for 30 minutes and incubated overnight at room temperature. Then the PS-modified Au NRs were washed with THF for 6 cycles and re-dispersed in 4 mL of DMF. 1mL of the DMF solution, containing the PS- modified Au NRs, was added dropwise into 9 mL of H_2O containing, 1 mL of 0.2 M CTAB, to redisperse the PS- modified Au NRs into an aqueous solution. The concentration of the PS-modified Au NRs was further adjusted to make the extinction of the longitudinal LSPR band equal to 1. The aqueous solution was kept at room temperature for Pd layer coating.

3.2.7 Synthesis of polymer-tethered AuPd coaxial templates

PS-tethered AuPd coaxial templates were synthesized as follows. 1.6 mL of 10 mM H_2PdCl_4 were mixed with 20 mL of the PS-tethered Au NR solution, followed by

adding 0.8 mL of 0.1 M AA aqueous solution. After gentle shaking, the reaction was kept in a 30 ˚C water bath for more than 5 hours. The as-prepared PS-tethered AuPd coaxial templates were separated *via* centrifugation and washed twice with water at 14,000 rpm for 15 min. During the washing steps, BDAC was added to avoid template aggregation. The supernatants must be completely removed in order to decrease the CTAB residue in the solution. Then, the PS-tethered AuPd coaxial templates were redispersed in 2 mL of water before further use.

3.2.8 Ultrathin Pt NT synthesis via deposition of Pt on the AuPd coaxial templates

1 mL of the as-prepared AuPd coaxial templates was dispersed in 9 mL of water, containing 375 μL of 0.2 M BDAC. Then, 24 μL of 10 mM K_2PtCl_4 and 96 μL of KBr aqueous solution were added sequentially, followed by addition of 125 μL of 10 mM AA aqueous solution. To obtain Pt overgrowth layer with thickness of 1.5 nm, 2.1 nm, and 2.5 nm, different amounts of K_2PtCl_4 were added, respectively. After gentle mixing, the reaction was kept in an 80 ˚C water bath for 3 hours. After cooling down, the sample was washed with DMF and dispersed in 4 mL of 4mM $CuCl_2$ /DMF solution at 60 ˚C to etch away the AuPd coaxial templates. After 3 hours, the sample was separated by centrifuge, washed with DMF twice, and redispersed and kept in 1 mL water for the next step.

3.2.9 Synthesis of PtAu NTs

Typically, 0.1 mL of the as-prepared Pt NT aqueous solution was mixed with 0.9 mL of water containing 0.1 mL of 0.2 M CTAB, followed by adding 5 μL of 10 mM $AgNO_3$ and 5 μL of 0.1 M AA. The mixture was then kept at 60 ˚C for 1 hour, followed by the

injection of 120 μL of 1 M HCl and 12.5 μL of 10 mM $HAuCl_4$. The sample was then kept at 30 ˚C for more than 5 hours. After washing twice with water, the sample was redispersed in 1mL of water for further characterization.

3.2.10 Morphological, structural, and elemental characterizations

Transmission electron microscopy (TEM) images were taken using a JEOL LaB6 microscope operated at 200 kV. High-resolution TEM (HRTEM), high-angle annular dark-field scanning TEM (HAADF-STEM) and energy dispersive X-ray (EDX) analyses were performed using a JEOL 2100F microscope (JEOL, Tokyo, Japan) operated at 200 kV. Visible-NIR extinction measurements were performed using the PERKIN LAMBDA 40 UV–vis system.

3.2.11 Simulations

The finite-difference time-domain (FDTD) method was used for the three-dimensional modeling and simulation (Lumerical FDTD) of the electromagnetic response. The method with a pulse excitation allows for simultaneous broadband (400 to 1100 nm) full-wave simulation of a single object. Very fine mesh (1 nm) was used to ensure the simulation accuracy. The extinction, absorption and scattering spectra were calculated using the simulated fields. To compare the simulated results with experimental results, models (plane wave source) with different wavevector orientations and plane wave polarizations were simulated and the spectra were averaged based on excitation probability. The permittivity of gold is from reference[202].

3.3 Results and discussion

3.3.1 Synthesis strategy and characterization of the PtAu NTs

Figure 3.1a presents the scheme of a four-step synthetic strategy of hollow PtAu NTs, which includes the preferential deposition of a layer of Pd on PS-tethered Au NRs, the deposition of an ultrathin layer of Pt, the etching of PS-tethered AuPd coaxial templates, and the controllable deposition of Au on hollow Pt NTs. Briefly, the reaction started with PS-tethered Au NRs. Thiol-terminated PS was selectively modified to both ends of the Au NRs. With the protection of the collapsed PS at both ends of the Au NRs, the subsequent deposition of Pd selectively deposited to the side of Au NRs and formed a coaxial tubular Pd shell.

The layer of Pt deposition follows the method described in Section 2 Chapter 2. This method allows us to deposit an ultrathin layer of Pt on the surface of Pd at a relatively low temperature of 80°C, which can help to maintain the attachment of PS compared with other ultrathin Pt deposition methods performed at relatively high temperatures (≥100°C). After etching away the PS-tethered AuPd templates, ultrathin Pt NTs were reserved. Lastly, a layer of Au was deposited on the Pt NTs, regulated by Ag ion induced underpotential deposition (UPD).

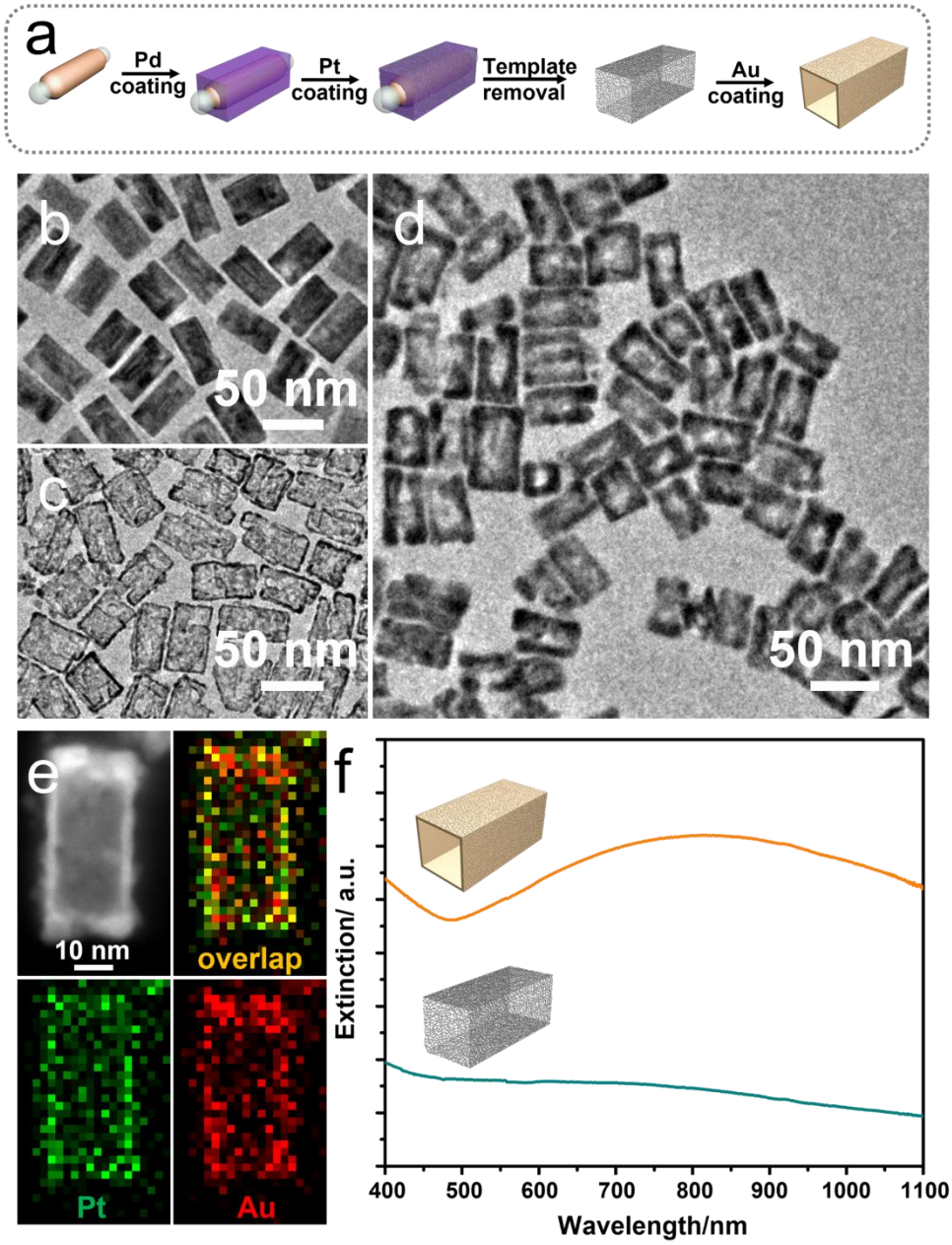

Figure 3.1 Morphology evolution of from PS-tethered Au NRs to PtAu NTs. (a) Schematic illustration of the four-step synthetic strategy of hollow PtAu NTs. (b-d) TEM images of (b) PS-tethered AuPd NRS, (c) Pt NTs, and (d) PtAu NTs. (e) HAADF-STEM image and the EDX mapping of an individual PtAu NT. (f) UV-vis-NIR spectra of Pt NTs and PtAu NTs.

The morphology evolution from PS-tethered Au NRs to PS-tethered AuPd NRs, Pt NTs, and finally PtAu NTs is presented in Figure 3.1 b-d, corresponding to Figure 3.1a. PS-tethered Au NRs with a length/width aspect ratio (LW-AR) of 4.4 (38.0 × 8.7 nm, length × width, Figure 3.3c and Table 3.1) served as templates at the initial step. The as-prepared PS-tethered Au NRs showed typical LSPR bands at 510 nm and 805 nm (Figure 3.3a). The PS-tethered AuPd NRs resulted in an increase of both length and diameter of the templates (49.6 × 27.0 nm, length × width) with a decreased LW-AR of 1.8 (Figure 3.1b and Table 3.3). Subsequently, Pt was deposited on the PS-tethered AuPd NRs, followed by the AuPd NR template removal. The resulting ultrathin Pt NTs (1.7 nm of averaged wall thickness) had an average outer diameter of 27.3 nm and an average length of 48.0 nm (Figure 3.1c and Table 3.5), whose dimensions shrunk slightly compared to those of the AuPd NR templates. No characteristic LSPR band was observed for Pt NTs (Figure 3.1f). After Au deposition, the acquired PtAu NTs inherited the structure of the Pt NT templates with a slight increase in its dimension (49.5 × 29.0 nm) (Figure 3.1d and Table 3.6). The averaged total thickness of the PtAu NTs was measured as 5.1 nm. The PtAu NTs exhibited high uniformity in both size and shape. EDX mapping clearly showed that Au deposited uniformly on the Pt NT template (Figure 3.1e). It is interesting to note that more Au was deposited inside Pt NTs as indicated the shrinkage of the inner diameter (I.D.) of the PtAu NTs (Table 3.6) compared to that of Pt NTs. The PtAu NTs exhibited a broad extinction peak with its central position located at 820 nm (Figure 3.1f).

3.3.2 Analysis of the Au deposition on the Pt NTs

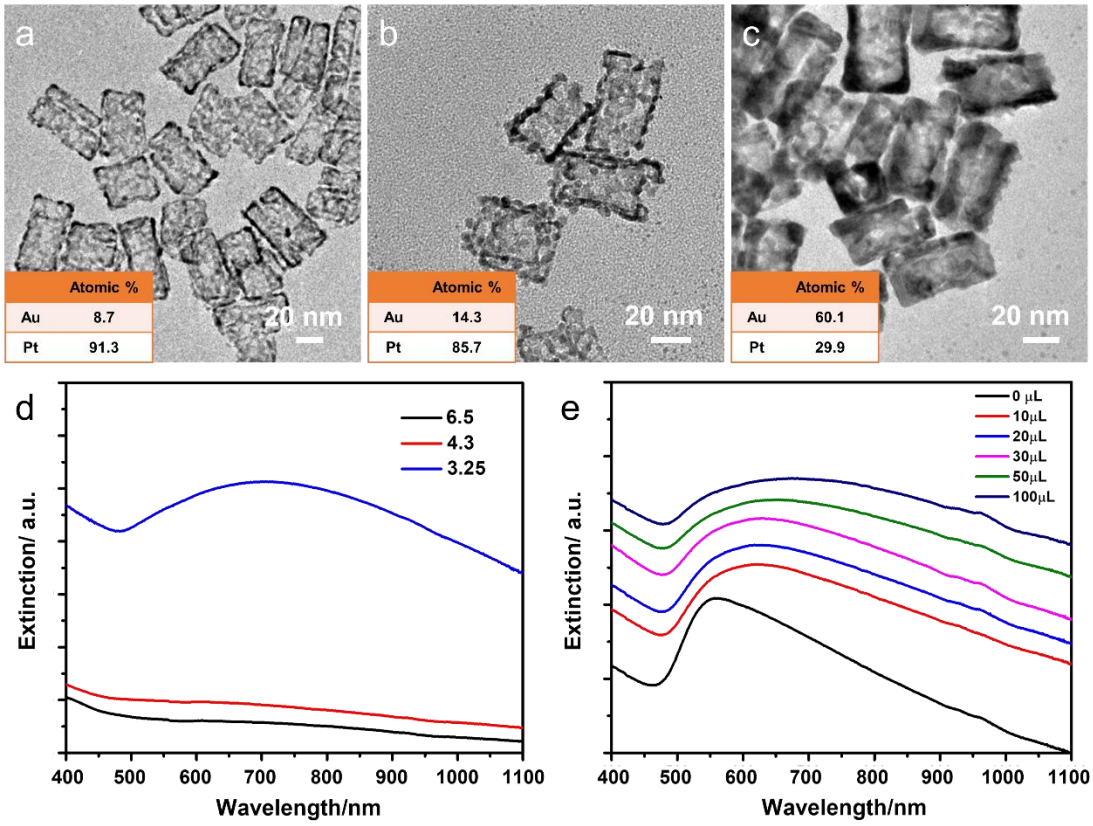

Figure 3.2 Controlling the morphology of PtAu NTs by the ratio between $[AuCl_4^-]/[Ag^+]$ and pH values. (a-c) TEM images of PtAu NTs synthesized at $[AuCl_4^-]/[Ag^+]$ ratio of 6.5, 4.3, and 3.25, respectively, the inset is the Au/Pt atomic percent from EDX. (d-e) UV-vis-NIR spectra of PtAu NTs with varied $[AuCl_4^-]/[Ag^+]$ ratios and volume of HCl.

The growth of Au on the Pt NT surface was controlled by the Ag intermediate layer. To investigate the assistance of the Ag^+ on the growth of Au, the ratio of $AuCl_4^-$ and Ag^+ ions was decreased by increasing the Ag^+ while keeping the amount of $AuCl_4^-$ fixed. As the ratio of Au to Ag decreased from 6.5 to 3.25, the coating of Au became

obvious (Figure 3.2a-c). EDX results revealed that the amount of Au increased in the PtAu NTs (Figure 3.2a-c insets). It should be noted as the ratio of Au^{3+}/Ag^{+} decreased from 6.5 to 4.3, the content of Au only slightly increased, in comparison to the obvious increase when the ratio further decreased to 3.25. We assumed that by increasing the Ag^{+}, a more complete Ag UPD layer was formed, which could have led to a more uniform Au deposition[203]. The Ag^{+} regulated Au deposition was also monitored by UV-vis spectra (Figure 3.2d). Although the intensity slightly increased when decreasing the ratio of Au^{3+}/Ag^{+} from 6.5 to 4.3, there was not an obvious change; however, a broad band presented at ~720nm when the ratio was further decreased to 3.25.

Additionally, during the UPD process, the deposition of Au and the corresponding LSPR band could be optimized by tuning the pH value of the reaction, as a lower pH value may make AA a weaker reducing agent[204], which modulates Au growth. The pH value was tuned by HCl. The LSPR band (Figure 3.2e) clearly showed, with the addition of HCl, a red-shift from 553 nm to ~700 nm along with obvious broadening of the peak.

3.3.3 Optical properties of PtAu NTs

The characteristics of the nanostructure's LSPR band, such as band shifting, absorbance magnitude damping, the resonance line width (full width at half maximum, FWHM), *etc*., are dependent on their geometry, dimensions, and components. As aforementioned, a hard template directed deposition is the key step to govern the synthesis of the PtAu NTs. Thus, we systematically tune the dimensions of the templates, including the LW-AR of the PS-tethered Au NRs, the thickness of the Pd

deposition layer, the thickness of the deposited Pt layer, and the thickness of Au layer, to investigate their influence on the PtAu NT LSPR.

3.3.3.1 Characterization of the Au NR template with different lengths

The length of the PS-tethered Au NRs plays the major role in controlling the length of the PtAu NTs. Au NRs of three different LW-ARs were synthesized *via* a modified seed mediated growth by adjusting the concentration of the Au seeds, CTAB, $AgNO_3$, and the pH of the growth solution, followed by PS modification to protect both ends of the as-synthesized Au NRs.

Figure 3.3b-d present the TEM images of the PS-tethered Au NRs. The average lengths and widths of the NRs were determined by measuring the dimensions of at least 100 NRs from their TEM images and summarized in Table 3.1. The LW-ARs of the Au NRs were calculated as 2.2 (denoted as short Au NRs, *S*-Au NRs), 4.4 (denoted as medium Au NRs, *M*-Au NRs) and 7.2 (denoted as long Au NRs, *L*-Au NRs), respectively. The corresponding extinction spectra show a clear red-shift of the longitudinal mode of the LSPR bands along with the increase of LW-ARs, while the LSPR band of the transverse mode remained almost unchanged (Figure 3.3a and Table 3.1).

Table 3.1 The dimension parameters and aspect ratios of the PS-tethered Au NRs

	Length/nm	Width/nm	LW-AR	Transverse/nm	Longitudinal/nm
S-Au NRs	25.6 ± 3.2	11.6 ± 1.7	2.2	518	634
M-Au NRs	38.0 ± 3.9	8.7 ± 1.3	4.4	510	805
L-AuNRs	64.7 ± 6.7	9.0 ± 1.3	7.2	506	1032

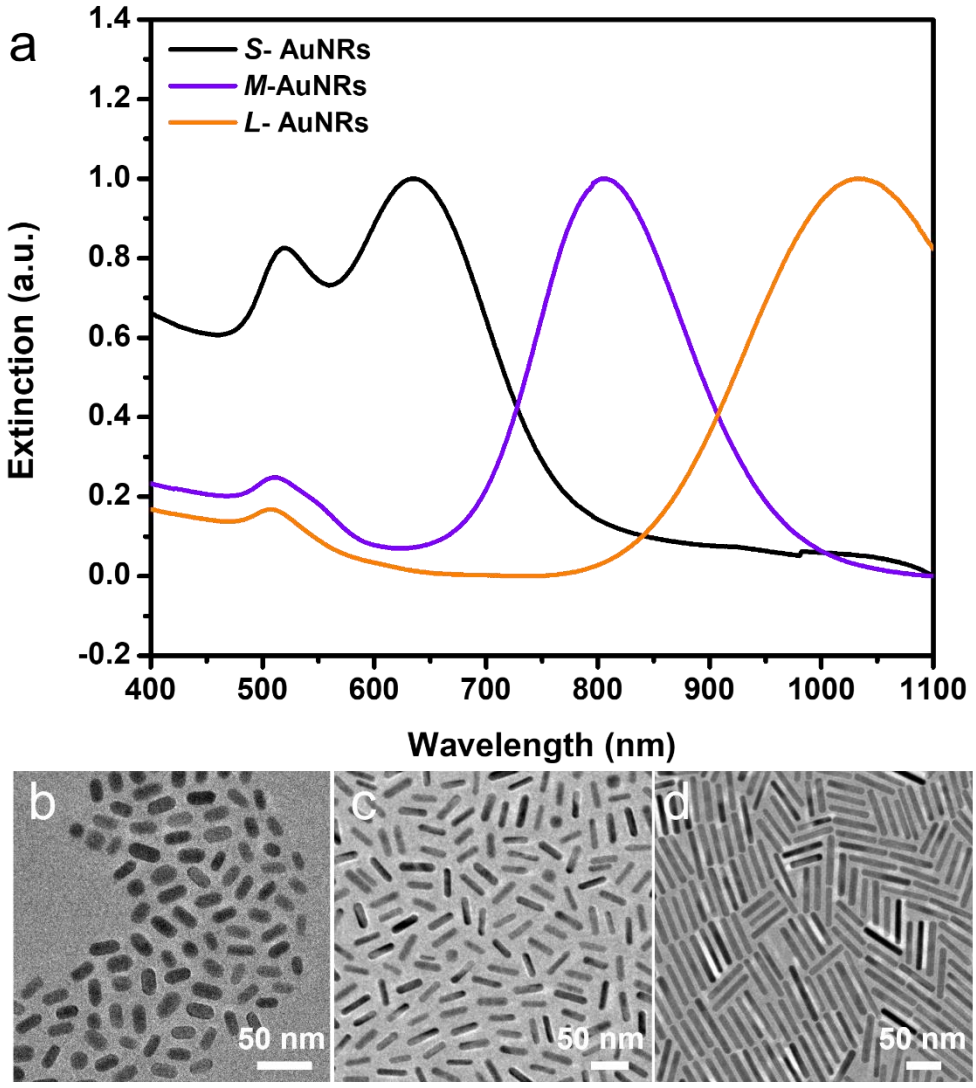

Figure 3.3 (a) The extinction spectra of the as-prepared PS-tethered Au NRs. (b-d) TEM images of the PS-tethered *S*-Au NRs, *M*-Au NRs and *L*-Au NRs.

3.3.3.2 Characterization of the PS-tethered AuPd coaxial NR templates

The width of the PtAu NTs is mainly tuned by the thickness of Pd deposition layer on the as-synthesized PS-tethered Au NRs. Figure 3.4-3.6 presents the length, width, and LW-ARs of the AuPd coaxial NR after Pd deposition on the *S*-Au NRs, *M*-Au NRs,

and *L*-Au NRs as a function of the feeding volume of $[PdCl_4^{2-}]$ ($V[PdCl_4^{2-}]$, 10 mM), respectively. When the $V[PdCl_4^{2-}]$ is low, the Pd preferentially deposited on the side of the PS-tethered AuNR templates, owing to the protection of the collapsed PS on both ends of the AuNRs. As the $V[PdCl_4^{2-}]$ increases, both length and thickness of the Pd deposition layer progressively increased. Consequently, the LW-AR of the PS-tethered Au-Pd coaxial NR decreased and reached a plateau of 0.9, 1.8, and 2.9 for the *S*-AuPd NRs, *M*-AuPd NRs, and *L*-AuPd NRs, respectively (Table 3.2-3.4). For each set of AuPd NRs grown from the corresponding Au NR template, although the LW-AR remained mostly constant as the $V[PdCl_4^{2-}]$ increased, the dimensions of the resulting PS-tethered AuPd NRs increased. Thus, this resulted in the increase in size of the Pt NTs and PtAu NTs.

Table 3.2 The relationship between $V[PdCl_4^{2-}]$ and the dimension parameters of *S*-AuPd NRs

$V[PdCl_4^{2-}]$/μL	200	400	800	1000	1200	1600
Length/nm	20.9±2.0	22.4±2.5	22.2±2.7	23.2±2.4	24.2±3.6	26.8±3.2
Width/nm	12.3±1.4	16.5±2.5	22.5±1.8	26.7±2.4	27.7±3.2	30.1±3.6
LW-AR	1.7±0.3	1.4±0.3	1.0±0.2	0.9±0.1	0.9±0.2	0.9±0.2

Table 3.3 The relationship between V[$PdCl_4^{2-}$] and the dimension parameters of *M*-AuPd NRs

V[$PdCl_4^{2-}$]/μL	200	400	800	1000	1200	1600
Length/nm	30.1±3.5	32.4±3.4	38.1±4.4	40.6±4.6	47.6±5.4	49.6±5.8
Width/nm	11.7±2.3	19.0±2.6	22.1±2.8	22.7±2.4	24.5±1.6	27.0±3.3
LW-AR	2.6±0.6	1.7±0.3	1.7±0.3	1.8±0.3	1.9±0.3	1.8±0.3

Table 3.4 The relationship between V[$PdCl_4^{2-}$] and the dimension parameters of *L*-AuPd NRs

V[$PdCl_4^{2-}$]/μL	200	400	600	800	1000	1200
Length/nm	63.1±7.5	65.8±9.3	71.8±7.6	73.9±7.0	77.7±9.0	76.3±8.1
Width/nm	15.2±1.7	18.5±2.0	21.7±2.4	22.6±1.9	25.0±2.5	25.7±2.6
LW-AR	4.2±0.7	3.6±0.6	3.3±0.5	3.3±0.4	3.1±0.5	3.0±0.4

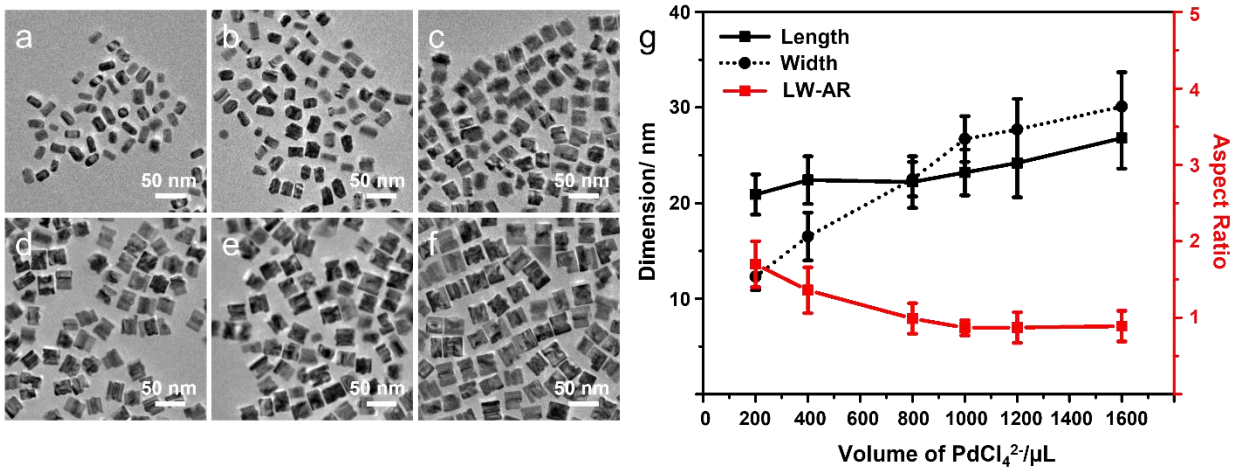

Figure 3.4 (a-f) TEM images *S*-AuPd NRs fabricated with different feeding volumes

of [$PdCl_4^{2-}$]: (a) 200, (b) 400, (c) 800, (d) 1000, (e) 1200, and (f) 1600 μL, respectively. (g) Dimensions and LW-AR values of corresponding *S*-AuPd NRs

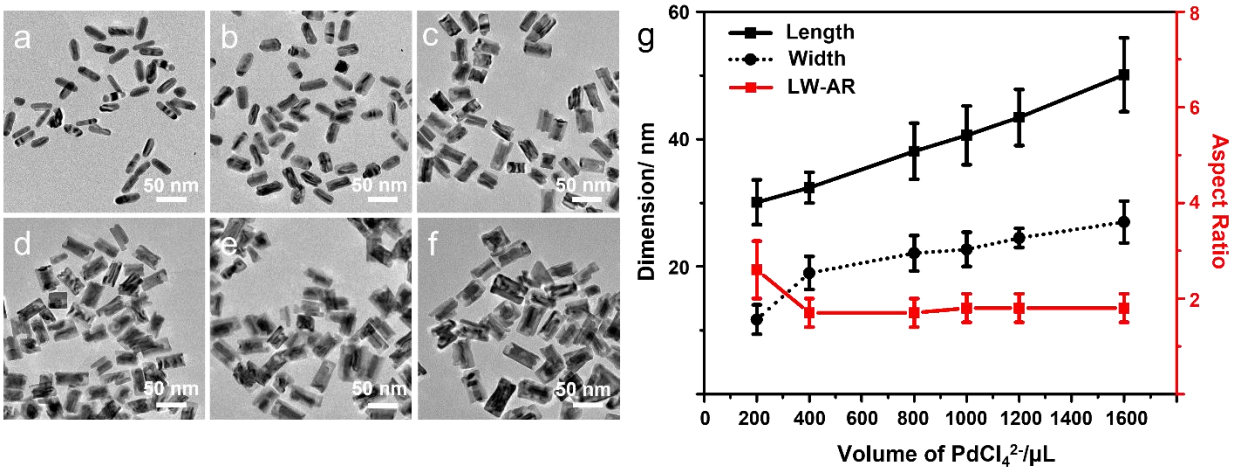

Figure 3.5 (a-f) TEM images *M*-AuPd NRs fabricated with different feeding volumes of [$PdCl_4^{2-}$]: (a) 200, (b) 400, (c) 800, (d) 1000, (e) 1200, and (f) 1600 μL, respectively. (g) Dimensions and LW-AR values of corresponding *M*-AuPd NRs

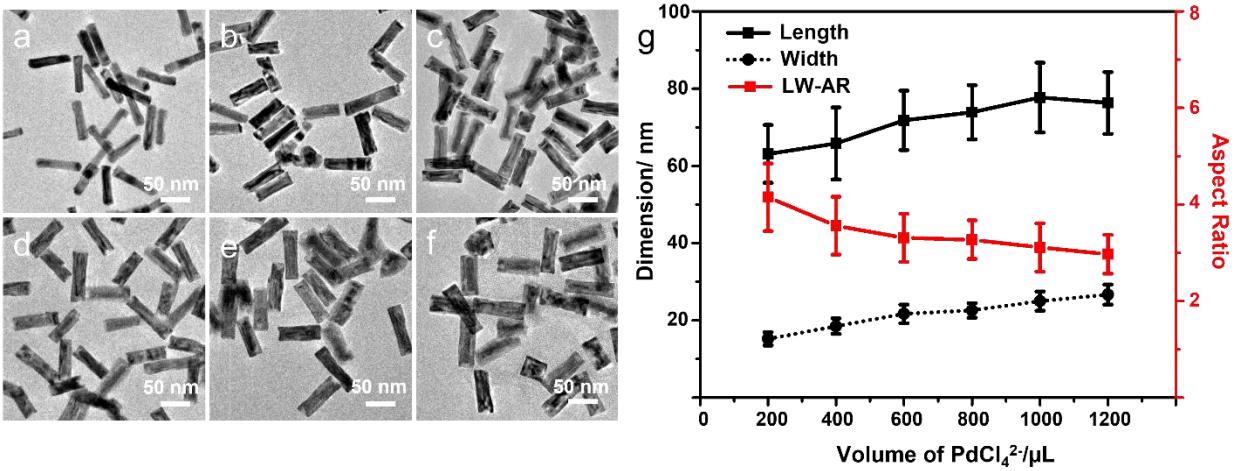

Figure 3.6 (a-f) TEM images *L*-AuPd NRs fabricated with different feeding volumes of [$PdCl_4^{2-}$]: (a) 200, (b) 400, (c) 600, (d) 800, (e) 1000, and (f) 1200 μL, respectively. (g) Dimensions and LW-AR values of corresponding *L*-AuPd NRs

3.3.3.3 Characterization of Pt NTs and PtAu NTs

Three series of Pt NTs and PtAu NTs synthesized were employing AuPd NRs of different lengths. These were: short nanotubes based off *S*-AuPd NRs (denoted as *ST*-Pt, *ST*-PtAu), medium nanotubes based off *M*-AuPd NRs (denoted as *MT*-Pt, *MT*-PtAu) and long nanotubes based off *L*-AuPd NRs (denoted as *LT*-Pt, *LT*-PtAu). A simplified schematic model was built to illustrate the dimension parameters of the NTs (Figure 3.8a). Figure 3.7 presents the TEM images of Pt NTs and the corresponding PtAu NTs with their dimension parameters presented in Table 3.5 and Table 3.6.

Table 3.5 Dimension parameters of the Pt NTs, with length (L), width (W), inner diameter (I.D.), and thickness (T) being extracted from TEM images.

Sample	L/nm	W/nm	I.D./nm	T/nm
ST_1-Pt	23.1±3.2	17.0±2.0	13.2±2.0	1.8±0.3
ST_2-Pt	23.5±3.1	23.5±3.0	19.8±2.9	1.7±0.2
ST_3-Pt	23.7±3.4	27.2±3.6	24.0±3.4	1.9±0.4
MT_1-Pt	34.9±3.5	17.2±2.4	12.8±2.3	1.8±0.3
MT_2-Pt	43.7±4.5	24.9±2.7	20.0±3.1	1.9±0.3
MT_3-Pt	48.0±4.0	27.3±2.5	23.1±2.3	1.7±0.3
LT_1-Pt	57.6±5.5	18.9±2.7	15.3±2.6	1.8±0.3
LT_2-Pt	62.5±6.2	24.2±2.8	19.6±3.2	1.9±0.2
LT_3-Pt	70.6±8.2	27.2±3.1	23.8±3.6	2.0±0.2

Table 3.6 Dimension parameters of the PtAu NTs, with L, W, I.D., and T being extracted from TEM images.

Composition	L/nm	W/nm	I.D./nm	T/nm
ST_1-PtAu	26.0±4.0	19.0±2.2	8.9±2.1	5.0±1.1
ST_2-PtAu	23.8±3.2	26.8±3.3	15.7±2.3	4.9±0.9
ST_3-PtAu	25.0±4.1	28.7±3.1	19.0±2.4	5.1±0.9
MT_1-PtAu	34.7±3.4	20.0±3.1	9.0±1.9	5.1±1.0
MT_2-PtAu	45.9±4.6	26.5±2.4	16.2±2.4	5.0±1.0
MT_3-PtAu	49.5±5.4	29.0±3.4	17.2±3.1	5.1±0.7
LT_1-PtAu	57.6±6.3	19.4±2.1	9.6±1.7	5.0±0.8
LT_2-PtAu	68.3±6.4	26.4±2.8	16.1±1.9	5.3±0.8
LT_3-PtAu	72.0±10.3	29.7±2.8	17.6±2.3	5.2±0.9

To facilitate further discussion on geometric and compositional dependent LSPR band position and band shifting, we adopted Pt NTs and PtAu NTs with controlled width, length, and thickness. The Pt thickness of all Pt NTs was precisely controlled around 1.8 nm (Table 3.5). For PtAu NTs, the total wall thickness (includes both Au layer and Pt layer) was controlled around 5.0 nm (Table 3.6). The NTs of different lengths labelled with the same subscripts indicate they shared same widths, inner diameters, and wall thicknesses, while their lengths varied.

As shown in Figure 3.7 a-r, all of the PtAu NTs inherited the structure of their corresponding Pt NT templates successfully with the hollow interior well-preserved. Figure 3.7 s, u and w present the normalized experimental extinction spectra of ST_n-,

MT_n- and LT_n-PtAu, respectively. To further investigate the LSPR of the PtAu NTs, we performed FDTD simulation to study the electromagnetic response of single PtAu NTs.

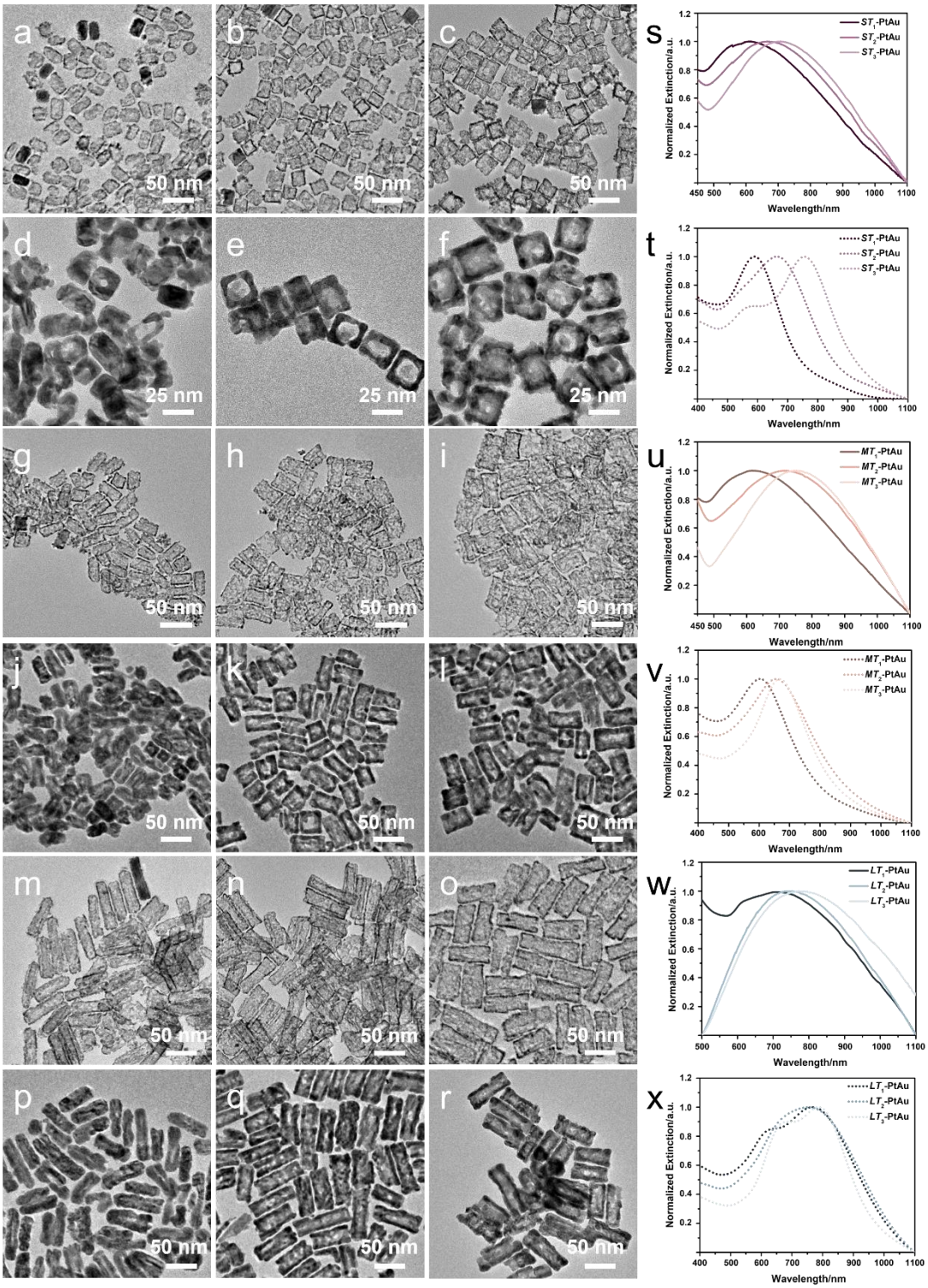

Figure 3.7 TEM images of (a-c) ST_n-Pt; (d-f) ST_n-PtAu; (g-i) MT_n-Pt; (j-l) MT_n-PtAu; (m-o) LT_n-Pt; (p-r) LT_n-PtAu. Experimental spectra and FDTD simulated spectra of ST_n-PtAu (s,t), MT_n-PtAu (u,v) and LT_n-PtAu (w, x), respectively.

Typically, PtAu NTs exhibited broad LSPR extinction bands in the UV-Vis region with the central peak positions shifting from 600 nm to 820 nm. Additionally, the corresponding simulated spectra exhibited similar LSPR band features; although, there are differences among the peak positions. We attributed the discrepancies between the experimental and simulated spectra to the polydispersity of the PtAu NTs and the porosity on the walls, as compared to the single PtAu NT, with smooth wall, used in the simulation.

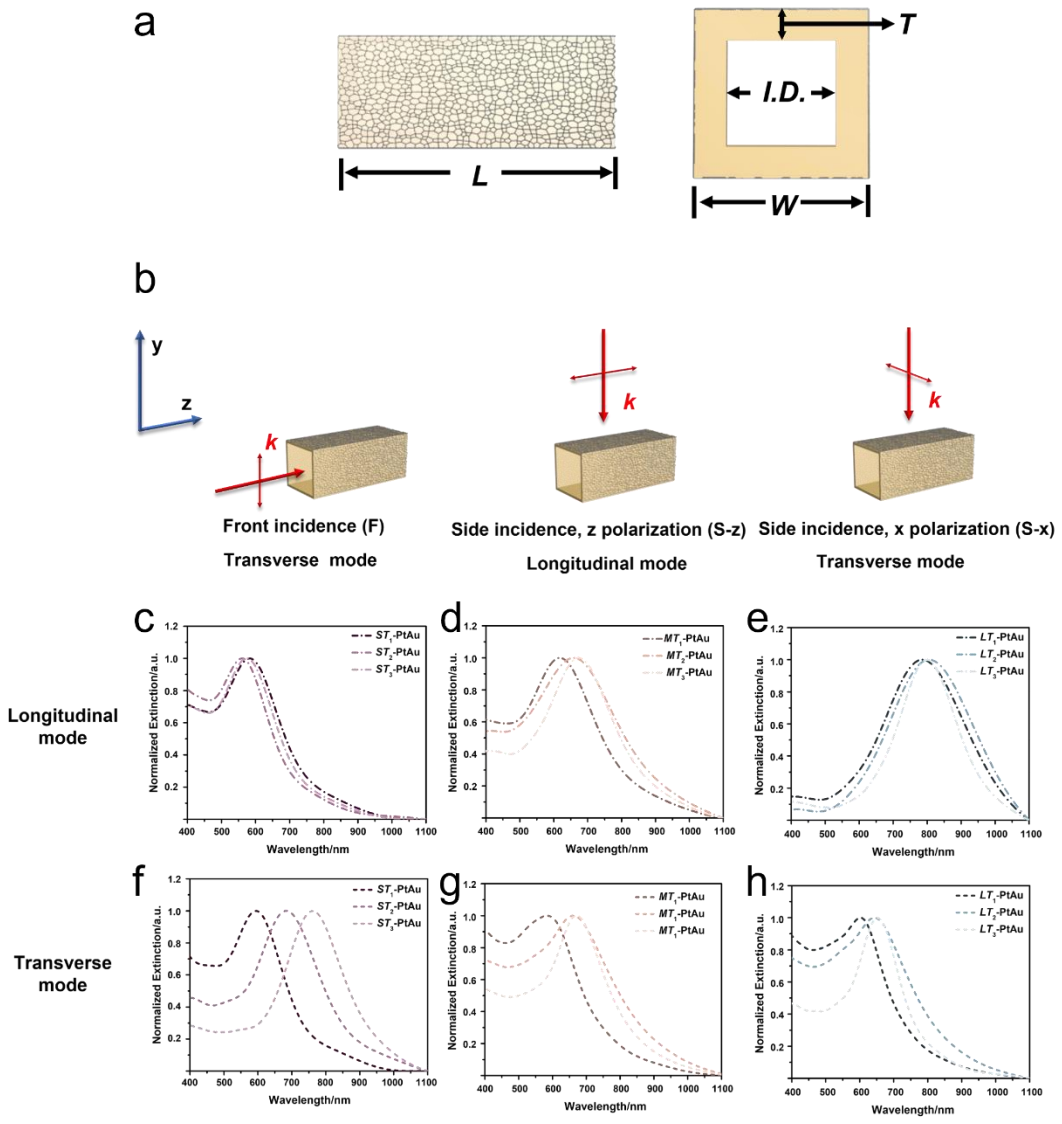

Figure 3.8 Schematic illustration of (a) geometric parameters of a single PtAu NT and (b) FDTD simulation: the excitation of the LSPR longitudinal and transverse modes with incident light of corresponding linear polarization and wavevector, respectively. (c-e) FDTD simulated L-Ext LSPR spectra of ST_n-PtAu, MT_n-PtAu and LT_n-PtAu and (f-h) FDTD simulated T-Ext LSPR spectra of ST_n-PtAu, MT_n-PtAu and LT_n-PtAu.

3.3.3.4 LSPR analysis of PtAu NTs

For isotropic hollow nanostructures, e.g., hollow Au nanoshells (NSs) and hollow Au-Ag nanocages (NCs), the LSPR band position has a close relationship with the ratio between the shell thickness and the outer diameter. However, for anisotropic tubular structures, due to the geometric differences on the longitudinal and transverse direction of the PtAu NTs, we broke the resonance by separating the LSPR transverse extinction mode (T-Ext mode) from the longitudinal extinction mode (L-Ext mode). We then studied the LSPR band shifting dependence on the geometric parameters along the corresponding direction (Figure 3.8b), similar to the LSPR study of anisotropic Au NRs. Thus, we define two ARs along the longitudinal and transverse direction, respectively:

$$LT - AR = \frac{Length}{Total\ wall\ thickness\ of\ PtAu\ NTs} \quad (1)$$

$$WT - AR = \frac{Width}{Total\ wall\ thickness\ of\ PtAu\ NTs} \quad (2)$$

The LW-AR of the PtAu NTs were defined the same as that of for Au NRs and AuPd NRs templates.

$$LW - AR = \frac{Length\ of\ PtAu\ NTs}{Width\ of\ PtAu\ NTs} \quad (3)$$

The FDTD simulated spectra of the longitudinal mode and transverse mode of the PtAu NTs are presented in Figure 3.8 c-h. The calculated LT-AR and WT-AR values (based off Table 3.6) together with LSPR extinction peak values along the longitudinal ($\lambda_{L\text{-}Ext}$)

and transverse direction ($\lambda_{T\text{-}Ext}$) extracted from Figure 3.8 c-h are presented in Table 3.7.

Table 3.7 Calculated LT-AR, WT-AR and LW-AR of ST_n-PtAu, MT_n-PtAu and LT_n-PtAu based off the dimension parameters listed in Table 3.6 with $\lambda_{L\text{-}Ext}$ and $\lambda_{T\text{-}Ext}$ collected from Figure 3.8 c-h.

Sample	LT-AR	WT-AR	LW-AR	$\lambda_{L\text{-}Ext}$/nm	$\lambda_{T\text{-}Ext}$/nm
ST_1-PtAu	5.2	3.8	1.4	583.0	595.1
ST_2-PtAu	4.9	5.5	0.9	559.0	682.7
ST_3-PtAu	4.8	5.6	0.8	572.5	760.9
MT_1-PtAu	6.8	3.9	1.7	617.6	583.4
MT_2-PtAu	9.2	5.3	1.7	659.4	652.0
MT_3-PtAu	9.8	5.7	1.7	671.3	664.1
LT_1-PtAu	11.6	3.9	3.0	786.0	601.9
LT_2-PtAu	13	5.0	2.6	806.6	644.1
LT_3-PtAu	13.8	5.7	2.4	799.0	653.2

At a fixed PtAu wall thickness, the extinction band of the L-Ext mode red-shifted by increasing the LT-AR, as did the T-Ext mode when increasing the WT-AR (Figure 3.9a and 3.9b). However, for ST_n-PtAu, the red-shift of the T-Ext mode, along with the increase of the WT-AR, is much greater than those of MT_n-PtAu and LT_n-PtAu (Figure 3.9b). It is also worth noting that although the WT-AR increased, the LW-AR of the *ST*-PtAu decreased from 1.4 to 0.8. Geometrically, the *ST*-PtAu, with a smaller LW-

AR, had more exposed interior space to the environment, similar to a nanoring structure. Therefore, such LSPR modes in previous literature can also be referred to as in-plane and out-of-plane modes, if we further reduce the length of the PtAu NTs.

In the meantime, there is no clear consistent trend between the LW-AR and L-Ext mode or LW-AR and T-Ext mode (Figure 3.9c and 3.9d). Consequently, it is concluded that the PtAu NTs exhibits typical LSPR characters of the hollow structures.

Nevertheless, we separated the longitudinal mode from the transverse mode and investigated their LSPR dependence on the LT-AR and WT-AR for discussion simplicity only. The dependence between the longitudinal mode and the transverse mode cannot be ignored and needs further comprehensive study.

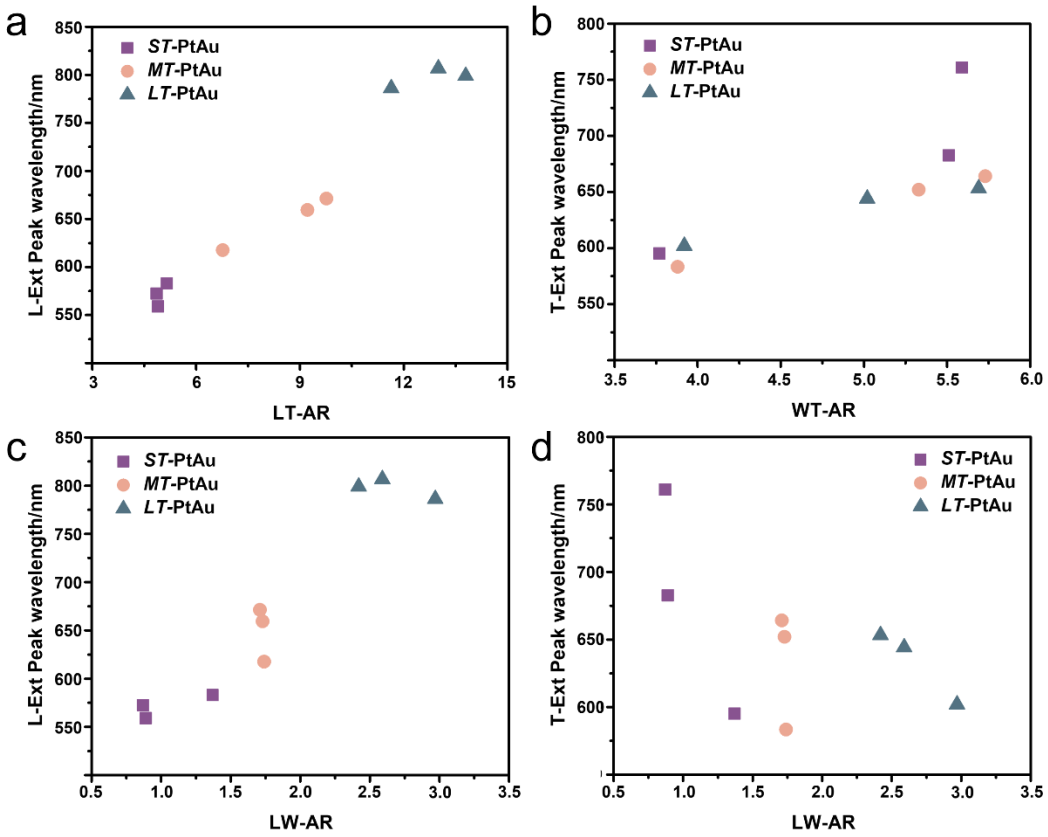

Figure 3.9 Dependence of (a) L-Ext peak wavelength on the LT-AR, (b) T-Ext peak wavelength on the WT-AR, (c) L-Ext peak wavelength on the LW-AR and (d) T-Ext peak wavelength on the LW-AR of ST_n-PtAu, MT_n-PtAu and LT_n-PtAu, respectively.

3.3.3.5 Au thickness influence on LSPR of PtAu NTs

We further analyzed the influence of Au thickness on the LSPR band shifting. Here, *MT*-Pt, with a Pt thickness of 1.7 nm, was employed as the templates. We precisely controlled the amount of [$AuCl_4^-$] added in the reaction to increase the thickness of the Au deposition layer, which increased from 2.4±0.7 nm to 7.2±1.1 nm (Figure 3.10 a-c and Table 3.8). It is worth noting that as the thickness of Au increased, the width (outer diameter) of the *MT*-$Pt_{(x)}Au_{(y)}$ (subscripts x and y represent the thickness of Pt and Au, respectively) only slightly increased, while the inner diameter shrunk significantly (Table 3.8), indicating more Au deposited on the interior surface of the *MT*-Pt than on the exterior surface.

For *MT*-$Pt_{(1.7)}Au_{(2.4)}$, a broad extinction band, with a central position red-shifted to the range of 700-800 nm with a slight intensity increase, was observed as compared to that of the *MT*-$Pt_{(1.7)}$ templates (refer to Figure 3.1h). Further increasing the Au thickness led to an obvious increase in LSPR band intensity, blue-shifting of the central band position, and a decrease of the FWHM (Figure 3.10d). Meanwhile, the FDTD simulated spectra matched well with the experimental spectra (Figure 3.10e). The dependence of the LT-AR on the L-Ext and WT-AR on the T-Ext peak wavelength are presented in Figure 3.10f and Table 3.9, respectively. As the thickness of Au increased, the T-Ext mode blue-shifted notably as compared to that of the L-Ext mode. According to the

plasmon hybridization model, proposed Prodan and Halas *et al.*[13,15], as the shell thickness increased, the reduced interaction between the sphere and cavity plasmon mode resulted in decreased splitting between the two hybrid plasmons of the NS, which resulted in blue-shifting of the LSPR peak.

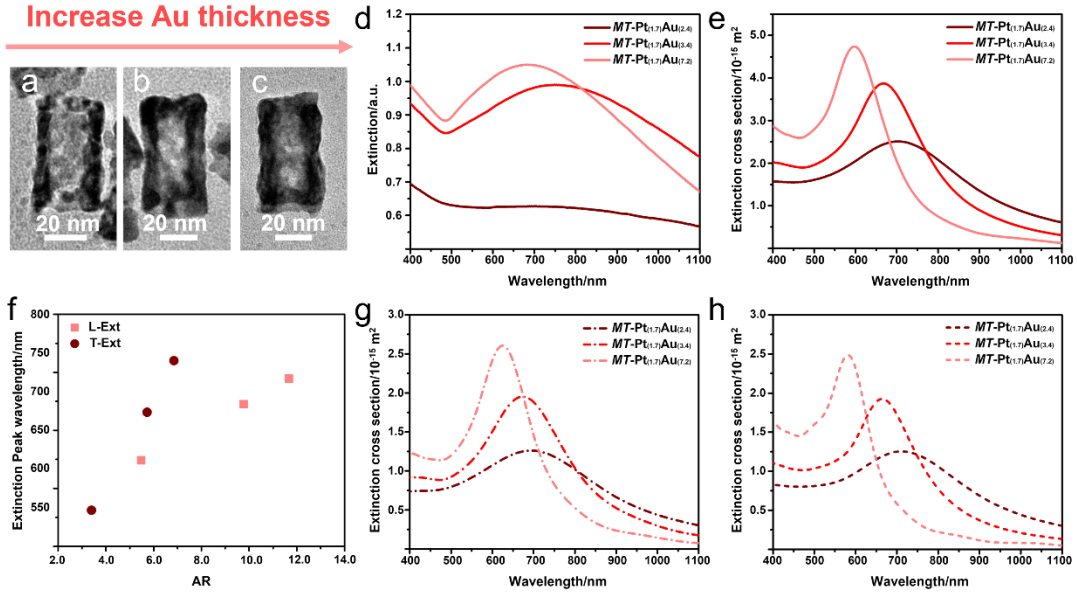

Figure 3.10 (a-c) TEM images of *MT*-$Pt_{(x)}Au_{(y)}$ with increased Au thickness. (d-e) Experimental and FDTD simulated spectra of *MT*-$Pt_{(x)}Au_{(y)}$, respectively. (f) Dependence of L-Ext peak wavelength on the LT-AR and T-Ext peak wavelength on the WT-AR. (g-h) FDTD simulated L-Ext and T-Ext LSPR spectra of *MT*-$Pt_{(x)}Au_{(y)}$.

Table 3.8 Dimension parameters of the *MT*-$Pt_{(x)}Au_{(y)}$, with L, W, I.D., and T extracted from TEM images. Au thickness was calculated by subtracting Pt thickness from the total thickness.

Sample	L/nm	W/nm	I.D./nm	T/nm	Au thickness/nm
MT-$Pt_{(1.7)}$	48.0±4.0	27.3±2.5	23.1±2.3	1.7±0.3	--
MT-$Pt_{(1.7)}Au_{(2.4)}$	48.1±5.2	28.2±3.0	20.0±3.0	4.1±0.6	2.4±0.7
MT-$Pt_{(1.7)}Au_{(3.4)}$	49.5±5.4	29.0±3.4	17.2±3.1	5.1±0.7	3.4±0.7
MT-$Pt_{(1.7)}Au_{(7.2)}$	48.9±5.5	30.3±3.0	10.3±2.3	8.9±1.1	7.2±1.1

Table 3.9 Calculated LT-AR, WT-AR, and LW-AR of *MT*-$Pt_{(x)}Au_{(y)}$ based off the dimension parameters listed in Table 3.8 with $\lambda_{L\text{-}Ext}$ and $\lambda_{T\text{-}Ext}$ collected from Figure 3.10 g-h.

Sample	LT-AR	WT-AR	LW-AR	$\lambda_{L\text{-}Ext}$/nm	$\lambda_{T\text{-}Ext}$/nm
MT-$Pt_{(1.7)}Au_{(2.4)}$	11.7	6.8	1.7	674.6	710.1
MT-$Pt_{(1.7)}Au_{(3.4)}$	9.8	5.7	1.7	672.6	665.6
MT-$Pt_{(1.7)}Au_{(7.2)}$	5.5	3.4	1.6	624.2	581.1

3.3.3.6 Pt thickness influence on LSPR of PtAu NTs

In various research, the LSPR peak broadening, in addition to peak position shift, was reported when Pt was coated on plasmonic Au nanostructures[205–207]. The FWHM broadening of the LSPR peak is mainly ascribed to the strong nonradiative damping that arises from the interband transition. The proximity of the *d* band to the Fermi level of Pt induces high probability of e^--h^+ excitation by small LSPR energies[208]. Thus, Pt

provides a damping channel of LSPR energy. Here we investigated the influence of the Pt thickness over the LSPR of the PtAu NTs.

MT-Pt with varied Pt thickness were employed as templates. The geometric parameters of all *MT*-$Pt_{(x)}$ and the corresponding *MT*-$Pt_{(x)}Au_{(y)}$ were listed in Table 3.10. The thickness of Au was controlled around 3.0 nm, while the thickness of Pt increased from 1.5 nm to 2.5 nm (Table 3.11). Figure 3.11a-f presents the TEM images of all *MT*-$Pt_{(x)}$ and the corresponding *MT*-$Pt_{(x)}Au_{(y)}$. It should be noted that the porous Pt NTs became intact along with the wall thickness increase (Figure 3.11a-c), as did the corresponding *MT*-$Pt_{(x)}Au_{(y)}$ (Figure 3.11d-f).

Table 3.10 Dimension parameters of *MT*-$Pt_{(x)}$ and *MT*-$Pt_{(x)}Au_{(y)}$, with L, W, I.D., and T extracted from TEM images.

Sample	L/nm	W/nm	I.D./nm	T/nm
MT-$Pt_{(1.5)}$	49.8±4.6	28.7±4.1	24.1±3.0	1.5±0.3
MT-$Pt_{(2.1)}$	48.1±3.6	29.0±2.5	23.2±1.6	2.1±0.3
MT-$Pt_{(2.5)}$	50.2±4.2	29.3±2.2	25.1±3.2	2.5±0.4
MT-$Pt_{(1.5)}Au_{(2.9)}$	51.3±2.6	29.9±3.1	22.0±1.9	4.5±0.8
MT-$Pt_{(2.1)}Au_{(3.0)}$	52.2±5.1	29.0±2.3	19.6±2.9	5.2±0.6
MT-$Pt_{(2.5)}Au_{(3.1)}$	52.5±4.9	29.9±1.6	21.2±2.2	5.6±0.6

Table 3.11 Calculated Pt thickness, Au thickness, and LT-AR and LW-AR from the *MT*-$Pt_{(x)}Au_{(y)}$ listed in Table 3.10.

	Pt thickness/nm	Au thickness/nm	WT-AR	LW-AR
MT-$Pt_{(1.5)}Au_{(2.9)}$	1.5±0.3	2.9±0.8	6.6	1.7
MT-$Pt_{(2.1)}Au_{(3.0)}$	2.1±0.3	3.0±0.7	5.6	1.8
MT-$Pt_{(2.5)}Au_{(3.1)}$	2.5±0.4	3.1±0.7	5.3	1.8

For *MT*-$Pt_{(1.5)}Au_{(2.9)}$, a broad extinction band with a central position at 850 nm was observed (Figure 3.11g). With the increase of Pt thickness, there was a clear blue-shift of the LSPR band to 760 nm. No obvious change of the LW-AR of the *MT*-$Pt_{(x)}Au_{(y)}$ was observed. Thus, we attributed the blue-shift of LSPR band to the decreased WT-AR[209,210], as indicated by the *plasmon hybridization* model discussed previously. Meanwhile, only a slight decrease of the FWHM was observed, as compared to the results when increasing the Au thickness (Figure 3.10d), indicating the strong LSPR broadening provided by Pt. Due to the difficulty of modelling porous structures, no FDTD simulation was performed here.

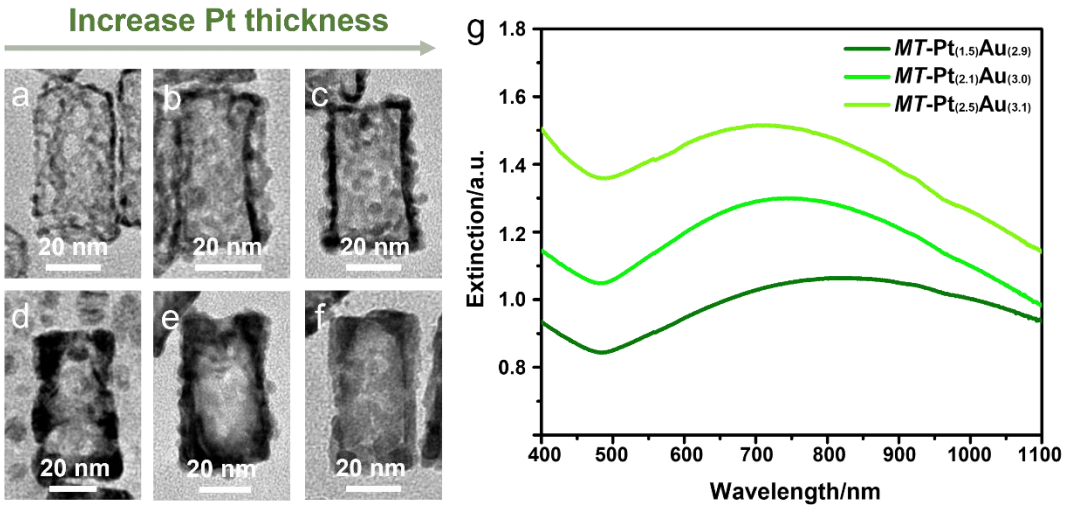

Figure 3.11 (a-c) TEM images of *MT*-$Pt_{(x)}$ with increased Pt thickness. (d-f) TEM images of *MT*-$Pt_{(x)}Au_{(y)}$ synthesized based off corresponding *MT*-$Pt_{(x)}$. (g) Experimental LSPR spectra of *MT*-$Pt_{(x)}Au_{(y)}$.

3.4 Conclusions

In summary, we proposed a template-directed multi-step synthesis to fabricate PtAu NTs. By tuning the dimensions of the templates, PtAu NTs with different dimensions have been synthesized. Based off the LSPR extinction spectra from both experiments and FDTD calculation, it is found that the LSPR of the PtAu NTs exhibited LSPR characteristics of both rodlike and hollow nanostructures. The LSPR band of the PtAu NTs can be tuned in the visible-NIR range by adjusting the dimension parameters, which may find applications in visible light driven photocatalysis.

Chapter 4: Tailoring the optical properties of PtAu nanotubes for high efficiency photocatalysis

Overview

In this chapter, the photocatalytic performance of PtAu NTs, under visible light irradiation, was investigated. *LT*-PtAu with a maximized superposition of transverse and longitudinal LSPR modes was predicted and demonstrated to exhibit the highest photoelectrochemical enhancement under different light irradiation conditions. The results successfully demonstrated the customizable design of photoelectrocatalysts. Manipulation over the LSPR band, through rational design of the plasmonic structure in the catalyst, can maximize the synergistic photoelectrocatalytic effect of the catalyst when combing the plasmonic entity and the catalytic entity.

A manuscript based on this chapter is in preparation.

4.1 Introduction

LSPR excitation has been demonstrated as an effective way to enhance electrocatalysis under visible light irradiation. Although plasmonic-semiconductor conjugates have demonstrated their advantages in converting light energy to drive catalytic reactions, the superior catalytic performance of transition metals cannot be ignored. It is of practical concern to develop electrocatalysts that combine the benefits of both plasmonic and catalytic metals to drive electrochemical reactions under visible-NIR light irradiation.

In this booming field, various multimetallic nanostructures have been reported with enhanced visible light driven photoelectrocatalytic performance, seeking optimized

compositional ratios, such as Pd_xAg NTs[63], 3D PdM nanosheet assemblies (M=Au, Ag, Cu)[211], AgPt edgeless nanocubes[66], Au@AgPt hollow urchin-like nanostructures[64], *etc*. However, the unique characteristic shape and size dependent LSPR of plasmonic nanostructures and its influence on the photoelectrocatalytic performance have been less considered when constructing the multimetallic photocatalyst systems[212]. Similar to the plasmonic-semiconductor conjugate systems, the effective energy transfer from the light absorber plasmonic entity to the catalytic entity transitional metal has been the key issue, in plasmonic-catalytic multicomponent nanostructure designs, to maximize the synergistic effect. Linic *et al.* proposed several design principles when designing multimetallic photocatalysts[52]. Multimetallic nanocatalysts with smaller sizes are favored as the fraction of absorption will dominate the total extinction. For the Au-Pt bimetallic system, the absorbed light energy is preferentially directed from Au to Pt at longer wavelengths. Thus, it remains challenging in rational construction of PtAu bimetallic nanostructure to satisfy the requirements of maximized LSPR absorption in visible-NIR region with minimized scattering, while fulfilling the traditional catalyst design demands, which includes, highly exposed active reaction sites, prolonged catalyst's stability, economically reduced Pt loading amount, *etc*.

In this chapter, PtAu NTs of three different lengths (*ST*-PtAu, *MT*-PtAu and *LT*-PtAu) and fixed widths were selected to investigate their photoelectrocatalytic performance. Based off the investigation of the geometric-dependence LSPR of PtAu NTs in Chapter 3, *LT*-PtAu with extended length were predicted to exhibit higher photoelectrocatalytic response under visible-NIR excitation, owing to the maximized superposition of transverse and longitudinal LSPR bands at longer wavelengths. The

photoelectrocatalytic performance of PtAu NTs with different lengths were investigated under 532 nm, 671 nm, and 808 nm laser irradiation. PtAu NTs of all selected lengths exhibited elevated electrocatalytic performance towards MOR under laser irradiation. Higher photoelectrochemical enhancement was observed when the PtAu NTs were irradiated with light of longer wavelengths. Additionally, *LT*-PtAu exhibited the highest photoelectrochemical enhancement under laser irradiation at all selected wavelengths. Moreover, under Xenon lamp irradiation, a simulation of broadband sunlight driven electrocatalysis, *LT*-PtAu exhibited superior photoelectrochemical enhancement compared to other catalysts.

It is also worth noting that *LT*-PtAu exhibited the highest intrinsic MOR activity under ambient light conditions. Together, with the superior photoelectrocalytic performance among the selected PtAu NTs, it is concluded *LT*-PtAu can be considered as a good photocatalyst that can enhance catalytic performance and effectively convert light energy to chemical energy. This work demonstrated a successful example of theoretical-directed rational design of photoelectrocatalysts. We expect this work could open a new design avenue for the future photoelectrocatalyst development.

4.2 Experiments

4.2.1 Materials

Gold (III) chloride trihydrate ($HAuCl_4.3H_2O$, 99.9 +%), silver nitrate ($AgNO_3$, 99+%), potassium tetrachloroplatinate (II) (K_2PtCl_4, 98+%), palladium (II) chloride ($PdCl_2$, 99+%), hydrochloric acid (HCl, 36.5%-38%), hexadecyltrimethylammonium bromide

(CTAB, 99%), benzyldimethyldodecylammonium chlorride (BDAC, 99.0%), sodium borohydride ($NaBH_4$, 99.99%), L-ascorbic acid (AA, 99%+), tetrahydrofuran (THF), dimethylformamide (DMF), and sodium hydroxide (NaOH) were purchased from Sigma-Aldrich.

HPLC water was used in all the experiments and was purchased from Sigma-Aldrich.

Hexadecyltrimethylammonium chloride (CTAC, >95%) was purchased from TCI.

Thiol-terminated polystyrene (PS-SH, Mn=12,000, Mw/Mn =1.09) was purchased from Polymer Source Inc.

Methanol (CH_3OH, Reagent Grade) was purchased from PHARMCO, sulfuric acid (H_2SO_4, 95-98%) were purchased from Alfa Aesar, and Nafion solution (5 wt.%) was purchased from Sigma-Aldrich. The commercial Pt/C was purchased from Fuel Cell Store (20% Pt on Vulcan XC-72R).

All the chemicals were used as received without further processing.

4.2.2 Synthesis of Pt NTs and PtAu NTs of different lengths

The template directed synthesis of Pt NTs and PtAu NTs followed the synthesis procedure as described in Section 3.2 Chapter 3. Specifically, to facilitate further discussion of LSPR properties and the influence on the light driven photoelectrocatalytic performance, the dimensional parameters of the *ST*-PtAu, *MT*-PtAu and *LT*-PtAu samples, including width and thickness of Pt and Au, were carefully controlled to be identical, while only the lengths of the PtAu NTs varied. All detailed dimensions of the Pt NTs and PtAu NTs are listed in Table 4.1.

4.2.3 Morphological, structural, and elemental characterizations

Transmission electron microscopy (TEM) images were taken using a JEOL LaB6 microscope operated at 200 kV. High-resolution TEM (HRTEM), high-angle annular dark-field scanning TEM (HAADF-STEM), selected area electron diffraction (SAED) and energy dispersive X-ray (EDX) analyses were performed using a JEOL 2100F microscope operated at 200 kV. Visible-NIR extinction measurements were performed using a Shimadzu UV-2501PC UV-Vis recording spectrophotometer. X-ray photoelectron spectra (XPS) were measured by an X-ray photoelectron spectrometer (Thermo Fisher ECSALAB Xi^+) equipped with an excitation source of Al Kα radiation (1486.6 eV). Inductively coupled plasma (ICP) data was determined by inductively coupled plasma atomic emission spectroscopy (ICP-AES) employing Shimadzu ICPE-9000 ICP-AES.

4.2.4 Electrochemical measurements

The electrocatalytic measurements were performed on a CHI 660A electrochemical workstation. A three-electrode system was used, where a glassy carbon electrode (GCE) (diameter 3mm) was used as the working electrode (WE), a Ag/AgCl (3M KCl) electrode was used as the reference electrode, and a graphite rod was used as the counter electrode. Catalytic inks were prepared as follows. First, the as-prepared PtAu NTs, of a specific length, were dispersed into a mixture of water (180 µL), ethanol (50 µL) and Nafion (20 µL). A total of 2 µL of the catalytic ink were then dropcast onto the surface of a clean WE. Subsequently, the modified WE was dried at room temperature for 1h. The methanol oxidation reaction (MOR) was performed in a freshly prepared N_2-saturated solution containing 1 M CH_3OH and 0.5 M NaOH. The scanning rate for the

MOR was set as 50 mV s^{-1}. Hollow Pt NTs and commercial Pt/C were both employed as the reference catalysts and their electrochemical catalytic performances were conducted using the same method.

4.2.5 Electrochemical measurements under light irradiation

The illumination sources were a 532 nm laser, a 671 nm laser, an 808 nm laser and a Xenon lamp, respectively. A representative experimental setup of the electrochemical measurement under laser irradiation using the 532 nm laser as the light source is presented in Figure 4.1a. The photoelectrochemical measurements were performed in a customized quartz reactor (30mm×30mm×30mm). Optical neutral filters (Thorlabs) were used to adjust the power intensity of the light source to 0.25 W/cm^2, 0.5W/cm^2, 0.75W/cm^2, and 1W/cm^2. All the illuminating power intensities from each light source were calibrated using Coherent FieldMate power meter. The power intensity was calculated following the equation:

$$Power\ intensity = \frac{Power}{Area\ of\ the\ light\ spot} \quad (1)$$

The Xenon lamp was exploited as the light source to evaluate the photoelectrochemical performance of the catalysts driven by broadband light irradiation. The experimental setup is presented in Figure 4.1b. Specifically, the electrochemical tests were measured in a customized cell equipped with a flat quartz window and a circulating cooling water system to minimize the heating of the electrolyte generated by the IR irradiation from the Xenon lamp.

All the electrochemical tests were performed at room temperature (21.6 °C), which was frequently monitored by a digital thermometer.

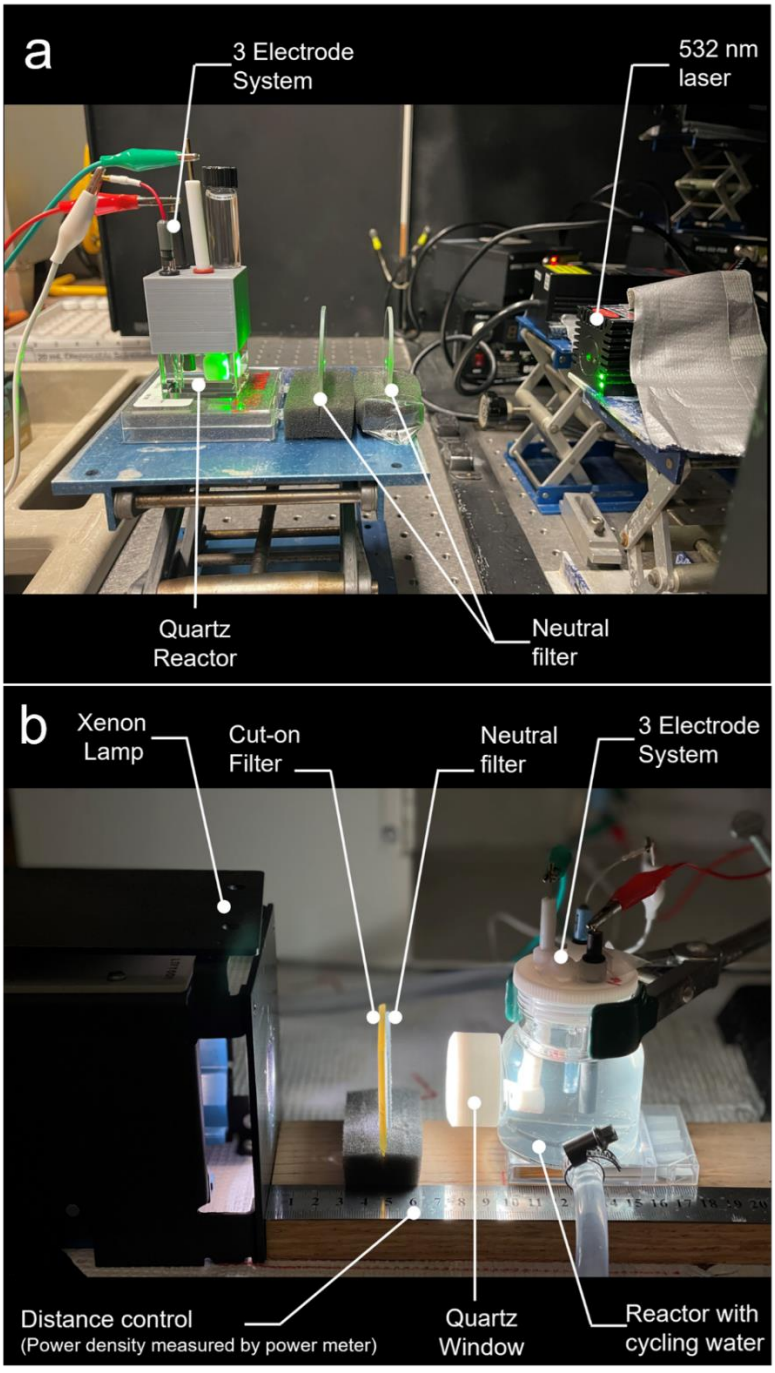

Figure 4.1. Representative photo images of the experimental setup of using (a) 532 nm laser and (b) Xenon lamp as the light irradiation sources for the electrochemical test.

4.3 Results and discussion

4.3.1 Characterization of PtAu NTs

PtAu NTs of different lengths were synthesized by adopting as-synthesized PS tethered *S*-AuPd NRs, *M*-AuPd NRs and *L*-AuPd NRs coated with the same Pd thickness as templates, respectively. The dimension parameters of the acquired Pt NTs and PtAu NTs are presented in Table 4.1 (the data was extracted from Table 3.5 and 3.6 in Chapter 3). The lengths of the *ST*-PtAu, *MT*-PtAu and *LT*-PtAu were measured as 25.0±4.1, 49.5±5.4, and 72.0±10.3 nm, respectively, while the widths of all PtAu NTs were almost identical (~27 nm). The wall thickness of all the Pt NTs was controlled between 1.7-1.9 nm, and the total wall thickness of the PtAu NTs was controlled between 5.0-5.2 nm.

Table 4.1 The dimensions of all the Pt NTs and PtAu NTs adopted in this chapter.

	Sample	Length/nm	Width/nm	I.D./nm	Thickness/nm
S-NTs	Pt NTs	23.7±3.4	27.2±3.6	24.0±3.4	1.9±0.4
	PtAu NTs	25.0±4.1	28.7±3.1	19.0±2.4	5.1±0.9
M-NTs	Pt NTs	48.0±4.0	27.3±2.5	23.1±2.3	1.7±0.3
	PtAu NTs	49.5±5.4	29.0±3.4	17.2±3.1	5.1±0.7
L-NTs	Pt NTs	70.6±8.2	27.2±3.1	23.8±3.6	2.0±0.2
	PtAu NTs	72.0±10.3	29.7±2.8	17.6±2.3	5.2±0.9

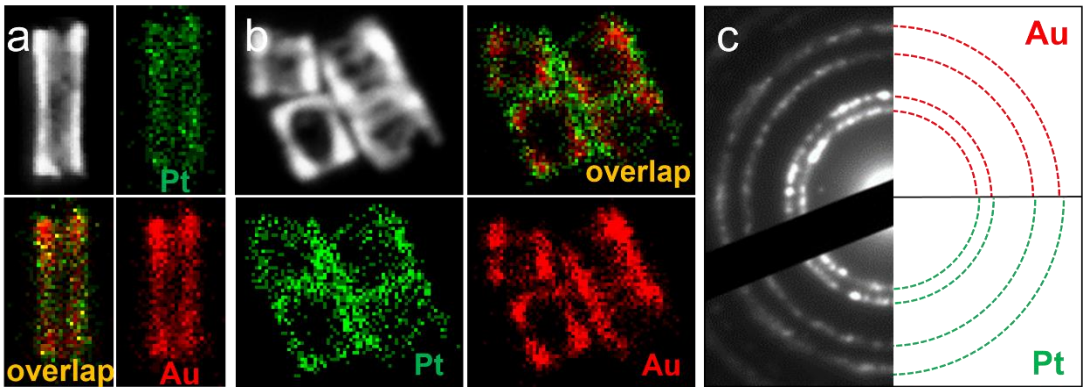

Figure 4.2 (a) HAADF-STEM image and the EDX mapping of an individual *LT*-PtAu. (b) HAADF-STEM image and the EDX mapping of an individual *ST*-PtAu. (c) The SAED pattern of *LT*-PtAu and schematic illustration of Au (red dash lines) and Pt (green dash lines).

Figure 4.2a and b present the EDX mapping images of the *LT*-PtAu and *ST*-PtAu, respectively. Similar to the *MT*-PtAu (Figure 3.1e), the results clearly showed that Au deposited uniformly on the Pt NT templates of the corresponding length. Taken *LT*-PtAu as an example, the selective area electron diffraction (SAED) image revealed the polycrystalline nature of PtAu NTs (Figure 4.2c). Further detailed analysis indicated that the diffraction rings can be indexed as fcc Au (red dash line) and fcc Pt (green dash line), although the two sets of rings almost overlapped with each other.

4.3.2 LSPR analysis of PtAu NTs with different lengths

The mass normalized vis-NIR spectra of the NTs are presented in Figure 4.3a. The PtAu NTs exhibited a broad LSPR band centered at 717 nm for the *ST*-PtAu, 720 nm for the *MT*-PtAu and 820 nm for the *LT*-PtAu, respectively. The calculated spectra

obtained from FDTD simulations (Figure 4.3b) are generally consistent with the experimental spectra.

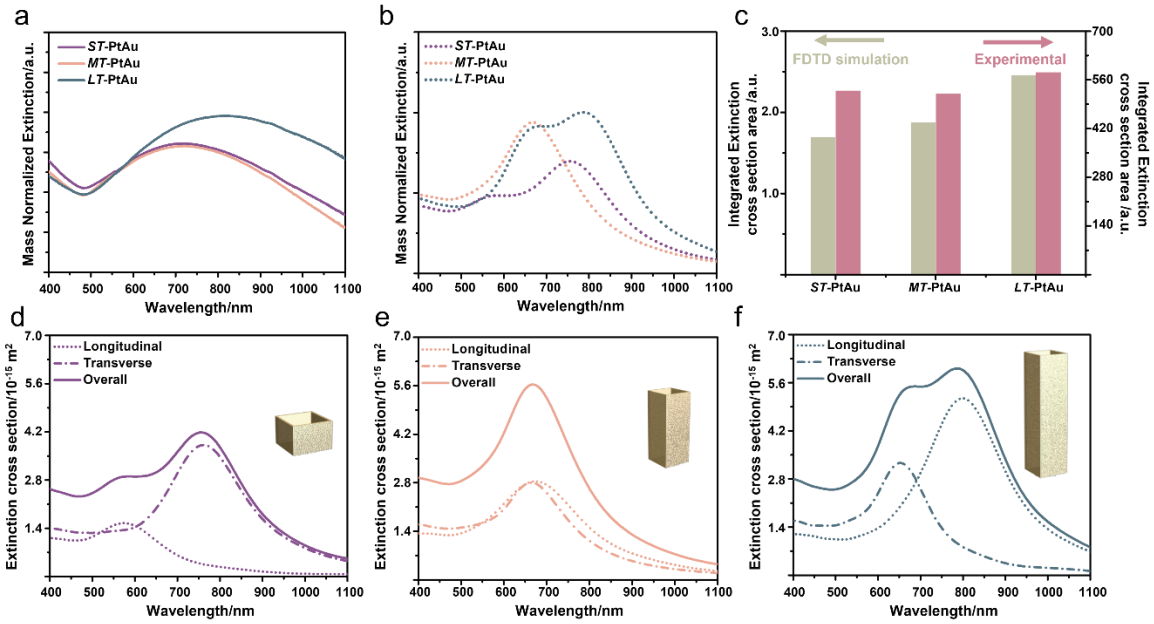

Figure 4.3 (a, b) mass normalized vis-NIR spectra of *ST*-PtAu, *MT*-PtAu, and *LT*-PtAu obtained from experimental results and FDTD simulations, respectively. (c) the comparison of the integrated extinction cross section area between the experimental spectra and the FDTD simulated spectra in the range of 400-1100 nm. (d-e) the separated longitudinal LSPR mode and transverse LSPR mode for the *ST*-PtAu, *MT*-PtAu, and *LT*-PtAu obtained from the FTDT simulation, respectively.

To estimate and compare the extinction of PtAu NTs of different lengths over the vis-NIR range, we integrated the extinction cross section in the vis-NIR region from 400 nm to 1100 nm. The extinction cross-section of a single nano-object at a specific wavelength is defined as the extinction power divided by the power density (power per unit area) of the incident beam. This is also the same for absorption or scattering cross-

section. The extinction cross-section is proportional to the extinction power as we use a constant incident power density. For a broadband spectrum, this means the extinction cross-section is proportional to the extinction power spectral density (power per unit wavelength). Integration over a range of extinction cross-section spectrum provides the "total extinction power" in the spectral range. The absolute value of the total extinction power is not meaningful since it depends on the absolute value of the excitation source power; however, this approach allows us to evaluate the difference of the total extinction, absorption, or scattering power among different nanoparticles with varied compositions and morphologies, based on the calculated cross-section spectra results. Figure 4.3c shows the integrated extinction cross section area (IECSA) of PtAu NTs of different lengths. *LT*-PtAu presented the highest IECSA in both the experimental spectrum and FDTD simulation, compared to the *ST*-PtAu and *MT*-PtAu. The extinction contribution from the longitudinal and transverse modes are presented in Figure 4.3d-f. The LSPR longitudinal extinction mode (L-Ext) of the PtAu NTs, red-shifts from 571 nm to 799 nm with increasing intensity as the NT length increases. Meanwhile, the transverse extinction mode (T-Ext), blue-shifts from 760 nm to 651 nm. Although the width of the PtAu NTs was kept constant, the increase in length led to a significant red-shift of the L-Ext mode and a moderate blue-shift of the T-Ext mode. Interesting, this is counterintuitive when we compare this to the LSPR of anisotropic Au NRs, where the T-Ext mode doesn't shift noticeably when the width of the Au NRs is fixed, and the L-Ext mode shifts significantly as the length is increased. Thus, we believe this unique reciprocal shifting of the L-Ext and T-Ext modes promotes a

broader extinction of the *LT*-PtAu in the visible-NIR range by the superposition of the L-Ext and T-Ext modes, compared to the *ST*-PtAu and *MT*-PtAu.

Furthermore, the FDTD results indicates that absorption is the dominant decay channel for PtAu NTs of different lengths (Figure 4.4), owing to their small dimensions. For *LT*-PtAu (Figure 4.4g-i), although the scattering along the longitudinal direction increases as the length of the PtAu NTs increases (Figure 4.4h), the absorption still dominates the light decay pathway.

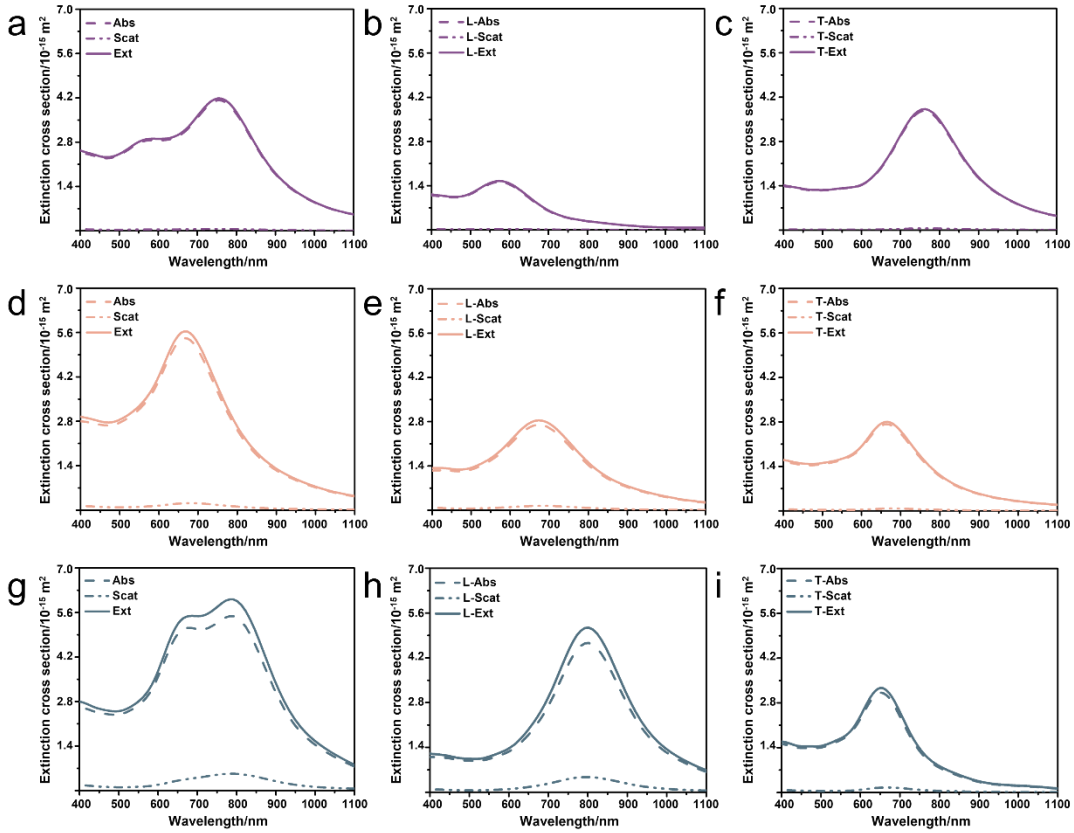

Figure 4.4 FDTD simulated fractional extinction, absorption, and scattering, along longitudinal direction, and transverse direction of (a-c) *ST*-PtAu, (d-f) *MT*-PtAu, and (g-i) *LT*-PtAu.

4.3.3 Surface structure identification of PtAu NTs by XPS

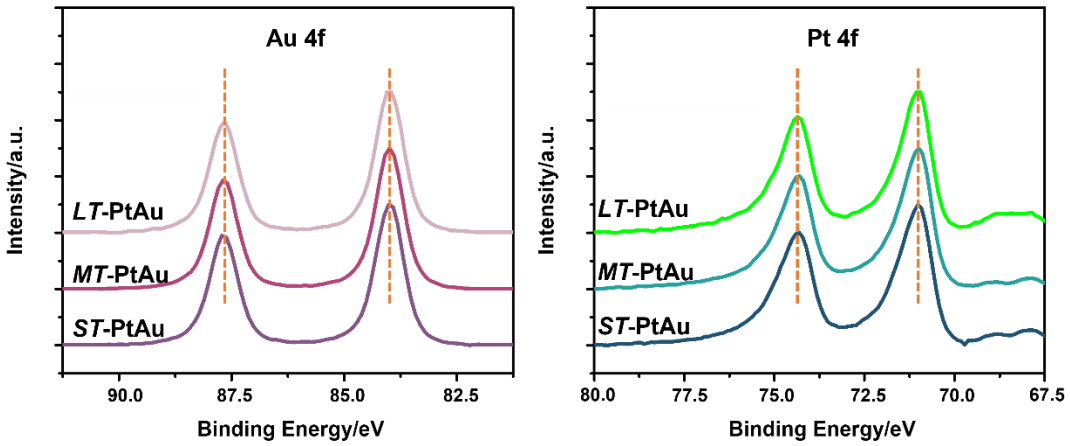

Figure 4.5 Comparison of the XPS spectra of (a) Au 4f and (b) Pt 4f for *ST*-PtAu, *MT*-PtAu and *LT*-PtAu, respectively.

XPS was utilized to investigate and compare the surface composition and valence state of Pt and Au for the PtAu NTs of different lengths. Figure 4.5 displays the high-resolution XPS spectra of Au 4f and Pt 4f. For *LT*-PtAu, the binding energies at 70.95eV and 74.35 eV correspond to Pt $4f_{7/2}$ and Pt $4f_{5/2}$, respectively, and 84.00 and 87.66 eV correspond to Au $4f_{7/2}$ and Au $4f_{5/2}$, respectively. Both Au and Pt exist in the metallic state. The binding energy differences (ΔE) between the Pt $4f_{7/2}$ and Au $4f_{7/2}$ of *LT*-PtAu are the same as the literature value[213], indicating that there is no significant electron transfer between Pt and Au. Meanwhile, no obvious peak shift of Au 4f and Pt 4f was observed for *ST*-PtAu and *MT*-PtAu (Figure 4.5), inferring that the valence states of Pt and Au for *ST*-PtAu and *MT*-PtAu were similar to that of *LT*-PtAu, as further confirmed by the similar calculated ΔE (Table 4.2).

Table 4.2 Binding energies of Pt 4f and Au 4f acquired from XPS spectra and the binding energy difference (ΔE) between Pt $4f_{7/2}$ and Au $4f_{7/2}$ for PtAu NTs of different lengths in comparison to the literature value[213].

	Binding Energy (eV)				
	Pt $4f_{7/2}$	Pt $4f_{5/2}$	Au $4f_{7/2}$	Au $4f_{5/2}$	ΔE
ST-PtAu	71.02	74.31	84.00	87.66	12.98
MT-PtAu	70.99	74.29	84.00	87.66	13.01
LT-PtAu	70.95	74.35	84.00	87.66	13.05
Lit Value	71.0	--	84.0	--	13.0

4.3.4 Au/Pt mass ratio and surface atomic ratio investigation

The mass ratios of Au/Pt for the *ST*-PtAu, *MT*-PtAu and *LT*-PtAu were examined by both EDX and ICP-AES. The Au/Pt ratio in all the PtAu NTs was measured as 1.8-1.9 (Table 4.3). The surface element distribution of Au and Pt was investigated by XPS.

Table 4.3 The mass ratio of Au/Pt ratio measured by EDX, ICP-AES and the surface atomic ratio of Au/Pt measured by XPS and CV.

	EDX	ICP-AES	XPS	CV
ST-PtAu	2.17	1.83	0.93	0.79±0.07
MT-PtAu	1.95	1.97	0.82	0.84±0.09
LT-PtAu	1.92	1.88	1.12	0.79±0.07

XPS and cyclic voltammetry (CV) were employed to quantitatively determine the surface atomic ratio between Pt and Au of the PtAu NTs of different lengths. The CV curves show two reduction peaks at 0.92 V and 0.43 V, corresponding to the oxygen desorption from Au and Pt when comparing with the reduction peak potentials of the bare Au electrode (0.96 V) and Pt NTs modified onto a GCE (0.46 V) (Figure 4.6a). This indicates that the surface of the PtAu NTs is composed of both Au and Pt instead of a complete coverage of Au on the Pt NT templates. The charges required to the electrochemically reduce the surface Au-O and Pt-O are 400 and 440 $\mu C \cdot cm^{-2}$, respectively[214]. The calculated surface area ratios of Au/Pt of different lengths are listed in Table 4.3.

The bulk mass ratios of PtAu NTs of different lengths were reported as ~2, while the surface atomic ratios between Au and Pt, measured by the surface sensitive techniques XPS and CV were reported as 0.8 (Figure 4.6b). The difference between the bulk Au/Pt mass ratio and the surface Au/Pt atomic ratio further confirmed that the exterior of the PtAu NTs were composed of Pt and Au with more Au deposited on interior surface of the NTs.

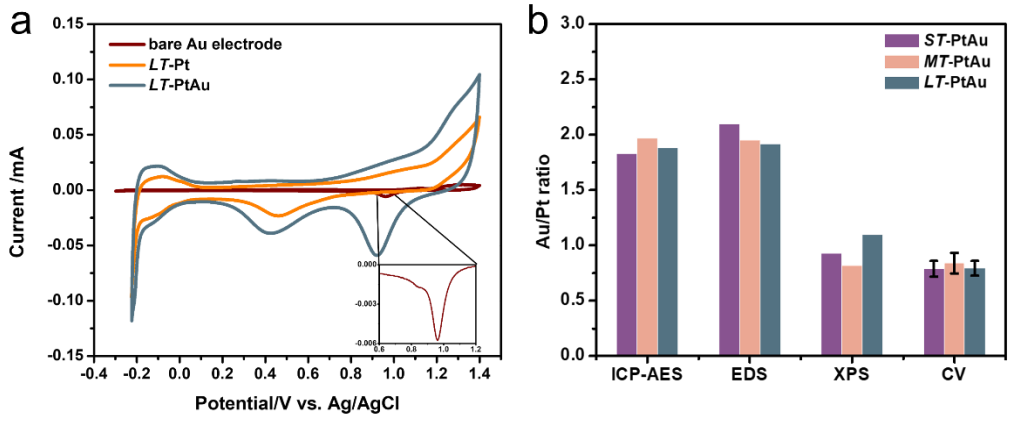

Figure 4.6 (a) Cyclic voltammograms of the bare Au electrode, Pt NTs modified on a GCE and PtAu NTs modified on a GCE in a 0.5 M H_2SO_4 solution (purged with N_2) with a scanning rate of 50 mV/s. (b) Au/Pt mass ratio and surface atomic ratio measured by ICP-AES, EDX, XPS, and CV.

4.3.5 MOR catalytic performance of Pt NTs, PtAu NTs, and commercial Pt/C

The electrocatalytic activities of Pt NTs and PtAu NTs toward MOR under an ambient light environment (referred to as the dark condition, in comparison to the MOR electrochemical reaction carried out under light irradiation) were measured and compared by CV scans in 0.5 M NaOH solution with 1 M CH_3OH. Figure 4.7a presents the CV scans of Pt NTs of different lengths and the commercial 20% Pt/C catalyst. The electrochemical surface area (ECSA) of Pt was employed to estimate the specific activities of the catalysts. The ECSA was calculated *via* integrating the hydrogen adsorption charge obtained by CV scans with a scanning rate of 50 mV s^{-1} in an N_2-saturated 0.5 M H_2SO_4 solution at room temperature.

All samples tested exhibited characteristic MOR catalytic behavior with oxidation peaks in both forward and backward scans. For all Pt NTs, the forward scans showed MOR peak oxidation potentials between -0.18 to -0.19 V *vs.* Ag/AgCl. The specific activities of the *ST*-Pt, *MT*-Pt, and *LT*-Pt were measured to be 2.03, 2.54, and 2.80 mA cm^{-2}, respectively (Figure 4.7b). By contrast, the commercial Pt/C showed a lower specific peak current density of 1.95 mA cm^{-2} at a higher peak potential (-0.12V *vs.* Ag/AgCl).

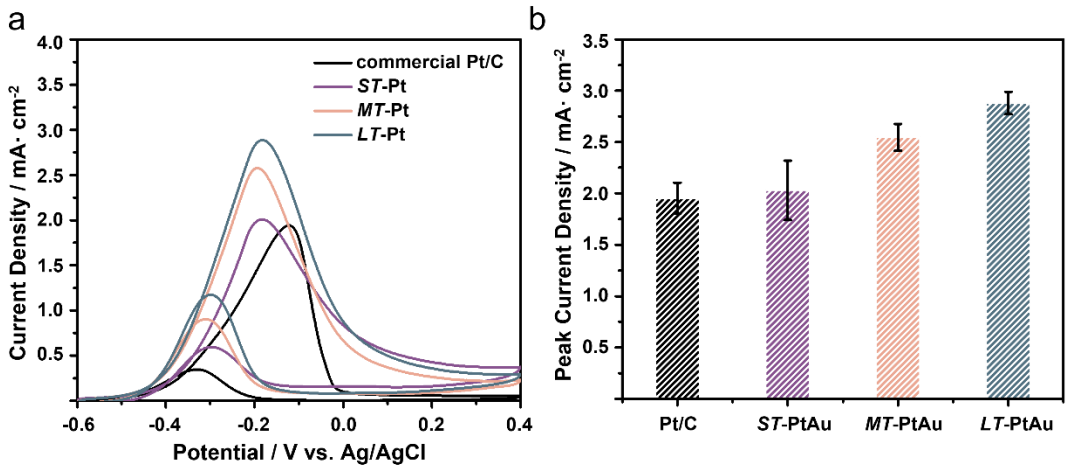

Figure 4.7 MOR performance of Pt NTs and commercial Pt/C. (a) CVs of Pt NTs of different lengths and the commercial Pt/C in an aqueous solution of 1 M CH_3OH and 0.5 M NaOH. The CV scanning rate was 50mV s^{-1}. (b) The corresponding histogram of specific activities.

After Au deposition, the resulting PtAu NTs showed enhanced MOR activities compared with their corresponding Pt NT templates. The *ST*-PtAu, *MT*-PtAu, and *LT*-PtAu exhibited specific activities of 9.38, 11.53, and 14.06 mA cm^{-2}, respectively (Figure 4.8a). The specific activities of the *ST*-PtAu, *MT*-PtAu and *LT*-PtAu are 4.60, 4.54, and 4.89 times higher than their corresponding Pt NTs templates, respectively (Figure 4.8b). Additionally, the I_f/I_b (ratio between the peak current in the forward and backward scan) dramatically decreased for PtAu NTs compared to their corresponding Pt NTs of the same length. A higher I_f/I_b ratio indicates a more complete oxidation of methanol with less poisonous species being produced. The enhanced electrochemical activity and improved anti-poisoning property can be attributed to the "bifunctional effect" when depositing Au onto Pt NTs.

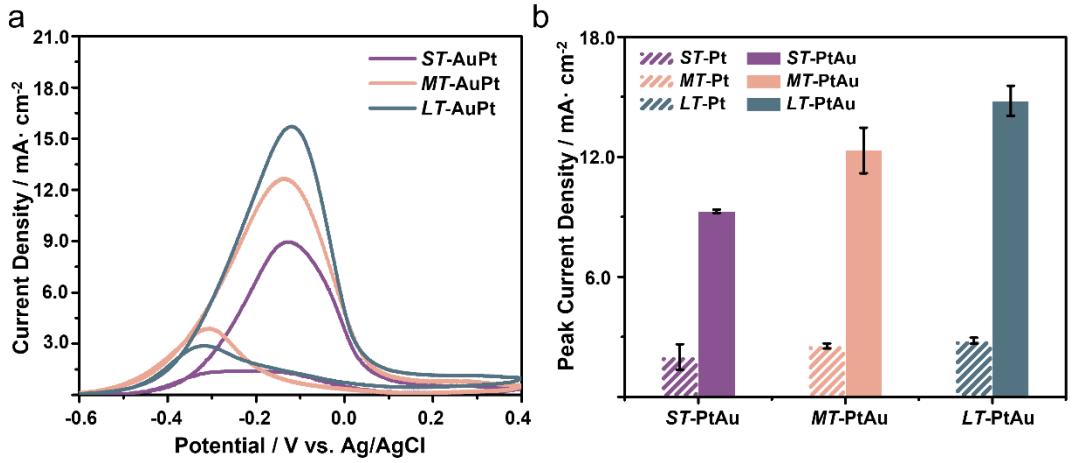

Figure 4.8 MOR performance of PtAu NTs of different lengths and the electrochemical activities comparison with their corresponding Pt NT templates. (a) CV scans of PtAu NTs of different lengths in an aqueous solution of 1M CH_3OH and 0.5 M NaOH. (b) The specific activity histogram comparison between the Pt NTs and PtAu NTs.

4.3.6 Enhanced MOR catalytic performance of PtAu NTs under laser irradiation

To avoid the photothermal effect from any carbon support, all NT samples were directly deposited on the GCE and tested.

The plasmon effect on MOR performance was first investigated by illuminating the PtAu NT modified electrodes with lasers of different wavelengths at different illuminance power intensities. Figure 4.9 presents the CV scans of MOR performance of *ST*-PtAu, *MT*-PtAu and *LT*-PtAu irradiated with a 532 nm laser, 671 nm laser, and 808 nm laser at power intensities of 0.25W·cm^{-2}, 0.5 W·cm^{-2}, 0.75 W·cm^{-2}, and 1W·cm^{-2}, which are compared to the MOR performance carried out under dark conditions. All peaks between -0.15 to 0.05 V (*vs*. Ag/AgCl) in the forward scan were ascribed to methanol electro-oxidation. Obviously, PtAu NTs of different lengths all

exhibited enhanced specific activities toward MOR under laser irradiation, when compared to the corresponding MOR activity under dark conditions. The magnitude of the light irradiation-induced specific peak current density increased as the laser power intensity increased. Specifically, for PtAu NTs of all lengths under investigation, the enhanced MOR performances induced by the 671 nm and 808 nm laser irradiation surpassed the MOR enhancement excited by the 532 nm laser.

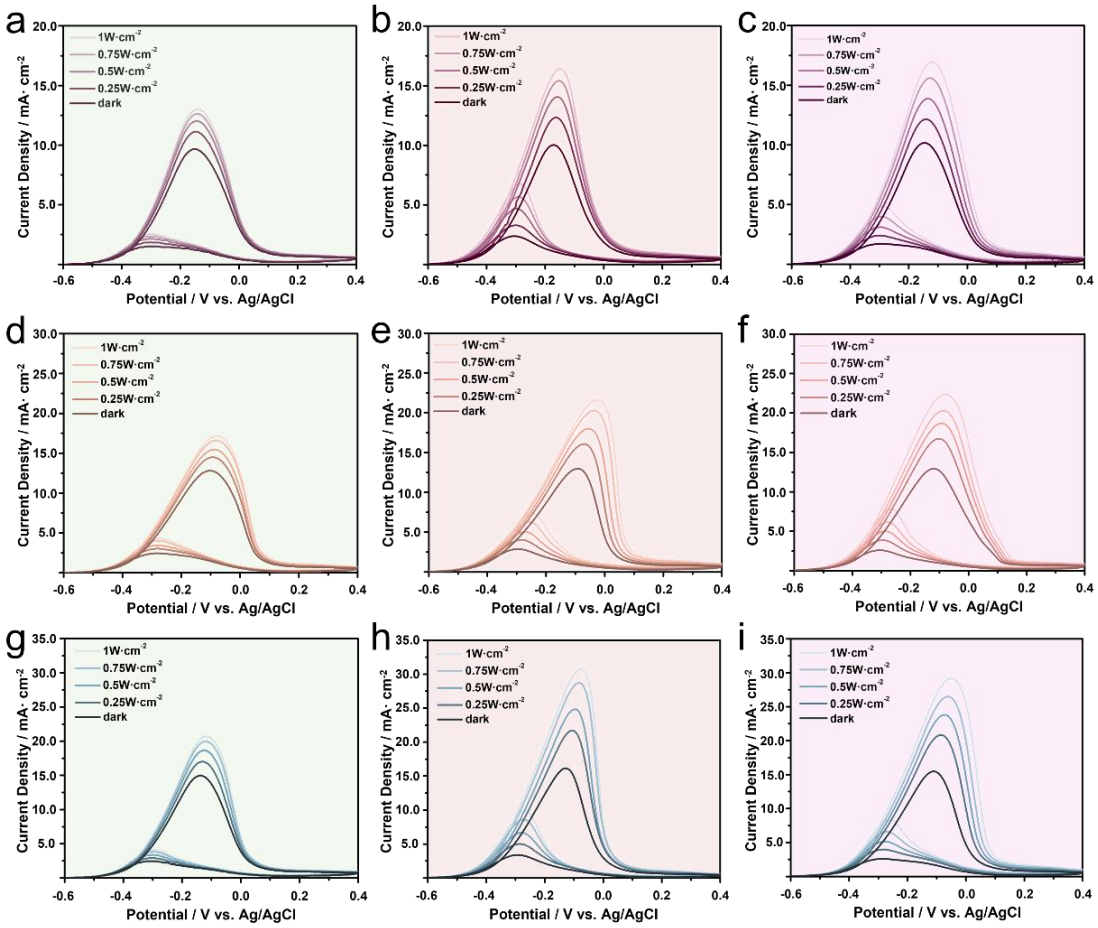

Figure 4.9 MOR performance of PtAu NTs of different lengths upon laser irradiation with different light power intensities (0.25W·cm^{-2}, 0.5 W·cm^{-2}, 0.75 W·cm^{-2}, and 1W·cm^{-2}) and under dark conditions (a-c) *ST*-PtAu irradiated by 532 nm, 671 nm, and 808 nm laser, respectively. (d-f) *MT*-PtAu irradiated by 532 nm, 671 nm, and 808 nm

laser, respectively. (g-i) *LT*-PtAu irradiated by 532 nm, 671 nm, and 808 nm laser, respectively.

To further elucidate and compare the laser-excitation induced enhancement and exclude the influence of the intrinsic electro-oxidation MOR performance, we defined a photoelectrochemical enhancement factor (PEEF) as $(j_P-j_0)/j_0$. Here, j_p and j_0 were the peak current density under light irradiation and peak current density under dark conditions, respectively. The PEEFs of PtAu NTs of different lengths were calculated and listed in Table 4.4.

Under 532 nm laser irradiation, the calculated PEEFs were almost identical for *ST*-PtAu, *MT*-PtAu and *LT*-PtAu at each applied light power intensity. When irradiating with 671 nm and 808 nm lasers, all PtAu NTs exhibited higher PEEFs, indicating the PtAu NTs shows higher photoelectrochemical response at longer wavelengths. *LT*-PtAu exhibited the highest PEEF values at all laser irradiation wavelengths, compared to those of *ST*-PtAu and *MT*-PtAu, respectively. We assume that higher LSPR absorption of *LT*-PtAu at longer wavelengths (Figure 4.3), owing to the geometric-dependent superposition of the L-Ext and T-Ext LSPR modes, contributed to the better photocatalytic performance of *LT*-PtAu.

It is worth noting that the PEEF value was not proportional to the extinction at selected laser wavelengths. The extinction ratio from experimental spectra at 532 nm, 671 nm and 808 nm for *ST*-PtAu, *MT*-PtAu and *LT*-PtAu were calculated to be 0.9:1:0.99, 0.9:1:0.99, and 0.81:0.95:1. Comparatively, the k_{PEEF} ratios were 0.47:0.84:1, 0.55:1:0.97, and 0.41:0.99:1 at 532 nm, 671 nm, and 808 nm for *ST*-PtAu, *MT*-PtAu

and *LT*-PtAu, respectively. The k_{PEEF} is defined as the slope of PEEF over the light intensity and is used to compare the photocurrent response of PtAu NTs of different lengths under laser irradiation. The discrepancy between the extinction ratio and the k_{PEEF} ratio was attributed to the energy transfer efficiency difference between Pt and Au in the visible-NIR range. The energy transfer efficiency from the plasmonic metal Au to the catalytic metal Pt was suppressed before 550 nm and gradually increased as the LSPR band moved to longer wavelengths, based off modeling anisotropic Au@Pt core-shell nanostructures[52]. Thus, though the extinction of PtAu NTs at 532 nm was of a similar value as the extinction at 671 nm and 808 nm, the low energy transfer efficiency from Au to Pt results in a lower PEEF as compared to the PEEF values at 671 nm and 808 nm.

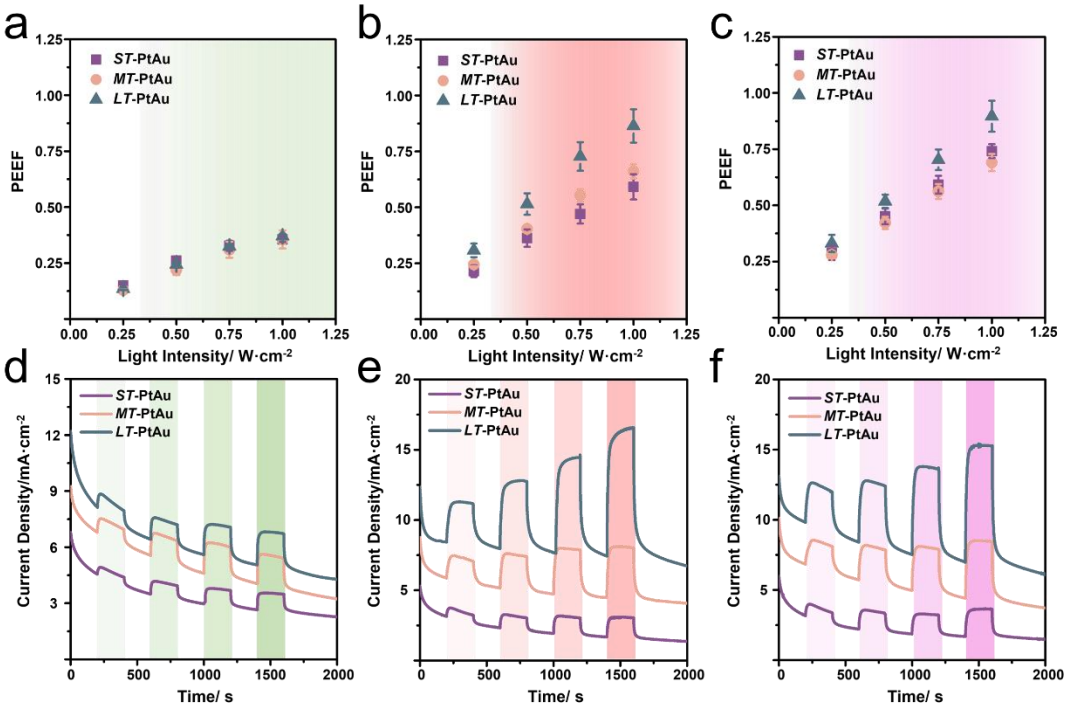

Figure 4.10 (a-c) PEEF values as a function of light intensity for *ST*-PtAu, *MT*-PtAu and *LT*-PtAu irradiated by 532 nm, 671 nm and 808 nm laser. (d-f) Amperometric

photocurrent response at -0.1 V (*vs.* Ag/AgCl) for *ST*-PtAu, *MT*-PtAu and *LT*-PtAu irradiated by 532 nm, 671 nm, and 808 nm laser.

Table 4.4 Calculated PEEF values of PtAu NTs of different lengths irradiated by different laser wavelengths at different light intensities.

Laser Wavelength	Light Intensity ($W \cdot cm^{-2}$)	*ST*-PtAu	*MT*-PtAu	*LT*-PtAu
532 nm	0.25	0.15±0.01	0.13±0.01	0.14±0.01
	0.5	0.26±0.02	0.22±0.02	0.24±0.01
	0.75	0.33±0.02	0.31±0.03	0.32±0.01
	1.0	0.36±0.01	0.36±0.04	0.37±0.01
671 nm	0.25	0.21±0.03	0.24±0.01	0.31±0.03
	0.5	0.36±0.04	0.40±0.02	0.51±0.05
	0.75	0.47±0.04	0.55±0.03	0.73±0.06
	1.0	0.59±0.06	0.66±0.03	0.86±0.07
808 nm	0.25	0.29±0.03	0.28±0.02	0.33±0.04
	0.5	0.45±0.04	0.42±0.03	0.52±0.03
	0.75	0.59±0.04	0.56±0.03	0.70±0.05
	1.0	0.74±0.03	0.69±0.04	0.90±0.07

Table 4.5 Extinction values at 532 nm, 671 nm, and 808 nm from the experimental visible-NIR spectra of PtAu NTs of different lengths and the k_{PEEF} of PtAu NTs of different lengths under 532nm, 671 nm, and 808 nm laser irradiation.

	ST-PtAu		*MT*-PtAu		*LT*-PtAu	
	Ext	*k*	Ext	*k*	Ext	*k*
532 nm	0.73	0.47	0.73	0.55	0.72	0.41
671 nm	0.82	0.84	0.81	1	0.85	0.99
808 nm	0.80	1	0.80	0.97	0.89	1

Amperometric *i-t* curves were recorded in the mixture solution containing 1M CH_3OH and 0.5 M NaOH at a fixed potential -0.1V (*vs.* Ag/AgCl). The photocurrent response of the PtAu NTs, upon laser irradiation, was examined after stabilizing under dark conditions for 200s; afterwards, the irradiation was chopped every 200s (Figure 4.10 d-f). The photocurrent rapidly increased upon laser irradiation and gradually reached a maximum, which was attributed to both hot carriers and photothermal induced enhanced MOR performance.

4.3.7 Enhanced MOR catalytic performance of PtAu NTs under Xenon lamp irradiation

The photoelectrocatalytic performance of the PtAu NTs, driven by a broadband light source, such as sunlight, was further evaluated. A Xenon lamp equipped with a 440 nm cut-on filter was employed as the light source to provide the broadband visible-light. The spectrum of the Xenon lamp with the cut-on filter is presented in Figure 4.11a. To

further evaluate the performance of the PtAu NTs, *LT*-Pt and Au@Pt core-shell NRs were employed as control groups. The Au@Pt NRs exhibited a transverse LSPR bands at 525 nm and a broadened longitudinal LSPR band at 785 nm, respectively. Compared with the Au NR template, the longitudinal mode of the Au@Pt NRs blue-shifted due to the reduced AR after the Pt layer deposition. The Au/Pt ratio of the Au@Pt NRs was confirmed as 2 by EDX, similar to that of PtAu NTs.

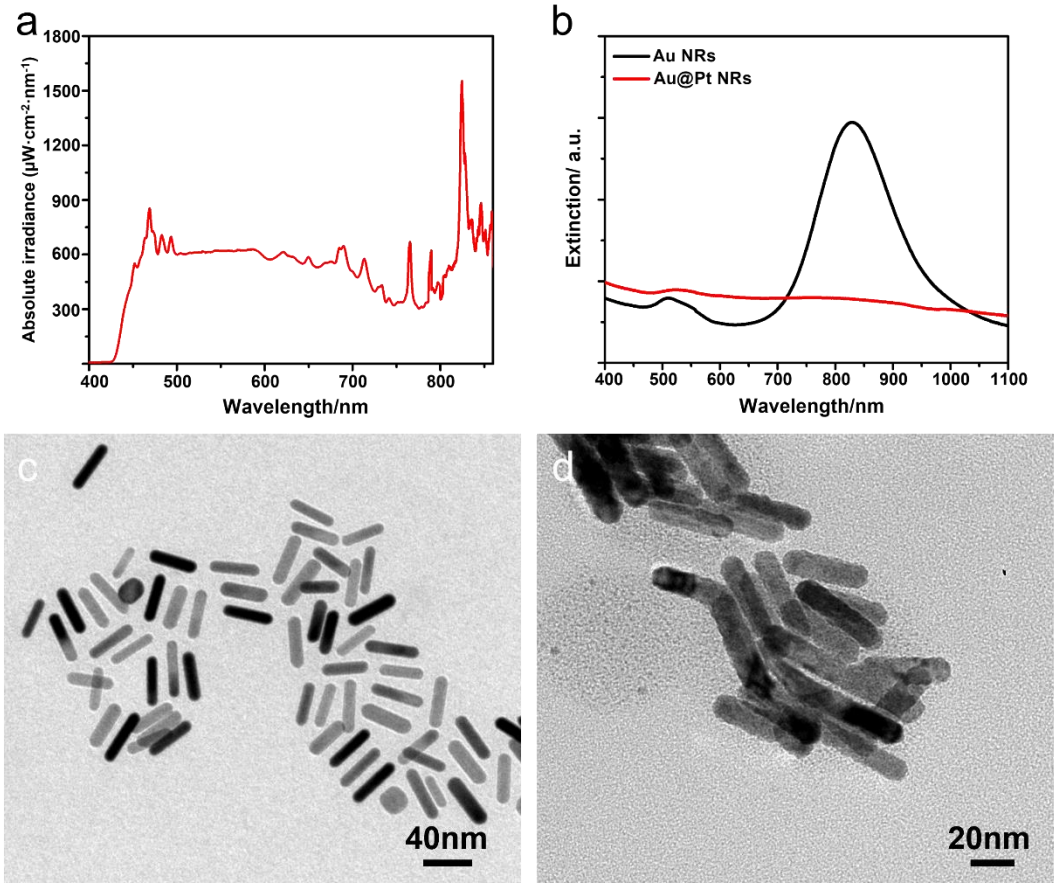

Figure 4.11 (a) Xenon lamp spectrum. (b) visible-NIR spectra of the Au NR templates and the Au@Pt NRs. (c-d) TEM images of Au NR templates and the corresponding synthesized Au@Pt NRs.

The photoelectrochemical catalytic performance of the PtAu NTs of different lengths, *LT*-Pt, and Au@Pt NRs are presented in Figure 4.12a. At each applied light power intensity (0.25, 0.5, 0.75, and 1W·cm^{-2}), the *LT*-PtAu exhibited the highest PEEFs under Xenon lamp irradiation. The PEEFs of *ST*-PtAu and *MT*-PtAu are comparable at applied light power densities and reached 0.75 and 0.73 under 1W·cm^{-2} irradiation, respectively (Figure 4.12b). Considering the intrinsic MOR electrochemical performance of the *ST*-PtAu, *MT*-PtAu and *LT*-PtAu, the *LT*-PtAu exhibited superior specific activities both under dark conditions and broadband light irradiation (Figure 4.12a). In comparison to the specific activity under dark conditions and the PEEFs for *LT*-Pt, the incorporation of plasmonic Au to Pt NTs not only improved the intrinsic electrochemical performance of the NTs, but also accelerated the MOR electrochemical kinetics under light irradiation. In the meantime, all PtAu NTs exhibited higher specific MOR activities under dark conditions compared to the Au@Pt core-shell NRs (7.63 mA·cm^{-2}), which was attributed to the advantage of hollow structures. The PEEFs of Au@Pt NRs was also significantly lower than the PtAu NTs of the same Au/Pt atomic ratios, which was assumed to be ascribed to the great suppression of the longitudinal mode of the Au@Pt NRs after Pt coating.

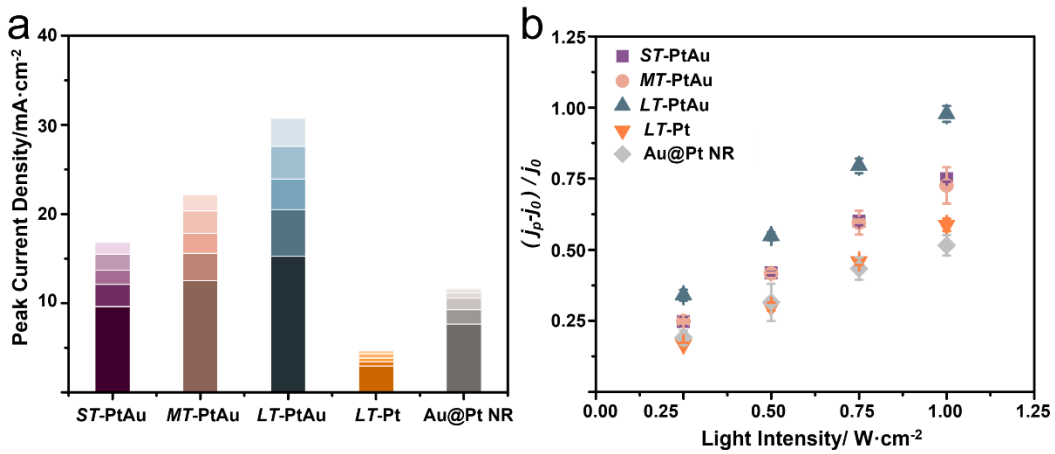

Figure 4.12 (a) MOR performance and (b) PEEF values as a function of light intensities (from bottom to top in Figure 4.12a: dark condition, 0.25, 0.5, 0.75, and 1W·cm^{-2}, respectively) for *ST*-PtAu, *MT*-PtAu, *LT*-PtAu, *LT*-Pt, and Au@Pt NRs irradiated by Xenon lamp.

4.4 Conclusions

In conclusion, we demonstrated that the *LT*-PtAu NTs, with larger LSPR absorption cross sections at longer wavelengths, exhibited better photoelectrocatalytic performances towards MOR under broadband light irradiation. The broader absorption cross section, in the visible-NIR region of the *LT*-PtAu, was achieved by adjusting the superposition of the L-Ext mode and the T-Ext mode of the PtAu NTs by tuning the length of the PtAu NTs. Three representative laser sources (532 nm, 671 nm, and 808 nm) were selected to examine the photoelectrocatalytic performance, and it was found that *LT*-PtAu exhibited the highest photoelectrochemical enhancement under light irradiation at each laser wavelength, compared with those of *ST*-PtAu and *MT*-PtAu. Meanwhile, the *LT*-PtAu possesses a higher intrinsic electrochemical performance

towards MOR under ambient light conditions, owing to its hollow tubular morphology. Thus, *LT*-PtAu is expected to serve as an excellent photoelectrocatalyst candidate fulfilling the requirements of: (1) intrinsic superior electrocatalytic performance and (2) effective light energy conversion. We hope this study can provide new insights for customizable photoelectrocatalyst design.

Chapter 5: Conclusions and Future Work

5.1 Conclusions

The objective of this dissertation is to design and fabricate PtAu NTs with tunable LSPR performance as photoelectrocatalysts to effectively drive electrochemical reactions under visible light irradiation. The LSPR dependence on the LT-AR, WT-AR and LW-AR allows PtAu NTs to reach maximum synergistic photoelectrochemical performance when combining the plasmonic entity and catalytic entity together.

In Chapter 2, we developed a novel synthetic strategy to fabricate ultrathin Pt NTs. The ultrathin Pt deposition was simply controlled by the concentration of the surfactant in the solution. We systematically investigated the synthesis conditions to control the desired morphology. Hollow Pt NTs can be formed when $c_{surf}^{+} < CMC$. As the c_{surf}^{+} approaches to the CMC value, well-dispersed Pt NTs with ultrathin walls are obtained. The generality of this approach was then further demonstrated as factors that increase the CMC value could facilitate the formation of ultrathin hollow Pt NTs. This synthetic strategy is demonstrated as a universal method in various reaction systems, where quaternary ammonium compounds serve as surfactants to direct the synthesis.

In Chapter 3, PtAu NTs with tunable parameters, including length, width, and thicknesses of the Pt and Au layers, were synthesized *via* a multi-stepwise synthesis strategy. The LSPR extinction band exhibited strong dependence on the dimension parameters of the PtAu NTs. Based off the FDTD simulation, the longitudinal and transverse LSPR band positions depend on the aspect ratios, including the ratio between the length/thickness, the ratio between width/thickness, the ratio between length/width,

and the thickness of the Pt and Au layers. Notably, the LSPR exhibits features of both rodlike and hollow structures. Delicate control over the dimensions can tune the LSPR band of the PtAu NTs from 600-820 nm in the visible-NIR range. Together, these findings allow for potential applications of PtAu NTs in visible-light driven catalysis.

In Chapter 4, we investigated the photoelectrocatalytic performance of PtAu NTs of different lengths under light irradiation. It was anticipated that all PtAu NTs would exhibit a greater photoelectrocatalytic response under longer wavelength light irradiation. More importantly, based off the superposition of the LSPR longitudinal mode and the transverse mode, we hypothesized that PtAu NTs, with extended length, would exhibit a great photoelectrocatalytic response. Subsequent experimental results supported all hypothesis we proposed. Together, with the superior intrinsic MOR activity of PtAu NTs, it is concluded that *LT*-PtAu can be considered as a good photoelectrocatalyst candidate, which can effectively convert light energy to chemical energy. This work was demonstrated as a successful example of theory-directed rational design of photoelectrocatalysts for future customizable catalyst design.

5.2 Future work

The development of multimetallic based photoelectrocatalysts to convert light energy to chemical energy has garnered particular interest in the field recently. A variety of multimetallic photoelectrocatalysts have been reported and demonstrated their application in various catalysis reactions. Despite the thriving development and remarkable progress in this field, many challenges, from the mechanism behind the scenes to the apparent enhanced catalytic efficiency, need to be surmounted. At the mechanism level, the differentiation among the enhancement field effect, the

photothermal effect, and the hot carrier effect is crucial to instruct the photocatalyst design. However, the fast recombination of the hot holes and electrons in the metal along with the inevitable photothermal effect from the plasmonic metal composition are bottleneck problems which hinder the exploration. Meanwhile, the mechanism of effective light energy transfer from the plasmonic entity to the catalytic entity is another key issue. Most research now follows a "trial and error" mode to find the optimized metal composition, composition ratio and spatial configuration of multiple components within one single entity. Although current reports reached an agreement that the reaction mechanisms can be significantly altered by light irradiation, no general trend for the customizable design of multimetallic photocatalyst structure has been summarized.

Additionally, it is crucial to evaluate the catalyst stability under light irradiation and scrutinize possible structure reconstructions during the photoelectrocatalytic process. It has been widely recognized that the electrocatalyst may lose its electrocatalytic performance during prolonged electrochemical operation due to phase segregation, dealloying, structure deformation, *etc*. Upon light irradiation, the inevitable photothermal effect may influence the surface atomic arrangement and induce catalyst sintering due to the difference in surface free energy of the components[83].

It should also be mentioned that current research in the field still lacks a standard design protocol for experimental setup. Home-made apparatuses are currently designed and adopted in different labs, leading to highly varied setups. The illumination conditions (such as intensity, flux, and light source spectra), the electrode structure, and the reactor geometry may all influence the reproducibility of the results.

Despite the bottleneck problems and challenges in this booming field, it is undisputed that the plasmonic photocatalysts pave a new avenue to effectively convert sustainable sunlight energy to drive chemical transformations; however, more insightful studies still need to be done in the future.

List of my publications

(1) **Zhang, Q.**, Yu, S.J., Kim, N., Zhao, Z., Peng, Y., Kong, C. C., Huang, Z.Q., Lee, S.B., Nie, Z.H. Tailoring optical property of ultrathin PtAu tubular nanostructure for high efficiency photocatalysis, *Manuscript in preparation*.

(2) **Zhang, Q.**, Huang, Z.Q., Yi C. L., Shen, X. X., Guo, H.Y., Kong, C. C., Lee, S.B., Nie, Z.H. Large scale fabrication of ultrathin Pt nanotubes *via* critical micelle concentration mediated heterogeneous nucleation, *Manuscript in preparation*.

(3) **Zhang, Q.**, Kim, N., Zhao, Z., Lee, S.B., Nie, Z.H. Plasmonic Photoelectrocatalysis, *Manuscript in preparation*.

(4) Zhao, Z., Kim, E., Chen, C.Y., Rzasa, J.R., **Zhang, Q.**, Li, J. Y., Tao, Y., Bentley, W.E., Lumb, J. P., Kohler, B., Payne, G.F. Orthogonal redox and optical stimuli lead to independent responses for catechol-chitosan films, *Submitted*

(5) Lin, X.Y., Kong, C.C., Webb, K., Yi, C.L., Zhang, S. Y., **Zhang Q.**, Fourkas J.T., Nie, Z.H. Polymeric ligand-mediated regioselective bonding of plasmonic nanoplates and nanospheres, *J. Am. Chem. Soc.*, 2020, 142, 41, 17282-17286.

(6) Guo, H., **Zhang, Q.**, Liu W., Nie, Z.H. Light-mediated shape transformation of a self-rolling nanocomposite hydrogel tube, *ACS Appl. Mater. Interfaces*, 2020, 12, 11, 13521-13528

(7) Gombedza, F., Evans, S., Shin, S., Boadi, E.A., **Zhang, Q.**, Nie, Z.H., Bandyopadhyay, B.C. Melamine promotes calcium crystal formation in three-dimensional microfluidic device, *Sci. Rep.*, 2019, 9, 875, 1-14

(8) Huang, Z.Q., Zhao, Z. J., **Zhang, Q.**, Han, L., Jiang, X. M., Li, C., Cardenas, M.T.P., Huang, P., Yin, J.J., Luo, J., Gong, J. L., Nie, Z. H. A welding phenomenon of dissimilar nanoparticles in dispersion, *Nat. Commun.*, 2019, 10, 219

(9) Jiang, X. M., He W. W., Zhang. X.W., Wu, Y., **Zhang, Q.**, Cao, G. J., Zhang, H., Zhang, J. W., Croley, T.R., Yin, J. J. Light-induced assembly of metal nanoparticles on ZnO enhances the generation of charge carriers, reactive oxygen species, and antibacterial activity, *J. Phys. Chem. C*, 2018, 122, 51, 29414-29425

(10) Yang, K.K., Liu, Y. J., L.Y., **Zhang, Q.**, Kong, C.C., Yi, C. L., Zhou, Z. J., Wang, Z. T., Zhang, G.G., Zhang, G.F., Zhang, Y., Khashab, N.M., Chen, X. Y., Nie, Z. H. Cooperative assembly of magneto-nanovesicles with tunable wall thickness and permeability for MRI-guided drug delivery, *J. Am. Chem. Soc.*, 2018, 140, 13, 4666-4677

(11) Cao, G. J., Fisher, C. M., Jiang, X. M., Chong, Y., Zhang, H., Guo, H. Y., **Zhang, Q.**, Zheng, J. W., Knolhoff, A. M., Croley, T. R., Yin, J. J. Platinum nanoparticles: An avenue for enhancing the release of nitric oxide from S-nitroso-N-acetylpenicillamine and S-nitrosoglutathione, *Nanoscale*, 2018, 10, 11176-11185

(12) Ye, H. H., Yang, K.K., Tao, J., Liu, Y. J., **Zhang, Q.**, Habibi, S., Nie, Z. H., Xia, X. H. An enzyme-free signal amplification technique for ultrasensitive colorimetric assay of disease biomarkers, *ACS Nano*, 2017, 11, 2, 2052-2059

(13) Lin, X. Y., Liu, Y., Lin, M. H., **Zhang, Q.**, Nie, Z. H. Synthesis of circular and triangular gold nanorings with tunable optical properties, *Chem. Comm.*, 2017, 53, 10765-10767

(14) Huang, Z.Q., Liu, Y. J., **Zhang, Q.**, Chang, X.X., Li, A., Deng, L., Yi, C. L., Yang, Y., Khashab, N. M., Gong, J. L., Nie, Z. H. Collapsed polymer-directed synthesis of multicomponent coaxial-like nanostructures, *Nat. Commun.*, 2016, 7, 12147

(15) Liu, Q., Cui, Z. M., **Zhang, Q.**, Guo, L. Gold-catalytic green synthesis of Cu_2O/Au/CuO hierarchical nanostructure and application for CO gas sensor, *Sci. Bull.*, 2014, 59, 7-10

(16) Huang, W.F., **Zhang, Q.**, Zhang. D.F., Zhou, J., Si, C., Guo, L., Chu, W. S., Wu, Z. Y. Investigation of structural and magnetic properties of CoPt/CoAu bimetallic nanochains by X-ray absorption spectroscopy, *J. Phys. Chem. C*, 2013, 117, 13, 6872-6879

(17) Zhang, D.F., **Zhang, Q.**, Huang, W. F., Guo, L., Chen, W. M., Chu, W. S., Chen, C. P., Wu, Z. Y. Low-temperature fabrication of Au-Co cluster mixed nanohybrids with high magnetic moment of Co, *ACS Appl. Mater. Interfaces*, 2012, 4, 10, 5643-5649

(18) Zhang, D.F., **Zhang, Q.**, Niu, L. Y., Jiang. L., Yin, P. G., Guo, L. Self-assembly of gold nanoparticles into chain-like structures and their optical properties, *J. Nanopart. Res.*, 2011, 13, 3923-3928

Bibliography

(1) Fujishima, A.; Honda, K. Electrochemical Photolysis of Water at a Semiconductor Electrode. *Nature* **1972**, *238* (5358), 37–38.

(2) Tong, H.; Ouyang, S.; Bi, Y.; Umezawa, N.; Oshikiri, M.; Ye, J. Nano-Photocatalytic Materials: Possibilities and Challenges. *Adv. Mater.* **2012**, *24* (2), 229–251.

(3) Jones, M. R.; Osberg, K. D.; Macfarlane, R. J.; Langille, M. R.; Mirkin, C. A. Templated Techniques for the Synthesis and Assembly of Plasmonic Nanostructures. *Chem. Rev.* **2011**, *111* (6), 3736–3827.

(4) Willets, K. A.; Van Duyne, R. P. Localized Surface Plasmon Resonance Spectroscopy and Sensing. *Annu. Rev. Phys. Chem.* **2007**, *58* (1), 267–297.

(5) Bastús, N. G.; Comenge, J.; Puntes, V. Kinetically Controlled Seeded Growth Synthesis of Citrate-Stabilized Gold Nanoparticles of up to 200 Nm: Size Focusing versus Ostwald Ripening. *Langmuir* **2011**, *27* (17), 11098–11105.

(6) Cao, J.; Sun, T.; Grattan, K. T. V. Gold Nanorod-Based Localized Surface Plasmon Resonance Biosensors: A Review. *Sens. Actuators B Chem.* **2014**, *195*, 332–351.

(7) Link, S.; Mohamed, M. B.; El-Sayed, M. A. Simulation of the Optical Absorption Spectra of Gold Nanorods as a Function of Their Aspect Ratio and the Effect of the Medium Dielectric Constant. *J. Phys. Chem. B* **1999**, *103* (16), 3073–3077.

(8) Ye, X.; Zheng, C.; Chen, J.; Gao, Y.; Murray, C. B. Using Binary Surfactant Mixtures To Simultaneously Improve the Dimensional Tunability and Monodispersity in the Seeded Growth of Gold Nanorods. *Nano Lett.* **2013**, *13* (2), 765–771.

(9) Oldenburg, S. J.; Averitt, R. D.; Westcott, S. L.; Halas, N. J. Nanoengineering of Optical Resonances. *Chem. Phys. Lett.* **1998**, *288* (2–4), 243–247.

(10) Schwartzberg, A. M.; Olson, T. Y.; Talley, C. E.; Zhang, J. Z. Synthesis, Characterization, and Tunable Optical Properties of Hollow Gold Nanospheres. *J. Phys. Chem. B* **2006**, *110* (40), 19935–19944.

(11) Chen, J.; McLellan, J. M.; Siekkinen, A.; Xiong, Y.; Li, Z.-Y.; Xia, Y. Facile Synthesis of Gold−Silver Nanocages with Controllable Pores on the Surface. *J. Am. Chem. Soc.* **2006**, *128* (46), 14776–14777.

(12) Sun, Y.; Xia, Y. Mechanistic Study on the Replacement Reaction between Silver Nanostructures and Chloroauric Acid in Aqueous Medium. *J. Am. Chem. Soc.* **2004**, *126* (12), 3892–3901.

(13) Prodan, E.; Radloff, C.; Halas, N. J.; Nordlander, P. A Hybridization Model for the Plasmon Response of Complex Nanostructures. *Science* **2003**, *302* (5644), 419–422.

(14) Genç, A.; Patarroyo, J.; Sancho-Parramon, J.; Bastús, N. G.; Puntes, V.; Arbiol, J. Hollow Metal Nanostructures for Enhanced Plasmonics: Synthesis, Local Plasmonic Properties and Applications. *Nanophotonics* **2017**, *6* (1), 193–213.

(15) Halas, N. Playing with Plasmons: Tuning the Optical Resonant Properties of Metallic Nanoshells. *MRS Bull.* **2005**, *30* (5), 362–367.

(16) Pissuwan, D.; Valenzuela, S. M.; Cortie, M. B. Therapeutic Possibilities of Plasmonically Heated Gold Nanoparticles. *Trends Biotechnol.* **2006**, *24* (2), 62–67.

(17) Linic, S.; Chavez, S.; Elias, R. Flow and Extraction of Energy and Charge Carriers in Hybrid Plasmonic Nanostructures. *Nat. Mater.* **2021**.

(18) Zhang, Y.; He, S.; Guo, W.; Hu, Y.; Huang, J.; Mulcahy, J. R.; Wei, W. D. Surface-Plasmon-Driven Hot Electron Photochemistry. *Chem. Rev.* **2018**, *118* (6), 2927–2954.

(19) Linic, S.; Christopher, P.; Ingram, D. B. Plasmonic-Metal Nanostructures for Efficient Conversion of Solar to Chemical Energy. *Nat. Mater.* **2011**, *10* (12), 911–921.

(20) Gellé, A.; Jin, T.; de la Garza, L.; Price, G. D.; Besteiro, L. V.; Moores, A. Applications of Plasmon-Enhanced Nanocatalysis to Organic Transformations. *Chem. Rev.* **2020**, *120* (2), 986–1041.

(21) Brongersma, M. L. Plasmon-Induced Hot Carrier Science and Technology. *Nat. Nanotechnol.* **2015**, *10*, 10.

(22) Govorov, A. O.; Zhang, W.; Skeini, T.; Richardson, H.; Lee, J.; Kotov, N. A. Gold Nanoparticle Ensembles as Heaters and Actuators: Melting and Collective Plasmon Resonances. *Nanoscale Res. Lett.* **2006**, *1* (1), 84.

(23) Govorov, A. O.; Richardson, H. H. Generating Heat with Metal Nanoparticles. *Nano Today* **2007**, *2* (1), 30–38.

(24) Mateo, D.; Cerrillo, J. L.; Durini, S.; Gascon, J. Fundamentals and Applications of Photo-Thermal Catalysis. *Chem. Soc. Rev.* **2021**, *50* (3), 2173–2210.

(25) Richardson, H. H.; Hickman, Z. N.; Govorov, A. O.; Thomas, A. C.; Zhang, W.; Kordesch, M. E. Thermooptical Properties of Gold Nanoparticles Embedded in Ice: Characterization of Heat Generation and Melting. *Nano Lett.* **2006**, *6* (4), 783–788.

(26) Fasciani, C.; Alejo, C. J. B.; Grenier, M.; Netto-Ferreira, J. C.; Scaiano, J. C. High-Temperature Organic Reactions at Room Temperature Using Plasmon Excitation: Decomposition of Dicumyl Peroxide. *Org. Lett.* **2011**, *13* (2), 204–207.

(27) Haas, K. M.; Lear, B. J. Billion-Fold Rate Enhancement of Urethane Polymerization via the Photothermal Effect of Plasmonic Gold Nanoparticles. *Chem. Sci.* **2015**, *6* (11), 6462–6467.

(28) Adleman, J. R.; Boyd, D. A.; Goodwin, D. G.; Psaltis, D. Heterogenous Catalysis Mediated by Plasmon Heating. *Nano Lett.* **2009**, *9* (12), 4417–4423.

(29) Yang, Q.; Xu, Q.; Yu, S.-H.; Jiang, H.-L. Pd Nanocubes@ZIF-8: Integration of Plasmon-Driven Photothermal Conversion with a Metal–Organic Framework for Efficient and Selective Catalysis. *Angew. Chem. Int. Ed.* **2016**, *55* (11), 3685–3689.

(30) Wang, F.; Huang, Y.; Chai, Z.; Zeng, M.; Li, Q.; Wang, Y.; Xu, D. Photothermal-Enhanced Catalysis in Core–Shell Plasmonic Hierarchical Cu_7S_4 Microsphere@zeolitic Imidazole Framework-8. *Chem. Sci.* **2016**, *7* (12), 6887–6893.

(31) Chen, Y.-Z.; Wang, Z. U.; Wang, H.; Lu, J.; Yu, S.-H.; Jiang, H.-L. Singlet Oxygen-Engaged Selective Photo-Oxidation over Pt Nanocrystals/Porphyrinic MOF: The Roles of Photothermal Effect and Pt Electronic State. *J. Am. Chem. Soc.* **2017**, *139* (5), 2035–2044.

(32) Ding, S.-Y.; Yi, J.; Li, J.-F.; Ren, B.; Wu, D.-Y.; Panneerselvam, R.; Tian, Z.-Q. Nanostructure-Based Plasmon-Enhanced Raman Spectroscopy for Surface Analysis of Materials. *Nat. Rev. Mater.* **2016**, *1* (6), 16021.

(33) Liu, D.; Xue, C. Plasmonic Coupling Architectures for Enhanced Photocatalysis. *Adv. Mater.* *33* (46), 2005738.

(34) Stamplecoskie, K. G.; Pacioni, N. L.; Larson, D.; Scaiano, J. C. Plasmon-Mediated Photopolymerization Maps Plasmon Fields for Silver Nanoparticles. *J. Am. Chem. Soc.* **2011**, *133* (24), 9160–9163.

(35) Liu, Z.; Hou, W.; Pavaskar, P.; Aykol, M.; Cronin, S. B. Plasmon Resonant Enhancement of Photocatalytic Water Splitting Under Visible Illumination. *Nano Lett.* **2011**, *11* (3), 1111–1116.

(36) Zhang, X.; Du, A.; Zhu, H.; Jia, J.; Wang, J.; Ke, X. Surface Plasmon-Enhanced Zeolite Catalysis under Light Irradiation and Its Correlation with Molecular Polarity of Reactants. *Chem Commun* **2014**, *50* (90), 13893–13895.

(37) Bernardi, M.; Mustafa, J.; Neaton, J. B.; Louie, S. G. Theory and Computation of Hot Carriers Generated by Surface Plasmon Polaritons in Noble Metals. *Nat. Commun.* **2015**, *6* (1), 7044.

(38) Ahlawat, M.; Mittal, D.; Govind Rao, V. Plasmon-Induced Hot-Hole Generation and Extraction at Nano-Heterointerfaces for Photocatalysis. *Commun. Mater.* **2021**, *2* (1), 114.

(39) Zhang, C.; Jia, F.; Li, Z.; Huang, X.; Lu, G. Plasmon-Generated Hot Holes for Chemical Reactions. *Nano Res.* **2020**, *13* (12), 3183–3197.

(40) Aslam, U.; Rao, V. G.; Chavez, S.; Linic, S. Catalytic Conversion of Solar to Chemical Energy on Plasmonic Metal Nanostructures. *Nat. Catal.* **2018**, *1* (9), 656–665.

(41) Qian, K.; Sweeny, B. C.; Johnston-Peck, A. C.; Niu, W.; Graham, J. O.; DuChene, J. S.; Qiu, J.; Wang, Y.-C.; Engelhard, M. H.; Su, D.; Stach, E. A.; Wei, W. D. Surface Plasmon-Driven Water Reduction: Gold Nanoparticle Size Matters. *J. Am. Chem. Soc.* **2014**, *136* (28), 9842–9845.

(42) Knight, M. W.; Sobhani, H.; Nordlander, P.; Halas, N. J. Photodetection with Active Optical Antennas. *Science* **2011**, *332* (6030), 702–704.

(43) Clavero, C. Plasmon-Induced Hot-Electron Generation at Nanoparticle/Metal-Oxide Interfaces for Photovoltaic and Photocatalytic Devices. *Nat. Photonics* **2014**, *8* (2), 95–103.

(44) DuChene, J. S.; Sweeny, B. C.; Johnston-Peck, A. C.; Su, D.; Stach, E. A.; Wei, W. D. Prolonged Hot Electron Dynamics in Plasmonic-Metal/Semiconductor Heterostructures with Implications for Solar Photocatalysis. *Angew. Chem. Int. Ed.* **2014**, *53* (30), 7887–7891.

(45) Zhang, P.; Wang, T.; Gong, J. Mechanistic Understanding of the Plasmonic Enhancement for Solar Water Splitting. *Adv. Mater.* **2015**, *27* (36), 5328–5342.

(46) Mubeen, S.; Lee, J.; Singh, N.; Krämer, S.; Stucky, G. D.; Moskovits, M. An Autonomous Photosynthetic Device in Which All Charge Carriers Derive from Surface Plasmons. *Nat. Nanotechnol.* **2013**, *8* (4), 247–251.

(47) Gomes Silva, C.; Juárez, R.; Marino, T.; Molinari, R.; García, H. Influence of Excitation Wavelength (UV or Visible Light) on the Photocatalytic Activity of Titania

Containing Gold Nanoparticles for the Generation of Hydrogen or Oxygen from Water. *J. Am. Chem. Soc.* **2011**, *133* (3), 595–602.

(48) Liu, G.; Li, P.; Zhao, G.; Wang, X.; Kong, J.; Liu, H.; Zhang, H.; Chang, K.; Meng, X.; Kako, T.; Ye, J. Promoting Active Species Generation by Plasmon-Induced Hot-Electron Excitation for Efficient Electrocatalytic Oxygen Evolution. *J. Am. Chem. Soc.* **2016**, *138* (29), 9128–9136.

(49) Robatjazi, H.; Zhao, H.; Swearer, D. F.; Hogan, N. J.; Zhou, L.; Alabastri, A.; McClain, M. J.; Nordlander, P.; Halas, N. J. Plasmon-Induced Selective Carbon Dioxide Conversion on Earth-Abundant Aluminum-Cuprous Oxide Antenna-Reactor Nanoparticles. *Nat. Commun.* **2017**, *8* (1), 27.

(50) Hou, W.; Hung, W. H.; Pavaskar, P.; Goeppert, A.; Aykol, M.; Cronin, S. B. Photocatalytic Conversion of CO_2 to Hydrocarbon Fuels via Plasmon-Enhanced Absorption and Metallic Interband Transitions. *ACS Catal.* **2011**, *1* (8), 929–936.

(51) Wang, C.; Astruc, D. Nanogold Plasmonic Photocatalysis for Organic Synthesis and Clean Energy Conversion. *Chem Soc Rev* **2014**, *43* (20), 7188–7216.

(52) Chavez, S.; Aslam, U.; Linic, S. Design Principles for Directing Energy and Energetic Charge Flow in Multicomponent Plasmonic Nanostructures. *ACS Energy Lett.* **2018**, *3* (7), 1590–1596.

(53) Aslam, U.; Chavez, S.; Linic, S. Controlling Energy Flow in Multimetallic Nanostructures for Plasmonic Catalysis. *Nat. Nanotechnol.* **2017**, *12* (10), 1000–1005.

(54) Lee, S.; Hwang, H.; Lee, W.; Schebarchov, D.; Wy, Y.; Grand, J.; Auguié, B.; Wi, D. H.; Cortés, E.; Han, S. W. Core–Shell Bimetallic Nanoparticle Trimers for

Efficient Light-to-Chemical Energy Conversion. *ACS Energy Lett.* **2020**, *5* (12), 3881–3890.

(55) Vadai, M.; Angell, D. K.; Hayee, F.; Sytwu, K.; Dionne, J. A. In-Situ Observation of Plasmon-Controlled Photocatalytic Dehydrogenation of Individual Palladium Nanoparticles. *Nat. Commun.* **2018**, *9* (1), 4658.

(56) Li, K.; Hogan, N. J.; Kale, M. J.; Halas, N. J.; Nordlander, P.; Christopher, P. Balancing Near-Field Enhancement, Absorption, and Scattering for Effective Antenna–Reactor Plasmonic Photocatalysis. *Nano Lett.* **2017**, *17* (6), 3710–3717.

(57) Quiroz, J.; Barbosa, E. C. M.; Araujo, T. P.; Fiorio, J. L.; Wang, Y.-C.; Zou, Y.-C.; Mou, T.; Alves, T. V.; de Oliveira, D. C.; Wang, B.; Haigh, S. J.; Rossi, L. M.; Camargo, P. H. C. Controlling Reaction Selectivity over Hybrid Plasmonic Nanocatalysts. *Nano Lett* **2018**, 9.

(58) Rao, V. G.; Aslam, U.; Linic, S. Chemical Requirement for Extracting Energetic Charge Carriers from Plasmonic Metal Nanoparticles to Perform Electron-Transfer Reactions. *J. Am. Chem. Soc.* **2019**, *141* (1), 643–647.

(59) Engelbrekt, C.; Crampton, K. T.; Fishman, D. A.; Law, M.; Apkarian, V. A. Efficient Plasmon-Mediated Energy Funneling to the Surface of Au@Pt Core–Shell Nanocrystals. *ACS Nano* **2020**, *14* (4), 5061–5074.

(60) Zhou, L.; Martirez, J. M. P.; Finzel, J.; Zhang, C.; Swearer, D. F.; Tian, S.; Robatjazi, H.; Lou, M.; Dong, L.; Henderson, L.; Christopher, P.; Carter, E. A.; Nordlander, P.; Halas, N. J. Light-Driven Methane Dry Reforming with Single Atomic Site Antenna-Reactor Plasmonic Photocatalysts. *Nat. Energy* **2020**, *5* (1), 61–70.

(61) Yang, X.; Wang, D. Photocatalysis: From Fundamental Principles to Materials and Applications. *ACS Appl. Energy Mater.* **2018**, *1* (12), 6657–6693.

(62) Wang, C.; Nie, X.-G.; Shi, Y.; Zhou, Y.; Xu, J.-J.; Xia, X.-H.; Chen, H.-Y. Direct Plasmon-Accelerated Electrochemical Reaction on Gold Nanoparticles. *ACS Nano* **2017**, *11* (6), 5897–5905.

(63) Huang, L.; Zou, J.; Ye, J.; Zhou, Z.; Lin, Z.; Kang, X.; Jain, P. K.; Chen, S. Synergy between Plasmonic and Electrocatalytic Activation of Methanol Oxidation on Palladium–Silver Alloy Nanotubes. *Angew. Chem. Int. Ed.* **2019**, *58* (26), 8794–8798.

(64) Bi, J.; Gao, P.; Wang, B.; Yu, X.; Kong, C.; Xu, L.; Zhang, X.; Yang, S. Intrinsic Insight on Localized Surface Plasmon Resonance Enhanced Methanol Electro-Oxidation over a Au@AgPt Hollow Urchin-like Nanostructure. *J. Mater. Chem. A* **2020**, *8* (14), 6638–6646.

(65) Zhang, Y.; Guo, W.; Zhang, Y.; Wei, W. D. Plasmonic Photoelectrochemistry: In View of Hot Carriers. *Adv. Mater. 33* (46), 2006654.

(66) Lin, S.-C.; Hsu, C.-S.; Chiu, S.-Y.; Liao, T.-Y.; Chen, H. M. Edgeless Ag–Pt Bimetallic Nanocages: In Situ Monitor Plasmon-Induced Suppression of Hydrogen Peroxide Formation. *J. Am. Chem. Soc.* **2017**, *139* (6), 2224–2233.

(67) Zheng, Z.; Xie, W.; Li, M.; Ng, Y. H.; Wang, D.-W.; Dai, Y.; Huang, B.; Amal, R. Platinum Electrocatalysts with Plasmonic Nano-Cores for Photo-Enhanced Oxygen-Reduction. *Nano Energy* **2017**, *41*, 233–242.

(68) Kim, Y.; Creel, E. B.; Corson, E. R.; McCloskey, B. D.; Urban, J. J.; Kostecki, R. Surface-Plasmon-Assisted Photoelectrochemical Reduction of CO_2 and NO_3^- on Nanostructured Silver Electrodes. *Adv. Energy Mater.* **2018**, *8* (22), 1800363.

(69) Yu, E. H.; Krewer, U.; Scott, K. Principles and Materials Aspects of Direct Alkaline Alcohol Fuel Cells. *Energies* **2010**, *3* (8), 1499–1528.

(70) Antolini, E. Catalysts for Direct Ethanol Fuel Cells. *J. Power Sources* **2007**, *170* (1), 1–12.

(71) Long, N. V.; Yang, Y.; Minh Thi, C.; Minh, N. V.; Cao, Y.; Nogami, M. The Development of Mixture, Alloy, and Core-Shell Nanocatalysts with Nanomaterial Supports for Energy Conversion in Low-Temperature Fuel Cells. *Nano Energy* **2013**, *2* (5), 636–676.

(72) Strasser, P.; Koh, S.; Anniyev, T.; Greeley, J.; More, K.; Yu, C.; Liu, Z.; Kaya, S.; Nordlund, D.; Ogasawara, H.; Toney, M. F.; Nilsson, A. Lattice-Strain Control of the Activity in Dealloyed Core–Shell Fuel Cell Catalysts. *Nat. Chem.* **2010**, *2* (6), 454–460.

(73) Liu, H.; Nosheen, F.; Wang, X. Noble Metal Alloy Complex Nanostructures: Controllable Synthesis and Their Electrochemical Property. *Chem. Soc. Rev.* **2015**, *44* (10), 3056–3078.

(74) Maroun, F.; Ozanam, F.; Magnussen, O. M.; Behm, R. J. The Role of Atomic Ensembles in the Reactivity of Bimetallic Electrocatalysts. *Science* **2001**, *293* (5536), 1811–1814.

(75) Wang, Y.; Cao, L.; Libretto, N. J.; Li, X.; Li, C.; Wan, Y.; He, C.; Lee, J.; Gregg, J.; Zong, H.; Su, D.; Miller, J. T.; Mueller, T.; Wang, C. Ensemble Effect in Bimetallic Electrocatalysts for CO_2 Reduction. *J. Am. Chem. Soc.* **2019**, *141* (42), 16635–16642.

(76) Liu, P.; Nørskov, J. K. Ligand and Ensemble Effects in Adsorption on Alloy Surfaces. *Phys. Chem. Chem. Phys.* **2001**, *3* (17), 3814–3818.

(77) Chen, M.; Kumar, D.; Yi, C.-W.; Goodman, D. W. The Promotional Effect of Gold in Catalysis by Palladium-Gold. *Science* **2005**, *310* (5746), 291–293.

(78) Wang, Y.; Wang, D.; Li, Y. A Fundamental Comprehension and Recent Progress in Advanced Pt-Based ORR Nanocatalysts. *SmartMat* **2021**, *2* (1), 56–75.

(79) Watanabe, M.; Motoo, S. Electrocatalysis by Ad-Atoms. *J. Electroanal. Chem. Interfacial Electrochem.* **1975**, *60* (3), 267–273.

(80) Kua, J.; Goddard, W. A. Oxidation of Methanol on 2nd and 3rd Row Group VIII Transition Metals (Pt, Ir, Os, Pd, Rh, and Ru): Application to Direct Methanol Fuel Cells. *J. Am. Chem. Soc.* **1999**, *121* (47), 10928–10941.

(81) Zhong, C.-J.; Luo, J.; Fang, B.; Wanjala, B. N.; Njoki, P. N.; Loukrakpam, R.; Yin, J. Nanostructured Catalysts in Fuel Cells. *Nanotechnology* **2010**, *21* (6), 062001.

(82) Suntivich, J.; Xu, Z.; Carlton, C. E.; Kim, J.; Han, B.; Lee, S. W.; Bonnet, N.; Marzari, N.; Allard, L. F.; Gasteiger, H. A.; Hamad-Schifferli, K.; Shao-Horn, Y. Surface Composition Tuning of Au–Pt Bimetallic Nanoparticles for Enhanced Carbon Monoxide and Methanol Electro-Oxidation. *J. Am. Chem. Soc.* **2013**, *135* (21), 7985–7991.

(83) Wanjala, B. N.; Luo, J.; Fang, B.; Mott, D.; Zhong, C.-J. Gold-Platinum Nanoparticles: Alloying and Phase Segregation. *J Mater Chem* **2011**, *21* (12), 4012–4020.

(84) Greeley, J.; Nørskov, J. K.; Mavrikakis, M. Electronic Structure and Catalysis on Metal Surfaces. *Annu. Rev. Phys. Chem.* **2002**, *53* (1), 319–348.

(85) Ruban, A.; Hammer, B.; Stoltze, P.; Skriver, H. L.; Nørskov, J. K. Surface Electronic Structure and Reactivity of Transition and Noble Metals. **1997**, 9.

(86) Stamenkovic, V. R.; Mun, B. S.; Arenz, M.; Mayrhofer, K. J. J.; Lucas, C. A.; Wang, G.; Ross, P. N.; Markovic, N. M. Trends in Electrocatalysis on Extended and Nanoscale Pt-Bimetallic Alloy Surfaces. *Nat. Mater.* **2007**, *6* (3), 241–247.

(87) Demirci, U. B. Theoretical Means for Searching Bimetallic Alloys as Anode Electrocatalysts for Direct Liquid-Feed Fuel Cells. *J. Power Sources* **2007**, *173* (1), 11–18.

(88) Kim, J.; Kim, H.; Lee, W.-J.; Ruqia, B.; Baik, H.; Oh, H.-S.; Paek, S.-M.; Lim, H.-K.; Choi, C. H.; Choi, S.-I. Theoretical and Experimental Understanding of Hydrogen Evolution Reaction Kinetics in Alkaline Electrolytes with Pt-Based Core–Shell Nanocrystals. *J. Am. Chem. Soc.* **2019**, *141* (45), 18256–18263.

(89) Mavrikakis, M.; Hammer, B.; Nørskov, J. K. Effect of Strain on the Reactivity of Metal Surfaces. *Phys. Rev. Lett.* **1998**, *81* (13), 2819–2822.

(90) Wang, W.; Lv, F.; Lei, B.; Wan, S.; Luo, M.; Guo, S. Tuning Nanowires and Nanotubes for Efficient Fuel-Cell Electrocatalysis. *Adv. Mater.* **2016**, *28* (46), 10117–10141.

(91) Tian, X. L.; Wang, L.; Deng, P.; Chen, Y.; Xia, B. Y. Research Advances in Unsupported Pt-Based Catalysts for Electrochemical Methanol Oxidation. *J. Energy Chem.* **2017**, *26* (6), 1067–1076.

(92) Wang, J.; Cui, Y.; Wang, D. Design of Hollow Nanostructures for Energy Storage, Conversion and Production. *Adv. Mater.* **2019**, *31* (38), 1801993.

(93) Park, J.; Kwon, T.; Kim, J.; Jin, H.; Kim, H. Y.; Kim, B.; Joo, S. H.; Lee, K. Hollow Nanoparticles as Emerging Electrocatalysts for Renewable Energy Conversion Reactions. *Chem. Soc. Rev.* **2018**, *47* (22), 8173–8202.

(94) Li, Y.; Shi, J. Hollow-Structured Mesoporous Materials: Chemical Synthesis, Functionalization and Applications. *Adv. Mater.* **2014**, *26* (20), 3176–3205.

(95) Pei, F.; An, T.; Zang, J.; Zhao, X.; Fang, X.; Zheng, M.; Dong, Q.; Zheng, N. From Hollow Carbon Spheres to N-Doped Hollow Porous Carbon Bowls: Rational Design of Hollow Carbon Host for Li-S Batteries. *Adv. Energy Mater.* **2016**, *6* (8), 1502539.

(96) Xia, X.; Wang, Y.; Ruditskiy, A.; Xia, Y. 25th Anniversary Article: Galvanic Replacement: A Simple and Versatile Route to Hollow Nanostructures with Tunable and Well-Controlled Properties. *Adv. Mater.* **2013**, *25* (44), 6313–6333.

(97) Oh, M. H.; Yu, T.; Yu, S.-H.; Lim, B.; Ko, K.-T.; Willinger, M.-G.; Seo, D.-H.; Kim, B. H.; Cho, M. G.; Park, J.-H.; Kang, K.; Sung, Y.-E.; Pinna, N.; Hyeon, T. Galvanic Replacement Reactions in Metal Oxide Nanocrystals. *Science* **2013**, *340* (6135), 964–968.

(98) Sun, Y.; Mayers, B. T.; Xia, Y. Template-Engaged Replacement Reaction: A One-Step Approach to the Large-Scale Synthesis of Metal Nanostructures with Hollow Interiors. *Nano Lett.* **2002**, *2* (5), 481–485.

(99) da Silva, A. G. M.; Rodrigues, T. S.; Haigh, S. J.; Camargo, P. H. C. Galvanic Replacement Reaction: Recent Developments for Engineering Metal Nanostructures towards Catalytic Applications. *Chem. Commun.* **2017**, *53* (53), 7135–7148.

(100) Zhang, H.; Jin, M.; Wang, J.; Li, W.; Camargo, P. H. C.; Kim, M. J.; Yang, D.; Xie, Z.; Xia, Y. Synthesis of Pd−Pt Bimetallic Nanocrystals with a Concave Structure through a Bromide-Induced Galvanic Replacement Reaction. *J. Am. Chem. Soc.* **2011**, *133* (15), 6078–6089.

(101) Susman, M. D.; Popovitz-Biro, R.; Vaskevich, A.; Rubinstein, I. PH-Dependent Galvanic Replacement of Supported and Colloidal Cu_2O Nanocrystals with Gold and Palladium. *Small* **2015**, *11* (32), 3942–3953.

(102) Han, L.; Wang, P.; Liu, H.; Tan, Q.; Yang, J. Balancing the Galvanic Replacement and Reduction Kinetics for the General Formation of Bimetallic CuM (M = Ru, Rh, Pd, Os, Ir, and Pt) Hollow Nanostructures. *J. Mater. Chem. A* **2016**, *4* (47), 18354–18365.

(103) Zhang, W.; Yang, J.; Lu, X. Tailoring Galvanic Replacement Reaction for the Preparation of Pt/Ag Bimetallic Hollow Nanostructures with Controlled Number of Voids. *ACS Nano* **2012**, *6* (8), 7397–7405.

(104) Yin, Y.; Rioux, R. M.; Erdonmez, C. K.; Hughes, S.; Somorjai, G. A.; Alivisatos, A. P. Formation of Hollow Nanocrystals Through the Nanoscale Kirkendall Effect. *Science* **2004**, *304* (5671), 711–714.

(105) Fan, H. J.; Knez, M.; Scholz, R.; Hesse, D.; Nielsch, K.; Zacharias, M.; Gösele, U. Influence of Surface Diffusion on the Formation of Hollow Nanostructures Induced by the Kirkendall Effect: The Basic Concept. *Nano Lett.* **2007**, *7* (4), 993–997.

(106) Chiang, R.-K.; Chiang, R.-T. Formation of Hollow Ni_2P Nanoparticles Based on the Nanoscale Kirkendall Effect. *Inorg. Chem.* **2007**, *46* (2), 369–371.

(107) Peng, S.; Sun, S. Synthesis and Characterization of Monodisperse Hollow Fe_3O_4 Nanoparticles. *Angew. Chem. Int. Ed.* **2007**, *46* (22), 4155–4158.

(108) Cabot, A.; Smith, R. K.; Yin, Y.; Zheng, H.; Reinhard, B. M.; Liu, H.; Alivisatos, A. P. Sulfidation of Cadmium at the Nanoscale. *ACS Nano* **2008**, *2* (7), 1452–1458.

(109) Cabot, A.; Puntes, V. F.; Shevchenko, E.; Yin, Y.; Balcells, L.; Marcus, M. A.; Hughes, S. M.; Alivisatos, A. P. Vacancy Coalescence during Oxidation of Iron Nanoparticles. *J. Am. Chem. Soc.* **2007**, *129* (34), 10358–10360.

(110) Bernard Ng, C. H.; Tan, H.; Fan, W. Y. Formation of Ag_2Se Nanotubes and Dendrite-like Structures from UV Irradiation of a CSe_2/Ag Colloidal Solution. *Langmuir* **2006**, *22* (23), 9712–9717.

(111) Jin fan, H.; Knez, M.; Scholz, R.; Nielsch, K.; Pippel, E.; Hesse, D.; Zacharias, M.; Gösele, U. Monocrystalline Spinel Nanotube Fabrication Based on the Kirkendall Effect. *Nat. Mater.* **2006**, *5* (8), 627–631.

(112) Chen, C.; Kang, Y.; Huo, Z.; Zhu, Z.; Huang, W.; Xin, H. L.; Snyder, J. D.; Li, D.; Herron, J. A.; Mavrikakis, M.; Chi, M.; More, K. L.; Li, Y.; Markovic, N. M.; Somorjai, G. A.; Yang, P.; Stamenkovic, V. R. Highly Crystalline Multimetallic Nanoframes with Three-Dimensional Electrocatalytic Surfaces. *Science* **2014**, *343* (6177), 1339–1343.

(113) Niu, K.-Y.; Park, J.; Zheng, H.; Alivisatos, A. P. Revealing Bismuth Oxide Hollow Nanoparticle Formation by the Kirkendall Effect. *Nano Lett.* **2013**, *13* (11), 5715–5719.

(114) Tang, Y.; Ouyang, M. Tailoring Properties and Functionalities of Metal Nanoparticles through Crystallinity Engineering. *Nat. Mater.* **2007**, *6* (10), 754–759.

(115) Gonzalez, E.; Arbiol, J.; Puntes, V. F. Carving at the Nanoscale: Sequential Galvanic Exchange and Kirkendall Growth at Room Temperature. *Science* **2011**, *334* (6061), 1377–1380.

(116) Park, J.; Wang, H.; Vara, M.; Xia, Y. Platinum Cubic Nanoframes with Enhanced Catalytic Activity and Durability Toward Oxygen Reduction. *ChemSusChem* **2016**, *9* (19), 2855–2861.

(117) Huang, Z.; Raciti, D.; Yu, S.; Zhang, L.; Deng, L.; He, J.; Liu, Y.; Khashab, N. M.; Wang, C.; Gong, J.; Nie, Z. Synthesis of Platinum Nanotubes and Nanorings via Simultaneous Metal Alloying and Etching. *J. Am. Chem. Soc.* **2016**, *138* (20), 6332–6335.

(118) Wong, Y. J.; Zhu, L.; Teo, W. S.; Tan, Y. W.; Yang, Y.; Wang, C.; Chen, H. Revisiting the Stöber Method: Inhomogeneity in Silica Shells. *J. Am. Chem. Soc.* **2011**, *133* (30), 11422–11425.

(119) Hu, M.; Furukawa, S.; Ohtani, R.; Sukegawa, H.; Nemoto, Y.; Reboul, J.; Kitagawa, S.; Yamauchi, Y. Synthesis of Prussian Blue Nanoparticles with a Hollow Interior by Controlled Chemical Etching. *Angew. Chem. Int. Ed.* **2012**, *51* (4), 984–988.

(120) Lu, X.; Au, L.; McLellan, J.; Li, Z.-Y.; Marquez, M.; Xia, Y. Fabrication of Cubic Nanocages and Nanoframes by Dealloying Au/Ag Alloy Nanoboxes with an Aqueous Etchant Based on $Fe(NO_3)_3$ or NH_4OH. *Nano Lett.* **2007**, *7* (6), 1764–1769.

(121) Li, H.-H.; Yu, S.-H. Recent Advances on Controlled Synthesis and Engineering of Hollow Alloyed Nanotubes for Electrocatalysis. *Adv. Mater.* **2019**, *31* (38), 1803503.

(122) Cui, C.-H.; Liu, X.-J.; Li, H.-H.; Gao, M.-R.; Liang, H.-W.; Yao, H.-B.; Yu, S.-H. Ternary PtPdCu Electrocatalyst Formed through Surface-Atomic Redistribution against Leaching. *ChemCatChem* **2012**, *4* (10), 1560–1563.

(123) Cui, C.-H.; Yu, J.-W.; Li, H.-H.; Gao, M.-R.; Liang, H.-W.; Yu, S.-H. Remarkable Enhancement of Electrocatalytic Activity by Tuning the Interface of Pd–Au Bimetallic Nanoparticle Tubes. *ACS Nano* **2011**, *5* (5), 4211–4218.

(124) Cui, C.-H.; Li, H.-H.; Yu, J.-W.; Gao, M.-R.; Yu, S.-H. Ternary Heterostructured Nanoparticle Tubes: A Dual Catalyst and Its Synergistic Enhancement Effects for O_2/H_2O_2 Reduction. *Angew. Chem. Int. Ed.* **2010**, *49* (48), 9149–9152.

(125) Cui, C.-H.; Li, H.-H.; Yu, S.-H. Large Scale Restructuring of Porous Pt-Ni Nanoparticle Tubes for Methanol Oxidation: A Highly Reactive, Stable, and Restorable Fuel Cell Catalyst. *Chem. Sci.* **2011**, *2* (8), 1611.

(126) Cui, C.-H.; Li, H.-H.; Yu, S.-H. A General Approach to Electrochemical Deposition of High Quality Free-Standing Noble Metal (Pd, Pt, Au, Ag) Sub-Micron Tubes Composed of Nanoparticles in Polar Aprotic Solvent. *Chem Commun* **2010**, *46* (6), 940–942.

(127) Zhang, L.; Wei, M.; Wang, S.; Li, Z.; Ding, L.-X.; Wang, H. Highly Stable PtP Alloy Nanotube Arrays as a Catalyst for the Oxygen Reduction Reaction in Acidic Medium. *Chem. Sci.* **2015**, *6* (5), 3211–3216.

(128) Ding, L.-X.; Wang, A.-L.; Li, G.-R.; Liu, Z.-Q.; Zhao, W.-X.; Su, C.-Y.; Tong, Y.-X. Porous Pt-Ni-P Composite Nanotube Arrays: Highly Electroactive and Durable Catalysts for Methanol Electrooxidation. *J. Am. Chem. Soc.* **2012**, *134* (13), 5730–5733.

(129) Zhang, L.; Ding, L.-X.; Chen, H.; Li, D.; Wang, S.; Wang, H. Self-Supported PtAuP Alloy Nanotube Arrays with Enhanced Activity and Stability for Methanol Electro-Oxidation. *Small* **2017**, *13* (17), 1604000.

(130) Choi, B.-S.; Lee, Y. W.; Kang, S. W.; Hong, J. W.; Kim, J.; Park, I.; Han, S. W. Multimetallic Alloy Nanotubes with Nanoporous Framework. *ACS Nano* **2012**, *6* (6), 5659–5667.

(131) Minch, R.; Es-Souni, M. On-Substrate, Self-Standing Hollow-Wall Pt and PtRu-Nanotubes and Their Electrocatalytic Behavior. *Chem. Commun.* **2011**, *47* (22), 6284.

(132) Wang, A.-L.; Wan, H.-C.; Xu, H.; Tong, Y.-X.; Li, G.-R. Quinary PdNiCoCuFe Alloy Nanotube Arrays as Efficient Electrocatalysts for Methanol Oxidation. *Electrochimica Acta* **2014**, *127*, 448–453.

(133) Wang, A.-L.; Xu, H.; Feng, J.-X.; Ding, L.-X.; Tong, Y.-X.; Li, G.-R. Design of Pd/PANI/Pd Sandwich-Structured Nanotube Array Catalysts with Special Shape Effects and Synergistic Effects for Ethanol Electrooxidation. *J. Am. Chem. Soc.* **2013**, *135* (29), 10703–10709.

(134) Zhao, Y.; Liu, J.; Liu, C.; Wang, F.; Song, Y. Amorphous CuPt Alloy Nanotubes Induced by $Na_2S_2O_3$ as Efficient Catalysts for the Methanol Oxidation Reaction. *ACS Catal.* **2016**, *6* (7), 4127–4134.

(135) Alia, S. M.; Jensen, K. O.; Pivovar, B. S.; Yan, Y. Platinum-Coated Palladium Nanotubes as Oxygen Reduction Reaction Electrocatalysts. *ACS Catal.* **2012**, *2* (5), 858–863.

(136) Zheng, J.; Cullen, D. A.; Forest, R. V.; Wittkopf, J. A.; Zhuang, Z.; Sheng, W.; Chen, J. G.; Yan, Y. Platinum–Ruthenium Nanotubes and Platinum–Ruthenium Coated Copper Nanowires As Efficient Catalysts for Electro-Oxidation of Methanol. *ACS Catal.* **2015**, *5* (3), 1468–1474.

(137) Liang, H.-W.; Liu, S.; Gong, J.-Y.; Wang, S.-B.; Wang, L.; Yu, S.-H. Ultrathin Te Nanowires: An Excellent Platform for Controlled Synthesis of Ultrathin Platinum and Palladium Nanowires/Nanotubes with Very High Aspect Ratio. *Adv. Mater.* **2009**, *21* (18), 1850–1854.

(138) Zuo, Y.; Cai, K.; Wu, L.; Li, T.; Lv, Z.; Liu, J.; Shao, K.; Han, H. Spiny-Porous Platinum Nanotubes with Enhanced Electrocatalytic Activity for Methanol Oxidation. *J. Mater. Chem. A* **2015**, *3* (4), 1388–1391.

(139) Lou, Y.; Li, C.; Gao, X.; Bai, T.; Chen, C.; Huang, H.; Liang, C.; Shi, Z.; Feng, S. Porous Pt Nanotubes with High Methanol Oxidation Electrocatalytic Activity Based on Original Bamboo-Shaped Te Nanotubes. *ACS Appl. Mater. Interfaces* **2016**, *8* (25), 16147–16153.

(140) Li, H.-H.; Fu, Q.-Q.; Xu, L.; Ma, S.-Y.; Zheng, Y.-R.; Liu, X.-J.; Yu, S.-H. Highly Crystalline PtCu Nanotubes with Three Dimensional Molecular Accessible and Restructured Surface for Efficient Catalysis. *Energy Environ. Sci.* **2017**, *10* (8), 1751–1756.

(141) Ma, S.-Y.; Li, H.-H.; Hu, B.-C.; Cheng, X.; Fu, Q.-Q.; Yu, S.-H. Synthesis of Low Pt-Based Quaternary PtPdRuTe Nanotubes with Optimized Incorporation of Pd for Enhanced Electrocatalytic Activity. *J. Am. Chem. Soc.* **2017**, *139* (16), 5890–5895.

(142) Li, H.-H.; Cui, C.-H.; Zhao, S.; Yao, H.-B.; Gao, M.-R.; Fan, F.-J.; Yu, S.-H. Mixed-PtPd-Shell PtPdCu Nanoparticle Nanotubes Templated from Copper Nanowires as Efficient and Highly Durable Electrocatalysts. *Adv. Energy Mater.* **2012**, *2* (10), 1182–1187.

(143) Chen, Z.; Waje, M.; Li, W.; Yan, Y. Supportless Pt and PtPd Nanotubes as Electrocatalysts for Oxygen-Reduction Reactions. *Angew. Chem. Int. Ed.* **2007**, *46* (22), 4060–4063.

(144) Ye, S.; Azad, A. A.; Chambers, J. E.; Beckett, A. J.; Roach, L.; Moorcroft, S. C. T.; Aslam, Z.; Prior, I. A.; Markham, A. F.; Coletta, P. L.; Marciniak, S. J.; Evans, S. D. Exploring High Aspect Ratio Gold Nanotubes as Cytosolic Agents: Structural Engineering and Uptake into Mesothelioma Cells. *Small* **2020**, *16* (46), 2003793.

(145) Ye, S.; Marston, G.; McLaughlan, J. R.; Sigle, D. O.; Ingram, N.; Freear, S.; Baumberg, J. J.; Bushby, R. J.; Markham, A. F.; Critchley, K.; Coletta, P. L.; Evans, S. D. Engineering Gold Nanotubes with Controlled Length and Near-Infrared Absorption for Theranostic Applications. *Adv. Funct. Mater.* **2015**, *25* (14), 2117–2127.

(146) Cai, K.; Zhang, W.; Zhang, J.; Li, H.; Han, H.; Zhai, T. Design of Gold Hollow Nanorods with Controllable Aspect Ratio for Multimodal Imaging and Combined Chemo-Photothermal Therapy in the Second Near-Infrared Window. *ACS Appl. Mater. Interfaces* **2018**, *10* (43), 36703–36710.

(147) Lin, Y.; Wang, L.; Zhang, H.; Wu, L.; Fan, H.; Liu, X.; Zheng, R.; Tian, X.; He, H. Widely Tunable Surface Plasmon Resonance and Uniquely Superior SERS Performance of Au Nanotube Network Films. *Nanotechnology* **2021**, *32* (29), 295706.

(148) McPhillips, J.; Murphy, A.; Jonsson, M. P.; Hendren, W. R.; Atkinson, R.; Höök, F.; Zayats, A. V.; Pollard, R. J. High-Performance Biosensing Using Arrays of Plasmonic Nanotubes. *ACS Nano* **2010**, *4* (4), 2210–2216.

(149) Torati, S. R.; Reddy, V.; Yoon, S. S.; Kim, C. Electrochemical Biosensor for Mycobacterium Tuberculosis DNA Detection Based on Gold Nanotubes Array Electrode Platform. *Biosens. Bioelectron.* **2016**, *78*, 483–488.

(150) Li, X.; Cao, L.; Zhang, Y.; Yan, P.; Kirk, D. W. Fabrication and Modeling of an Ultrasensitive Label Free Impedimetric Immunosensor for Aflatoxin B_1 Based on Protein A Self-Assembly Modified Gold 3D Nanotube Electrode Ensembles. *Electrochimica Acta* **2017**, *247*, 1052–1059.

(151) Shariati, M.; Ghorbani, M.; Sasanpour, P.; Karimizefreh, A. An Ultrasensitive Label Free Human Papilloma Virus DNA Biosensor Using Gold Nanotubes Based on Nanoporous Polycarbonate in Electrical Alignment. *Anal. Chim. Acta* **2019**, *1048*, 31–41.

(152) Yang, G.; Yang, X.; Yang, C.; Yang, Y. A Reagentless Amperometric Immunosensor for Human Chorionic Gonadotrophin Based on a Gold Nanotube Arrays Electrode. *Colloids Surf. Physicochem. Eng. Asp.* **2011**, *389* (1–3), 195–200.

(153) Gu, X.; Cong, X.; Ding, Y. Platinum-Decorated Au Porous Nanotubes as Highly Efficient Catalysts for Formic Acid Electro-Oxidation. *ChemPhysChem* **2010**, *11* (4), 841–846.

(154) Fu, Q.-Q.; Li, H.-H.; Ma, S.-Y.; Hu, B.-C.; Yu, S.-H. A Mixed-Solvent Route to Unique PtAuCu Ternary Nanotubes Templated from Cu Nanowires as Efficient Dual Electrocatalysts. *Sci. China Mater.* **2016**, *59* (2), 112–121.

(155) Sun, H.; Guo, X.; Ye, W.; Kou, S.; Yang, J. Charge Transfer Accelerates Galvanic Replacement for PtAgAu Nanotubes with Enhanced Catalytic Activity. *Nano Res.* **2016**, *9* (4), 1173–1181.

(156) Guan, S.; Fu, X.; Tang, Y.; Peng, Z. Synthesis and Photoeletrochemical Performance of AuAg@CdS Double-Walled Nanotubes. *Chem. Phys. Lett.* **2017**, *682*, 128–132.

(157) Yang, W.; Zhang, Q.; Peng, C.; Wu, E.; Chen, S.; Ma, Y.; Hou, J.; He, Y.; Zhang, B.; Deng, L. Au@PdAg Core–Shell Nanotubes as Advanced Electrocatalysts for Methanol Electrooxidation in Alkaline Media. *RSC Adv.* **2019**, *9* (2), 931–939.

(158) Xue, M.; Tan, Y. Hollow Alloy Nanostructures Templated by Au Nanorods: Synthesis, Mechanistic Insights, and Electrocatalytic Activity. *Nanoscale* **2014**, *6* (21), 12500–12514.

(159) Huang, Z.; Gong, J.; Nie, Z. Symmetry-Breaking Synthesis of Multicomponent Nanoparticles. *Acc. Chem. Res.* **2019**, *52* (4), 1125–1133.

(160) Gilroy, K. D.; Peng, H.-C.; Yang, X.; Ruditskiy, A.; Xia, Y. Symmetry Breaking during Nanocrystal Growth. *Chem. Commun.* **2017**, *53* (33), 4530–4541.

(161) Sun, Y.; Xia, Y. Multiple-Walled Nanotubes Made of Metals. *Adv. Mater.* **2004**, *16* (3), 264–268.

(162) Jang, H.-J.; Ham, S.; Acapulco, J. A. I.; Song, Y.; Hong, S.; Shuford, K. L.; Park, S. Fabrication of 2D Au Nanorings with Pt Framework. *J. Am. Chem. Soc.* **2014**, *136* (50), 17674–17680.

(163) Chen, H. M.; Liu, R.-S.; Lo, M.-Y.; Chang, S.-C.; Tsai, L.-D.; Peng, Y.-M.; Lee, J.-F. Hollow Platinum Spheres with Nano-Channels: Synthesis and Enhanced Catalysis for Oxygen Reduction. *J. Phys. Chem. C* **2008**, *112* (20), 7522–7526.

(164) Wang, Q.; Wang, H.; Yang, Y.; Jin, L.; Liu, Y.; Wang, Y.; Yan, X.; Xu, J.; Gao, R.; Lei, P.; Zhu, J.; Wang, Y.; Song, S.; Zhang, H. Plasmonic Pt Superstructures with Boosted Near-Infrared Absorption and Photothermal Conversion Efficiency in the Second Biowindow for Cancer Therapy. *Adv. Mater.* **2019**, *31* (46), 1904836.

(165) Hong, J. W.; Kang, S. W.; Choi, B.-S.; Kim, D.; Lee, S. B.; Han, S. W. Controlled Synthesis of Pd–Pt Alloy Hollow Nanostructures with Enhanced Catalytic Activities for Oxygen Reduction. *ACS Nano* **2012**, *6* (3), 2410–2419.

(166) Tao, L.; Yu, D.; Zhou, J.; Lu, X.; Yang, Y.; Gao, F. Ultrathin Wall (1 Nm) and Superlong Pt Nanotubes with Enhanced Oxygen Reduction Reaction Performance. *Small* **2018**, *14* (22), 1704503.

(167) Peng, Z.; Yang, H. Designer Platinum Nanoparticles: Control of Shape, Composition in Alloy, Nanostructure and Electrocatalytic Property. *Nano Today* **2009**, *4* (2), 143–164.

(168) Fan, F.-R.; Liu, D.-Y.; Wu, Y.-F.; Duan, S.; Xie, Z.-X.; Jiang, Z.-Y.; Tian, Z.-Q. Epitaxial Growth of Heterogeneous Metal Nanocrystals: From Gold Nano-Octahedra to Palladium and Silver Nanocubes. *J. Am. Chem. Soc.* **2008**, *130* (22), 6949–6951.

(169) Li, X.; Chen, Q.; Wang, M.; Cao, Z.; Zhan, Q.; He, T.; Kuang, Q.; Yin, Y.; Jin, M. Coordination Effect Assisted Synthesis of Ultrathin Pt Layers on Second Metal Nanocrystals as Efficient Oxygen Reduction Electrocatalysts. *J. Mater. Chem. A* **2016**, *4* (34), 13033–13039.

(170) Xie, S.; Choi, S.-I.; Lu, N.; Roling, L. T.; Herron, J. A.; Zhang, L.; Park, J.; Wang, J.; Kim, M. J.; Xie, Z.; Mavrikakis, M.; Xia, Y. Atomic Layer-by-Layer Deposition of Pt on Pd Nanocubes for Catalysts with Enhanced Activity and Durability toward Oxygen Reduction. *Nano Lett.* **2014**, *14* (6), 3570–3576.

(171) Xia, Y.; Xia, X.; Peng, H.-C. Shape-Controlled Synthesis of Colloidal Metal Nanocrystals: Thermodynamic versus Kinetic Products. *J. Am. Chem. Soc.* **2015**, *137* (25), 7947–7966.

(172) González, E.; Merkoçi, F.; Arenal, R.; Arbiol, J.; Esteve, J.; Bastús, N. G.; Puntes, V. Enhanced Reactivity of High-Index Surface Platinum Hollow Nanocrystals. *J. Mater. Chem. A* **2016**, *4* (1), 200–208.

(173) Klinkova, A.; Larin, E. M.; Prince, E.; Sargent, E. H.; Kumacheva, E. Large-Scale Synthesis of Metal Nanocrystals in Aqueous Suspensions. *Chem. Mater.* **2016**, *28* (9), 3196–3202.

(174) Guo, J.; Zhang, Y.; Shi, L.; Zhu, Y.; Mideksa, M. F.; Hou, K.; Zhao, W.; Wang, D.; Zhao, M.; Zhang, X.; Lv, J.; Zhang, J.; Wang, X.; Tang, Z. Boosting Hot Electrons in Hetero-Superstructures for Plasmon-Enhanced Catalysis. *J. Am. Chem. Soc.* **2017**, *139* (49), 17964–17972.

(175) Krishnaswamy, R.; Remita, H.; Impéror-Clerc, M.; Even, C.; Davidson, P.; Pansu, B. Synthesis of Single-Crystalline Platinum Nanorods within a Soft Crystalline Surfactant-Pt ^{II} Complex. *ChemPhysChem* **2006**, *7* (7), 1510–1513.

(176) Thomas, N.; Mani, E. An Analytical Solution to the Kinetics of Growth of Gold Nanorods. *RSC Adv.* **2016**, *6* (36), 30028–30036.

(177) Zhao, T.; Elzatahry, A.; Li, X.; Zhao, D. Single-Micelle-Directed Synthesis of Mesoporous Materials. *Nat. Rev. Mater.* **2019**, *4* (12), 775–791.

(178) Guo, K.; Liu, Y.; Han, M.; Xu, D.; Bao, J. Highly Branched Ultrathin Pt–Ru Nanodendrites. *Chem. Commun.* **2019**, *55* (74), 11131–11134.

(179) Gao, J.; Bender, C. M.; Murphy, C. J. Dependence of the Gold Nanorod Aspect Ratio on the Nature of the Directing Surfactant in Aqueous Solution. *Langmuir* **2003**, *19* (21), 9065–9070.

(180) Chang, G.; Oyama, M.; Hirao, K. Facile Synthesis of Monodisperse Palladium Nanocubes and the Characteristics of Self-Assembly. *Acta Mater.* **2007**, *55* (10), 3453–3456.

(181) Wu, H.-L.; Kuo, C.-H.; Huang, M. H. Seed-Mediated Synthesis of Gold Nanocrystals with Systematic Shape Evolution from Cubic to Trisoctahedral and Rhombic Dodecahedral Structures. *Langmuir* **2010**, *26* (14), 12307–12313.

(182) Huang, Z.; Liu, Y.; Zhang, Q.; Chang, X.; Li, A.; Deng, L.; Yi, C.; Yang, Y.; Khashab, N. M.; Gong, J.; Nie, Z. Collapsed Polymer-Directed Synthesis of Multicomponent Coaxial-like Nanostructures. *Nat. Commun.* **2016**, *7* (1), 12147.

(183) González-Pérez, A.; Czapkiewicz, J.; Prieto, G.; Rodríguez, J. R. Second Critical Micelle Concentration of Dodecyldimethylbenzylammonium Chloride in Aqueous Solution at 25 °C. *Colloid Polym. Sci.* **2003**, *281* (12), 1191–1195.

(184) Veisz, B.; Király, Z. Size-Selective Synthesis of Cubooctahedral Palladium Particles Mediated by Metallomicelles. *Langmuir* **2003**, *19* (11), 4817–4824.

(185) Zhou, Y.; Zeng, H. C. Simultaneous Synthesis and Assembly of Noble Metal Nanoclusters with Variable Micellar Templates. *J Am Chem Soc* **2014**, 13.

(186) Prashar, A. K.; Hodgkins, R. P.; Chandran, J. N.; Rajamohanan, P. R.; Devi, R. N. In Situ Encapsulation of Pt Nanoarchitectures of Varying Morphologies in Mesoporous Compounds. *Chem. Mater.* **2010**, *22* (5), 1633–1639.

(187) Li, W.; Han, Y.-C.; Zhang, J.-L.; Wang, B.-G. Effect of Ethanol on the Aggregation Properties of Cetyltrimethylammonium Bromide Surfactant. *Colloid J.* **2005**, *67* (2), 159–163.

(188) Callaghan, A.; Doyle, R.; Alexander, E.; Palepu, R. Thermodynamic Properties of Micellization and Adsorption and Electrochemical Studies of Hexadecylpyridinium Bromide in Binary Mixtures of 1,2-Ethanediol with Water. *Langmuir* **1993**, *9* (12), 3422–3426.

(189) Palepu, R.; Gharibi, H.; Bloor, D. M.; Wyn-Jones, E. Electrochemical Studies Associated with the Micellization of Cationic Surfactants in Aqueous Mixtures of Ethylene Glycol and Glycerol. *Langmuir* **1993**, *9* (1), 110–112.

(190) Torigoe, K.; Esumi, K. Preparation of Colloidal Gold by Photoreduction of Tetracyanoaurate(1-)-Cationic Surfactant Complexes. *Langmuir* **1992**, *8* (1), 59–63.

(191) Mukerjee, P.; Mysels, K. *Critical Micelle Concentrations of Aqueous Surfactant Systems*.

(192) Kim, J.-W.; Galanzha, E. I.; Shashkov, E. V.; Moon, H.-M.; Zharov, V. P. Golden Carbon Nanotubes as Multimodal Photoacoustic and Photothermal High-Contrast Molecular Agents. *Nat. Nanotechnol.* **2009**, *4*, 7.

(193) Bridges, C. R.; DiCarmine, P. M.; Fokina, A.; Huesmann, D.; Seferos, D. S. Synthesis of Gold Nanotubes with Variable Wall Thicknesses. *J. Mater. Chem. A* **2013**, 7.

(194) Zhu, H.; Chen, H.; Wang, J.; Li, Q. Fabrication of Au Nanotube Arrays and Their Plasmonic Properties. *Nanoscale* **2013**, *5* (9), 3742.

(195) Wang, J.; Zhang, C.; Zhang, J.; Song, H.; Wang, P.; Lu, Y.; Fei, G.; Xu, W.; Xu, W.; Zhang, L.; Kivshar, Y. S.; Zhang, L. Hybrid Plasmonic Cavity Modes in Arrays of Gold Nanotubes. **2017**, 11.

(196) Murphy, A.; McPhillips, J.; Hendren, W.; McClatchey, C.; Atkinson, R.; Wurtz, G.; Zayats, A. V.; Pollard, R. J. The Controlled Fabrication and Geometry Tunable Optics of Gold Nanotube Arrays. *Nanotechnology* **2011**, *22* (4), 045705.

(197) Bi, Y.; Lu, G. Controlled Synthesis of Pentagonal Gold Nanotubes at Room Temperature. *Nanotechnology* **2008**, *19* (27), 275306.

(198) Hendren, W. R.; Murphy, A.; Evans, P.; O'Connor, D.; Wurtz, G. A.; Zayats, A. V.; Atkinson, R.; Pollard, R. J. Fabrication and Optical Properties of Gold Nanotube Arrays. *J Phys* **2008**, 6.

(199) Kohl, J.; Fireman, M.; O'Carroll, D. M. Surface Plasmon and Photonic Mode Propagation in Gold Nanotubes with Varying Wall Thickness. *Phys. Rev. B* **2011**, *84* (23), 235118.

(200) Velichko, E. A. Plasmon Resonances in the Scattering and Absorption of Light by a Circular Gold Nanotube. In *2014 IEEE 34th International Scientific Conference on Electronics and Nanotechnology (ELNANO)*; 2014; pp 42–45.

(201) Zhu, J.; Li, F.-K. Effect of Aspect Ratio on the Inter-Surface Plasmonic Coupling of Tubular Gold Nanoparticle. *Eur. Phys. J. B* **2011**, *80* (1), 83–87.

(202) Olmon, R. L.; Slovick, B.; Johnson, T. W.; Shelton, D.; Oh, S.-H.; Boreman, G. D.; Raschke, M. B. Optical Dielectric Function of Gold. *Phys. Rev. B* **2012**, *86* (23), 235147.

(203) Yoo, S.; Go, S.; Son, J.; Kim, J.; Lee, S.; Haddadnezhad, M.; Hilal, H.; Kim, J.-M.; Nam, J.-M.; Park, S. Au Nanorings with Intertwined Triple Rings. *J. Am. Chem. Soc.* **2021**, jacs.1c05189.

(204) Scarabelli, L.; Sánchez-Iglesias, A.; Pérez-Juste, J.; Liz-Marzán, L. M. A "Tips and Tricks" Practical Guide to the Synthesis of Gold Nanorods. *J. Phys. Chem. Lett.* **2015**, *6* (21), 4270–4279.

(205) Grzelczak, M.; Pérez-Juste, J.; García de Abajo, F. J.; Liz-Marzán, L. M. Optical Properties of Platinum-Coated Gold Nanorods. *J. Phys. Chem. C* **2007**, *111* (17), 6183–6188.

(206) Fennell, J.; He, D.; Tanyi, A. M.; Logsdail, A. J.; Johnston, R. L.; Li, Z. Y.; Horswell, S. L. A Selective Blocking Method To Control the Overgrowth of Pt on Au Nanorods. *J. Am. Chem. Soc.* **2013**, *135* (17), 6554–6561.

(207) Forcherio, G. T.; Baker, D. R.; Boltersdorf, J.; Leff, A. C.; McClure, J. P.; Grew, K. N.; Lundgren, C. A. Targeted Deposition of Platinum onto Gold Nanorods by Plasmonic Hot Electrons. *J. Phys. Chem. C* **2018**, *122* (50), 28901–28909.

(208) Zorić, I.; Zäch, M.; Kasemo, B.; Langhammer, C. Gold, Platinum, and Aluminum Nanodisk Plasmons: Material Independence, Subradiance, and Damping Mechanisms. *ACS Nano* **2011**, *5* (4), 2535–2546.

(209) Li, Z.; Wang, W.; Yin, Y. Colloidal Assembly and Active Tuning of Coupled Plasmonic Nanospheres. *Trends Chem.* **2020**, *2* (7), 593–608.

(210) Han, X.; Goebl, J.; Lu, Z.; Yin, Y. Role of Salt in the Spontaneous Assembly of Charged Gold Nanoparticles in Ethanol. *Langmuir* **2011**, *27* (9), 5282–5289.

(211) Zhang, K.; Song, T.; Wang, C.; You, H.; Zou, B.; Guo, S.; Du, Y.; Li, S. Surface Plasmon Resonance Boost Electrocatalytic Alcohol Oxidation over Three-Dimensional PdM (M = Au, Ag, Cu) Nanosheet Assemblies. *Inorg. Chem.* **2021**, acs.inorgchem.1c00885.

(212) Yang, H.; Wang, Z.-H.; Zheng, Y.-Y.; He, L.-Q.; Zhan, C.; Lu, X.; Tian, Z.-Q.; Fang, P.-P.; Tong, Y. Tunable Wavelength Enhanced Photoelectrochemical Cells from Surface Plasmon Resonance. *J. Am. Chem. Soc.* **2016**, *138* (50), 16204–16207.

(213) *Handbook of X-Ray Photoelectron Spectroscopy: A Reference Book of Standard Spectra for Identification and Interpretation of XPS Data*, Update.; Moulder, J. F., Chastain, J., Eds.; Perkin-Elmer Corporation: Eden Prairie, Minn, 1992.

(214) Peng, Y.; Li, L.; Tao, R.; Tan, L.; Qiu, M.; Guo, L. One-Pot Synthesis of Au@Pt Star-like Nanocrystals and Their Enhanced Electrocatalytic Performance for Formic Acid and Ethanol Oxidation. *Nano Res.* **2018**, *11* (6), 3222–3232.